Investigations of Ta and Nb doped $KTiOPO_4$ derivatives

by

Christopher John Eaton

Thesis

Submitted to the University of Warwick
for the degree of

Doctor of Philosophy

Physics Department
September 1998

CONTENTS

LIST OF FIGURES

LIST OF TABLES

ACKNOWLEDGMENTS

I would like to thank and acknowledge the following people for help, friendship, guidance, encouragement, tea, toast and company in varying degrees and in no correlatory order: Dr Keith Hutton (for Pratchettisms), Dr C. McConville, Dr. R. Ward, Dr D. MckPaul, Dr M. Womersley, Dr W. Healy, Dr G. Styles, Mick Smith, Keith Briggs (for song), Dr. R. I. Cartwright (for general madness and weddings), Debbie Hill & Russ Bielby (for cheeriness in Woodside), Kevin Pike, Greg Gibbons, Ioanna Matsouli (for similarity), Paul Verlander (for Nights), Christoph Schetelich, Tina Latham, Al Campbell, Mum & Dad & Netty & Nanna & Bampa (all for constant support), and my girlfriend Justine, without whom I would be lost.

I would particularly like to thank Dr Pam Thomas for her guidance and support as my supervisor throughout this reasearch.

Thanks are also due to the project's funding body EPSRC, from which various Daresbury grants were also obtained, and D.E.R.A. for their financial support throughout this research via the CASE scheme.

This thesis is dedicated to Nanna and Bampa

All that glitters....
....has a high refractive index.
-Anon

DECLARATION

The material in this thesis is my own, except where stated, and was carried out in the Department of Physics at the University of Warwick in the period October 1994 to September 1998. No part of this work has been submitted previously to the university of Warwick, nor any other academic institution, for admission to a higher degree.

The material in Chapter 5 was researched in collaboration with Dr Keith Hutton, Oxford University. Portions of the research in Chapter 4 were carried out in collaboration with Dr M. Womersley, Warwick University.

SUMMARY

The non-linear optical material KTiOPO4 (KTP) has been established as an industry standard material for frequency-doubling of Nd:YAG 1μm radiation into the green visible range. Technological requirements for extended frequency-doubling into the visible blue have prompted the pursuit of doped KTP isomorphs which possess the already desirable characteristics of KTP itself, with modified non-linear optical responses to produce novel, useful materials. This thesis is an investigation of the crystal quality of some of these KTP isomorphs and the structural features of one such material.

High-resolution x-ray diffraction techniques are used to examine the structural quality of Nb, Ta and Ta/Ga doped KTP. It is demonstrated that differing perfection is found for these materials compared to pure KTP, and each possesses a degree of mosaicity.

Single-crystal diffraction is used to carry out a detailed structural refinement for 4% Ta-doped KTP, and demonstrates the similarity of this structure to previously refined structures for Nb-doped KTP. A potential new site for Ta incorporation into the unit cell is suggested. A simulation of the material's refractive indices, based on polarisability volume calculations, is carried out. The significance of the simulation is discussed in the context of improved optical performance of these crystals.

White-beam synchrotron radiation topographic studies are carried out for the Ta and Ta/Ga-doped KTP materials, and the presence of significant defect structures and associated domains is reported. The implications for non-linear optical quality are discussed.

ABBREVIATIONS

CCD	Charge-coupled device
cps	Counts per second
CW	Continuous wave
EO	Electro-optic
FWHM	Full-width, half-maximum
GSB	Growth-sector boundary
HRXRD	High-resolution x-ray diffraction
ITFC	International Tables for Crystallography
KTA	Potassium titanyl arsenate, $KTiOAsO_4$
KTP	Potassium titanyl phosphate, $KTiOPO_4$
MRD	Materials Research Diffractometer
NCPM	Non-critical phase-matching
NLO	Non-linear optic(al)
OPO	Optical parametric oscillator
PM	Phase-matching
QPM	Quasi-phase-matching
RLP	Reciprocal-lattice point
SH	Second harmonic
SHG	Second-harmonic generation
TSSG	Top-seeded solution growth

Chapter 1

Non-Linear Optical Processes and the KTP family of Materials.

1.1 Non-Linear Optics

1.1.1 Introduction.

Non-linear optics describes the interaction between light and certain materials in manners that go beyond familiar optical effects such as refraction and diffraction. The field of non-linear optics developed simultaneously with the development of more powerful lasers, and as lasers of new wavelengths became available throughout the 1960's. Many materials, crystalline, ceramic and polymeric, were discovered that exhibited the various effects of electro-optics, photo-refraction, and frequency-doubling: the first such experiment was performed by P.Franken *et al*[1] in 1961. These and other non-linear optical processes are now an important research field, and contribute to commercially useful products.

Non-linear optical (NLO) effects are those interactions between the electric field of a light ray and a material where the electronic response of the material does not scale linearly with the E-field[2]. When a light wave passes through a material, its electric-field vector interacts with the electronic environment of the material, such that when one or more light waves propagate through a material, they generate new polarisation states in this environment. These polarisations oscillate as the wave-fields propagate. If the electronic character of the material is of a nature that anharmonic interactions with the light waves take place, then certain of the interactions between the wave and the electrons become dominant and non-linear processes become possible; for example frequency-doubling. In one particular material, several non-linear optical processes may be possible, and then the material's utility is determined by which effect dominates. The various

properties of an NLO material are described by its (tensor) non-linear susceptibilities.

The uses of NLO materials are found when they are combined with laser radiation, and these uses are widespread and evolving. For example, the electro-optic effect[2] is found where the polarisation-state of a material is altered by the application of an electric field (often of size kV mm^{-1}) across it. In combination with polarising filters, an effective optical-shutter can be produced, with switching times fractions of those of mechanical shutters. This effect was one of the first applications of NLO materials, since it has a use as a modulator and in Q-switched lasers, and so the development of laser technology was itself influenced by non-linear optics. The second-harmonic generation (SHG) phenomenon was the most immediately applied, and was used to produce coherent sources at novel wavelengths.

Many other medical and communications applications of NLO effects are apparent, and current efforts are attempting to achieve innovative devices by marrying optical communications with information-technology. One possibility is the achievement of optical devices such as computer memories or novel communications devices, possibly based on waveguided light. Recently, advances in experimental holographic non-linear optical memory have used the material lithium niobate to produce high-density data storage, having the advantages of fast access and non-volatility compared to some semiconductor equivalents[3]. Another early goal was to produce a compact blue laser, based on frequency-doubled light from a diode laser source, since the utility of such a laser in communications is high, and production of a semiconductor blue laser was difficult. $KNbO_3$ is the current material used for frequency-doubling of diode lasers into the green, and recent developments in periodically-poled devices have achieved frequency-doubling into the blue[4], whilst multiple-quantum well diode lasers have now been produced that lase in the blue[5]. This has now become a competition of power, lifetimes and cost.

In general, the pursuit of non-linear optics has aimed at producing NLO effects

from lower pump powers and at newer frequencies. This has meant development on two fronts: optimising existing optical interactions and research into novel or more cost-effective materials, driven by the technological demands of both research and device-design.

1.1.2 Polarisation.

Consider the reaction of a particle (usually an electron) in a medium to the influence of one or more electromagnetic waves propagating through the medium: the particle reacts to the *total* field acting on it. This field has multiple frequency components that are present in the input waves, and acts to displace the particle from its equilibrium location: positive particles with the field, negative particles in the opposite sense. In this situation, as the wave propagates, it can be seen that transient dipoles are created as local charge centres are displaced. A polarisation is created and is modelled by:

$$\mathbf{P} = \varepsilon_0 \{\chi_{1(ij)} \mathbf{E}_j + \chi_{2(ijk)} \mathbf{E}_j\mathbf{E}_k + \chi_{3(ijkl)} \mathbf{E}_j\mathbf{E}_k\mathbf{E}_l + \dots \} \qquad (1.1)$$

where $\mathbf{P}$ is the dipole moment per unit volume, $\mathbf{E}$ the applied field (and its components) and χ_1 is the linear susceptibility, derived from the dielectric constant, ε, by $\chi_1 = 1-\varepsilon$.

Considering the classical model, where a linear response of a material to light is seen, the electrons experience a harmonic potential, i.e. a restoring force directly proportional to the displacement (itself proportional to the magnitude of the E-field). The higher-order effects are then evidently caused by an asymmetric force acting to return the displaced particles to their equilibrium position. The higher-order terms in (1.1) are described by: χ_2 , the second-order non-linear susceptibility, responsible for SHG, the linear electro-optic effect, sum-frequency generation, and parametric oscillation. χ_3 is the third order susceptibility and is responsible for third-harmonic generation, the quadratic EO effect, two-photon absorption and others such as self-focusing.

The familiar linear polarisation equation is produced by collapsing (1.1) when

the higher-order terms disappear for a 'linear' material. Since the higher the order of the term, the more difficult it is to perceive the optical effects (i.e. in general $|\chi_2| > |\chi_3| > ...$), it can be seen why non-linear effects generally manifest under intense light-fields, such as those produced by lasers.

1.1.3 The NLO coefficients

As outlined, the electronic environment of a material determines the various coefficients of the higher-order dielectric constants, sourced particularly in a characteristic asymmetry: i.e. if one considers an electron in an asymmetric electronic environment, the restoring force created in the dipole formation will form a potential that generally makes its response anharmonic. In this case, the particle's motion will not be a sinusoidal optical oscillation, but instead a complex oscillation - essentially with Fourier components that relate to the non-linear optical effects.

At optical frequencies low-mass charged particles will manifest this behaviour more so than heavier particles and thus the electron-light interaction is far more significant than the ionic one. So if the material perceives electromagnetic radiation at optical frequencies, then the interaction does not generally involve the ionic response of the material. If this incident light is accompanied by a low-frequency or DC field, then the ionic response of the structure does become significant in its effect on the electronic response: which is the source, for example, of the linear EO effect.

The asymmetric electronic environment can either be inherent to the material, or induced by some external action. In the former case, a crystal structure which possesses no centre of inversion symmetry will automatically possess an asymmetric electron structure. In the latter case, the effects can be induced by an applied static E-field or applied light, which is the source of electro-optical and photo-refractive effects.

As described, the second-order NLO coefficient is involved in second-harmonic generation (frequency-doubling) and sum and difference frequency mixing,

whereas the third order effect is involved in third-harmonic generation and phase conjugation. For the purposes of this thesis, it is the second order coefficient which is important, since many applications of NLO materials - particularly $KTiOPO_4$ (see section 1.2) - lie in frequency-doubling and optical-parametric oscillation to achieve new light sources.

The **E**-field is a vector property, and so is the polarisation. Therefore, the various susceptibilities, χ, are tensors that by the Neumann principle, are constrained by the point symmetry of the crystal[6].

For the second-order NLO tensor, the relationship between **P** and the components of input light **Ej**, **Ek** is as follows:

$$\mathbf{P} = \sum_{i=1}^{3} \sum_{j,k=1}^{3} d_{ijk}\, \mathbf{E}_j\, \mathbf{E}_k \qquad (1.2)$$

where d_{ijk} is the third-rank tensor relating the **E**-field to **P** i.e. the second-order NLO tensor. Thus,

$$\mathbf{P} = \begin{pmatrix} P_1 \\ P_2 \\ P_3 \end{pmatrix} = \begin{pmatrix} d_{11} & d_{12} & d_{13} & d_{14} & d_{15} & d_{16} \\ d_{21} & d_{22} & d_{23} & d_{24} & d_{25} & d_{26} \\ d_{31} & d_{32} & d_{33} & d_{34} & d_{35} & d_{36} \end{pmatrix} \begin{pmatrix} E^2_1 \\ E^2_2 \\ E^2_3 \\ 2E_2E_3 \\ 2E_1E_3 \\ 2E_1E_2 \end{pmatrix} \qquad (1.3)$$

is the contracted notation for the third-rank tensors. Also knowing the restrictions placed on the tensor from the symmetry of the structure, gives the *d* tensor for KTP's *mm2* point group as:

$$\begin{pmatrix} 0 & 0 & 0 & 0 & d_{15} & 0 \\ 0 & 0 & 0 & d_{24} & 0 & 0 \\ d_{31} & d_{32} & d_{33} & 0 & 0 & 0 \end{pmatrix} \qquad (1.4)$$

and this is related to the χ_2 factor in equation (1.1)[6].

1.1.4 Second-Harmonic Generation

In the SHG process, if an NLO material is illuminated with light at the frequencies ω_1 and ω_2 , then from the χ_2 term in (1), the ongoing light will contain components at $\omega_1 + \omega_2$, and $\omega_1 - \omega_2$. This is the sum-difference effect, and can be used to generate new wavelengths by mixing inputs with different frequencies (sum-frequency generation, SFG). The absolute magnitude of the polarisation at these frequencies depends on the χ_2 tensor coefficients, but if the two incoming light fields are of a single frequency, then the sum component is 2ω, and the difference component is zero, i.e. the second-harmonic has been created. Thus SHG is a collapsing of the sum-difference effect to a special case.

If the incoming waves are propagating in a crystal, and the direction of the **E**-component is reversed, then the polarisation must also reverse, assuming the field sees an identical electronic environment:

$$\mathbf{P} \alpha \chi_{1(ij)} \mathbf{E}_j \chi_{2(ijk)} \mathbf{E}_j \mathbf{E}_k \quad \text{and...} \qquad (1.5a)$$

$$-\mathbf{P} \alpha \chi_{1(ij)} \mathbf{E}_j \chi_{2(ijk)} \mathbf{E}_j \mathbf{E}_k \qquad (1.5b)$$

This situation occurs in centrosymmetric crystals, and the inconsistency in (1.5a) and (1.5b) is only removed when the χ_2 coefficient is reduced to zero. Thus centro-symmetric crystals possess no second-order NLO properties, which illustrates the dependence on macroscopic crystal symmetry. A single electron may see a nonlinear environment, but macroscopically there can be no second-order NLO effect.

The asymmetry that permits second-order NLO effects, in a structural sense may come from a highly-asymmetric unit or molecule in the crystal structure, or a single dominant interatomic bond that is asymmetric, though the crystal itself must still possess no centre of symmetry. In centrosymmetric crystals, second-order effects are not absolutely forbidden in all cases, but the point symmetry, by the Neumann principle, may still limit some NLO coefficients.

For efficient second-order NLO effects, not only is electronic asymmetry necessary, but also high electron polarisability is required, and hence atoms with electrons that can be easily excited or are delocalised are suitable. If both asymmetry and high-polarisability are met by the particular electronic environment of a crystal, then it is likely that significant NLO effects will be seen. For example, certain organic molecules have highly delocalised electrons in their asymmetric structures and hence have characteristics for operation in the green/blue wavelength ranges (although often limited by inconvenient absorption), and it is now possible to some extent to predict their properties[7].

Importantly, a material's utility for a particular role depends not only on its coefficients but also its physical suitability. For example, the material β-BaB_2O_4 has lower NLO coefficients than some other inorganic materials, but has a transparency in the UV region that makes it extremely suitable for frequency-doubling into this region[8]: other materials possess the characteristics of an excellent frequency-doubler, but suffer from rapid optical damage at low input intensities; or production of the material in sufficiently large quantities at consistently high quality is sometimes difficult. The advantage of inorganic crystalline or ceramic materials over some polymeric/organic materials is immediately apparent in that they can be more physically robust: where an organic crystal relies largely on the inter-molecular Van-der-Waals bonds to build the solid framework, inorganic materials rely on metal-oxygen bonds. This is important for their cutting, polishing, and processing properties. So crystalline inorganic materials do have excellent end-user characteristics, that in important cases compensate for the reduced NLO coefficients compared to some of the organic materials.

1.1.5 Phase matching

The refractive index of a crystal is dependent on the frequency of light propagating in it because of optical dispersion. Generally, second-harmonic light generated at different points along the propagation direction of the fundamental light ray will be incoherent because of this, and an interference pattern is

established in the SHG light as the energy-transfer between fundamental and second-harmonic light increases and decreases as the two move into and out of phase. This interference possesses a characteristic coherence length, l_c , between adjacent maxima, and so a long crystal contains a sinusoidal power variation along the propagation direction of SHG light.

The condition of phase matching (PM) maximises the power output, and it is found that when the refractive indices for both SHG and fundamental waves are equal, i.e the phase-mismatch between the fundamental and second-harmonic light:

$$\Delta k = 2k_f - k_{sh} = 0 \qquad (1.6)$$

From this, the coherence-length is:

$$l_c = |\pi / \Delta k| \qquad (1.7)$$

and it tends to infinity as phase-matching is approached, and so the sinusoidal power variation disappears.

In uniaxial birefringent crystals, the refractive index is also dependent on the polarisation state of the light. Light polarised parallel to the optic axis forms the extra-ordinary ray and light polarised perpendicularly to the optic axis forms ordinary rays. Since the refractive index can be decomposed into components parallel and perpendicular to the optic axis, there will exist (for sufficiently birefringent crystals) a particular angle to the optic axis where differently-polarised SHG and fundamental light perceive the same refractive index.

In an optically biaxial crystal, the refractive index surface (the optical indicatrix)[2] is a general ellipsoid with three different principal axes. The refractive index varies with the angle θ from the optic axes, and also the angle ϕ from x in the xy plane (see Figure 1.1). The phase-match can be made in this case by a suitable choice of propagation angles with respect to the *ab* plane as well as to the optic axes.

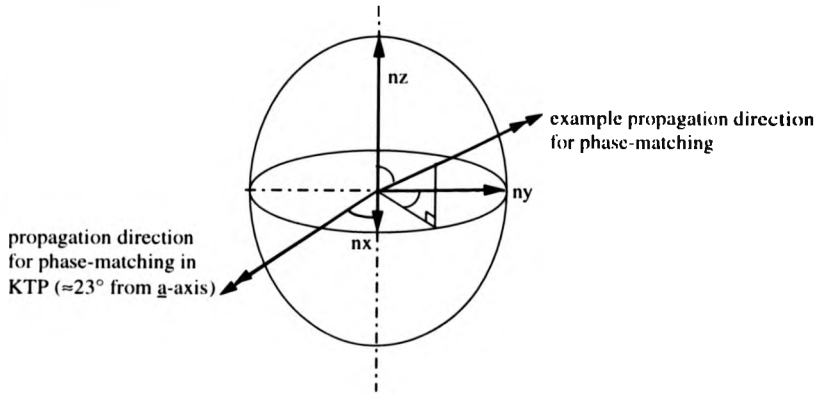

Figure 1.1 The optical indicatrix for an optically biaxial crystal, showing the major axes refractive indices, an example propagation direction for phase-matching conditions, and that of KTP.

The birefringent response of a material is, through phase-matching, central to its NLO applications.

1.1.6 Types of phase-matching.

There are three forms of 'true' phase matching and another of pseudo-phase matching.

Type I

Type I PM occurs when the wave-fronts are co-directional for both the fundamental ordinary ray and the SH extraordinary ray, but the propagation-direction is different, as well as the polarisation of the second-harmonic being perpendicular to the fundamental waves i.e. the fundamental photons are ordinary rays and the second-harmonic is extraordinary.

Type II

For type II PM, the interaction between ordinary and extraordinary fundamental rays is affected by the fact that they have different propagation directions and that the fundamental waves are polarised perpendicular to each other. After a

certain propagation distance, the fundamental and second-harmonic wave-fields are no-longer overlapping, and thus SHG becomes impossible: this separation is the walk-off effect, and is important in considering suitable materials for efficient type II PM. Where the birefringence of a sample is large enough to create significant walk-off effects, the utility of the material itself is limited for simple applications as the conversion efficiency decreases.

Non-critical phase-matching

Beam walk-off can be eliminated when the angle θ is 90° and ϕ is at some material-specific angle. In biaxial crystals (such as KTP) this is met when the dispersion is offset by the birefringence along a principal crystal axis. In this case non-critical PM (NCPM) occurs, and notably the angular sensitivity of θ and ϕ is reduced i.e. the external acceptance angle is increased. This is caused by the widening of the angle between the central phase-matching peak and the first zero in intensity in the angle-tuning curve, causing broader tolerance. (Type-II PM also possesses a similar reduction in sensitivity relative to type-I PM). Under this condition, the NLO crystal can be used to upconvert a beam with a broader angular spread - particularly useful where a focused beam geometry is required.

Quasi-phase-matching

Quasi-phase matching is an artificial effect[9], where the structure of the NLO material is modulated such that propagating SHG and fundamental light perceive, for example, a series of periodically inverted domain structures, separated by the coherence length, which compensates for the phase-mis-match, Δk, and allows the power output at the second harmonic to grow almost as for a perfectly phase-matched material.

In angle-tuning, phase-matching is achieved by adjusting the input angle relative to the refractive indices of the material, where these are within suitable limits. Where the birefringences are close to those required, in materials like $LiNbO_3$

the non-critical phase-match can be met by altering the temperature of the crystal - "temperature"-tuning the birefringence. In other materials and conditions, the phase-match can be made by designing a QPM 'device'.

1.2 Potassium Titanyl Phosphate (KTP)

1.2.1 Introduction

Different NLO materials have different characteristics, and the intense competition between organic and inorganic NLO materials is based on their relative properties. Organic materials (such as the new blue-SHG 4-aminobenzophenone[10], recently developed urea-(d)tartaric acid[11], and N-methyl urea[7]) often have very high NLO Figures of merit, sometimes tens of times that of the popular inorganic materials, such as lithium niobate. But the inorganics often have much higher optical-damage thresholds, and form crystals that are physically stronger with greater resistance to cleavage, and hence are easier to manufacture into devices.

One of the best-known inorganic crystals is $KTiOPO_4$ (KTP). It was first reported in 1890[12], noted for its birefringence, and in more recent times as an NLO material in polycrystalline form in 1971[13] , and in single crystal form in 1976 by the team of Bierlein and Zumsteg[14]. It is now grown across the world for its commercial value as a frequency-doubler, and preferred for its various excellent characteristics. Interest in KTP in the 1970's arose because of its promising physical parameters over existing materials such as lithium niobate.

KTP is a member of a group of crystals with the generic formula $MTiOXO_4$, where M is K, Rb, Tl, NH_4 and X is P or As, Ge, Si, V, with solid-solutions between the different group members having different properties[15]. Ti can also be substituted to form a greater class of materials, with Sn, Sb, Ta amongst others. Some of these family members also possess large NLO coefficients and other attractive properties, but KTP and $KTiOAsO_4$ (KTA) have been sufficiently set apart from the others by the depth of research performed, as well as commercial exploitation (in the case of KTP).

KTP is now used as a standard NLO material for frequency-doubling infra-red light at 1.064 μm from Nd:YAG lasers into the green, since it is a highly-efficient doubler at this frequency (about 60% efficiency), and has a birefringence suitable for type-II phase-matching. It is also capable of both non-critical phase-matching at 990nm and 1080nm, and type I phase-matching for pump sources up to 2μm: it has transparency from ≈350nm to ≈4500nm, and is phase-matchable in this from ≈1000nm to ≈3500nm. In fact, it is the preferred material for intracavity doubling where short pulse (pico-second) green-lasers are required. It can produce tens of watts of green CW light[16], and can also be used in an optical parametric oscillator[17]. It has a wide acceptance angle, manageable walk-off effects (in NCPM type-II configurations) and a broad temperature tolerance. Applications of the material include dedicated green light sources for experimentation and optical communications, and where the green output is further doubled to produce UV light of high average-power, new sources are produced, which are used for other applications such as laser surgery[18].

Its physical robustness make it easy to cut, polish and optically-coat for incorporation into devices, to which its low threshold power of 0.1MW, and high laser-damage threshold (of 15 GW/cm^2 for one pulse of 1ns at 1.064μm [19]) makes it ideally suited.

In common with other NLO materials KTP exhibits optical damage, seen particularly in the formation of grey-tracks where grey discoloration is seen along the light-path through the crystal[19]: this has been seen at high laser power (typically >10GW/cm^2), with CW or high pulse-cycling. Where the crystal is again exposed, catastrophic damage can occur due to power absorption and hence local heating in the track, though there are methods by which grey-track formation can be reduced[20], mainly by low temperature annealing. Grey tracks in KTP are attributed to the formation of localised Ti^{3+} centres[21], though the exact mechanism is still under investigation. It is an important consideration since the application of KTP to very high-power SHG (to which it is suited) is determined

by this damage characteristic.

KTP also possesses resistance to chemical attack, making it a useful material in harsh environments where other NLO materials may suffer. Technologically it has value as an EO modulator[22], or Q-switch, and as a permanent SHG component in optical systems. Its value in integrated optics is being investigated, with particular reference made to its wave-guide properties, and periodic-poling capabilities. These last are formed as surface-modified layers by ion indiffusion to create a shallow waveguide, or by various methods such as direct electron-beam writing to create the poled array.

1.2.2 Growth of KTP crystals

KTP decomposes incongruently when melted (at ≈1150°C) so it cannot be grown from a melt. However, it can be successfully grown by two processes: hydrothermally and from a high-temperature flux. The characteristic growth morphology, presented in both growth conditions is shown in Figure 1.2(a). Notably, the a-axis shows the shallowest growth-depth, with growth proceeding most readily along the [011] and [201] directions (and their mirror opposites), forming the wing-like sections that cap the c and b axis growth. Other growth facets are known, but generally are much smaller. This morphology conveniently produces crystals with suitably long path-lengths with wide apertures for optical devices, since propagation is in the (001) plane, at ≈23° to [100].

The fact that KTP is ferroelectric means that ferroelectric domains can be present, particularly if the material is grown above its Curie temperature (around 935°C [23]).

This is an important consideration since the presence of such domains in a crystal degrades the non-linear optical performance of the material through differential scattering.

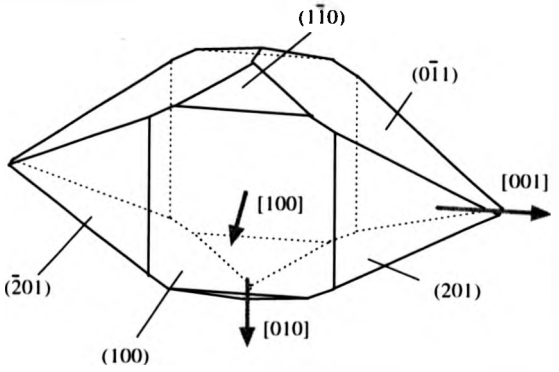

(a)

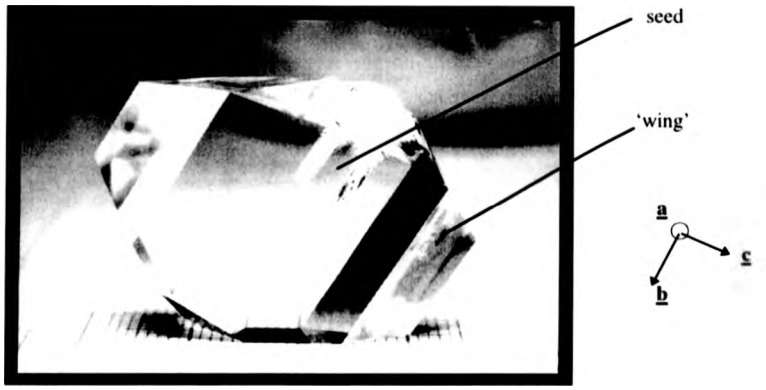

(b)

Figure 1.2 Growth morphology of pure KTP. (a) Ideal growth morphology (b) photo of typical flux-grown crystal, b-axis seed.

Growth experiments for optical devices are designed with this limitation in mind.

1.2.2.1 Hydrothermal growth.

KTP crystals can be produced hydrothermally by cooling TiO_2 in an aqueous flux of potassium salts, or by a temperature-gradient method which converts a pre-prepared KTP-glass. In recent methods Liu *et al*[24] report successful growth using TiO_2 in KH_2PO_4 at a temperature of 520-560°C and at a pressure of 24-28 kpsi (notably smaller than some growth conditions, which can be up to 1000 atmospheres). The nutrient and seed are sealed into an Au or Ag tube placed in a high-temperature/pressure autoclave with a temperature gradient of 30-70°C and

the expected route is:

$$KH_2PO_4 + TiO_2 \rightarrow KTiOPO_4 + H_2O \qquad (1.7)$$

Over several weeks, with growth rates of ≈1mm/day, crystals of useful size (e.g. 10*20*30 mm^3) and of good quality have been grown using this method and similar hydrothermal processes.

1.2.2.2 Flux growth.

KTP can also be produced by crystallising it out of a molten KTP/flux mix as this is slowly cooled. Uncontrolled flux growth produces crystals by spontaneous nucleation, yielding a large number of small crystals - each often highly perfect. A tightly-controlled flux-growth experiment is required to produce large, highly-perfect crystals avoiding inclusions and other gross defects. Typically, the flux components are heated in a three-zone furnace which produces a uniform environment with high-stability to temperatures in the region of 900°C. Larger crystals can only be produced by seeding, where a carefully prepared seed is suspended in the melt, and growth proceeds by accretion around this (see Figure 1.2(b)) - known as top-seeded solution growth (TSSG).

The Crystal Growth group at the Clarendon Laboratory, Oxford, use the route:

$$4K_2CO_3 + 6(NH_4)H_2PO_4 + 2TiO_2 \rightarrow K_6P_4O_{13} + 2KTiOPO_4 + 6NH_3 + 9H_2O + 4CO_2 \qquad (1.8)$$

where this stoichiometric mix of flux components is preheated in a box furnace to ≈700°C to ensure homogeneous mixing. The prepared flux is then heated in a three-zone furnace that has a stable zone measuring 8cm in diameter by 10cm deep, and with thermal stability of around ±0.1°C in the central zone. Initial temperatures can be as high as 1000°C, well above supersaturation (around 980°C for KTP), though the seed is not introduced until the temperature is near supersaturation else its surface can dissolve. Growth is observed between 930-880°C, through a cooling of between 0.01 and 0.1°C per hour. The top-seeded method is used with the seeds firmly attached to a platinum rod with platinum

wire and placed just beneath the surface of the hot flux. The seeds are generally plate-like crystals, often narrowest in c and with the longest axis parallel to b, harvested from previous growths since these have been shown to have excellent growth profiles. The seed can have either natural or pre-cut facets. Rotation of the seed at rates of between 50 and 70 rpm causes even growth around the central axis since this movement ensures new flux nutrient is presented to the growing surfaces at all times, and that inclusion of solution is therefore avoided. The growth of new crystal is assessed by constant computerised monitoring of the mass of the seed/crystal body: data from previous high-perfection profiles are used as guidelines. Once a crystal attains the desired size the temperature ramp-off at the end of the 30-100 day growth process is at a rate of 20 to 50°C/hour.

Regular production achieves crystals of 10*35*50 mm^3, and weighing 10-20g, though experiments have produced larger samples up to 6cm across the c-axis. These crystals are generally perfect, with only occasional imperfections associated with the seed-veil from the growth cap that forms around the seed. This region is most often associated with pre-cut seeds, and marks the boundary between dissolute growth and stable growth. In fact the size limitation can be blamed purely on the size of the crucible and furnace used, which is simply an economic consideration since the flux components are heated in an expensive high-purity platinum crucible.

Such flux-grown crystals are larger than those produced by hydrothermal methods. When removed from the flux and cleaned, the crystals are optically clear and water-white (without the yellow tinge that appears in some growths) and relatively free from surface features such as striations.

1.2.2.3 Limitations of KTP growth-methods.

Discussion has taken place over the benefits of KTP production by hydrothermal methods, since it is technologically difficult to produce very large-scale crystals. This limit comes mainly from the difficulties of producing an autoclave large enough and robust enough to provide the high temperatures and pressures

required, and the expense concerned with this and in producing the precious metal linings that insulate the crystal from the furnace. The growth process itself is sensitive: in particular the growth of single-domain crystals requires the use of a single-domain seed since growth takes place below Tc. This requires careful seed selection, since the crystal will ultimately contain the seed running through its length, limiting the available apertures for production of devices. In addition, single-domain seeds frequently produce twinned crystals: the interface with the seed provides an interruption, and allows two independent domains to grow.

Flux-grown KTP, whilst it can be grown in less demanding conditions, has its own difficulties. The process is sensitive to Fe^{3+} and Pt/Rh contamination, takes considerable time to produce large-scale crystals, requires careful combination of heating rates and rotation to allow balanced growth and can produce cracks as the material is cooled. Much research is undertaken simply to optimise this growth process.

However, it appears that hydrothermal KTP can be poled for use as a periodically-poled device (such as a waveguide), and flux-grown KTP cannot be so readily, although a successful low-temperature device has been patented recently[25]. This has been attributed to the different ionic conductivities observed in the two types, where the flux-grown material has a higher conductivity[20]. The conductivity variations are speculatively thought to relate to the defect/impurity structure of the crystals. The hydrothermally-grown material is also reported [26] to have a laser-damage threshold of 30 GW/cm^2 for 30ps pulses at 10 Hz at 526nm, some 3 times greater than that for flux-grown KTP under similar conditions. This is speculatively related to the incorporation/exclusion of Ti^{3+}, which promotes conductivity, without necessarily requiring the presence of K^+ movements.

The two growth methods, whilst ultimately producing crystalline KTP, thus give that material rather different qualities, which in turn affect the end-use possibilities for devices.

1.2.3 KTP Structure.

KTP belongs to the point group *mm*2, polar space group $Pna2_1$, and is ferroelectric[24]. It is orthorhombic, with eight formula units in the unit cell and with lattice parameters a=12.819Å, b=6.399Å, c=10.584Å[27]. Its structure was first determined in 1974 by Tordjman, Masse and Guitel[28] and can be seen symbolically in Figure 1.3.

The structure is characterised by a framework of TiO_6 octahedra and PO_4 tetrahedra linked at the vertices. The K ions, that occupy cage sites, are co-ordinated with eight or nine O atoms, and loosely bonded to the framework. The two distinct K ion sites have an average O-bond length of 2.84Å and 2.94Å respectively. The two Ti octahedra per formula unit possess similar distortions which make them tetragonal, because the Ti atom is strongly shifted towards one of the oxygen atoms along its bond, twisting the octahedra (see Figure 1.4).

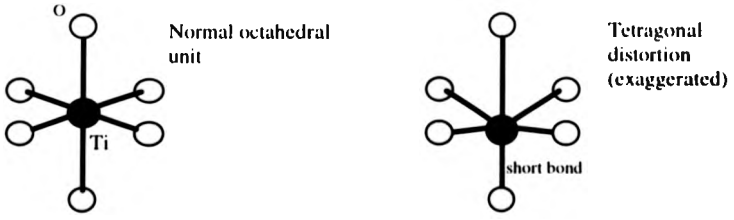

Figure 1.4 Diagram showing tetragonal distortion in a TiO_6 octahedron

Notably, the chains of Ti-O bonds that run approximately in the c- direction (with a path along [0 1 1] and [0 $\bar{1}$ 1]) through the TiO_6 octahedra series have adjusted lengths because of this octahedral distortion, such that long and anomalously short bonds (see table 1.1) run in series along c, giving rise to an asymmetric electronic environment around the Ti atoms and a net polarisation of the structure in the c-direction. The high electro-optic and non-linear-optic coefficients of KTP are generally attributed to this asymmetry in the Ti-O bonds[28], and since the short bonds are noted for their covalent character, the surplus electron density here may account for the magnitude of KTP's non-linearity.

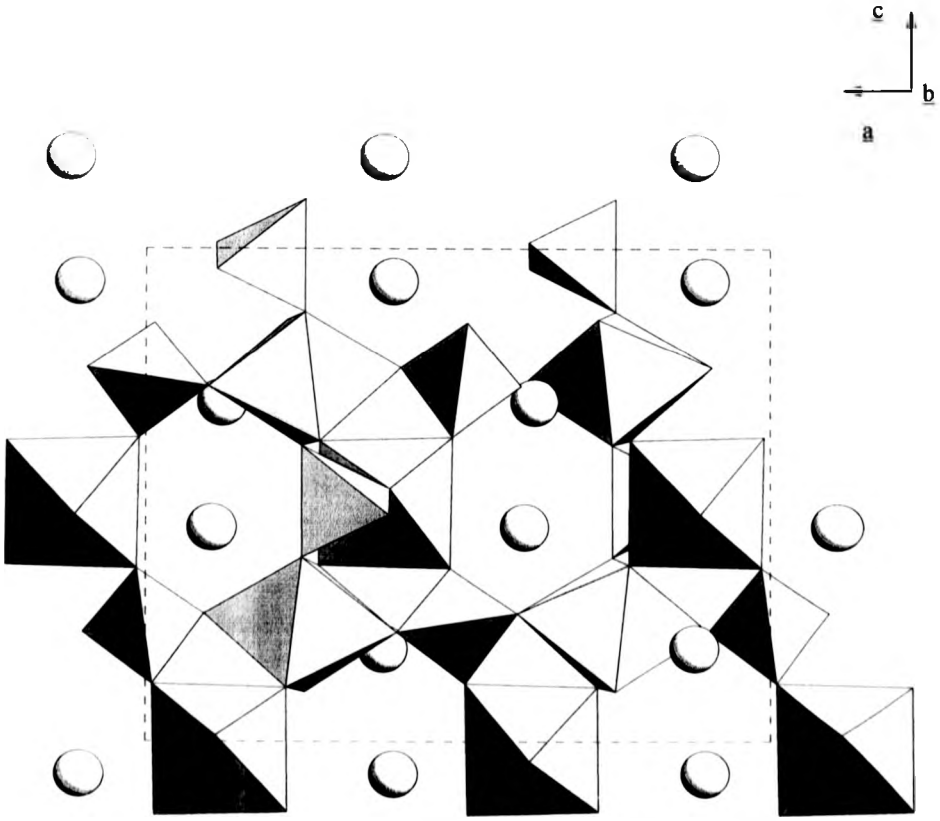

Figure 1.3 Schematic representation of the unit cell of KTP. The octahedra are the TiO_6 groups, the tetrahedra are the PO_4 groups, and the spheres are the K atoms in cage sites.

Ion	Bond lengths: *short*	*long* (Å)
Ti (1) (*trans*)	1.716	1.981
Ti (2) (*cis*)	1.733	2.092

Table 1.1 Bond-length parameters for the Ti-O chains in KTP

Along the c-axis are also found channels, which spiral through the whole structure of a macroscopic crystal. Through these, motion of the K ions can occur by a vacancy mechanism if a suitable E-field is applied, which offers one possible route for structural modification by indiffusion of new ions. Ionic conductivity studies also show that the DC conductivity along the *c* axis[29] is 4 times greater than that along the *a* or *b* axes because of this mobility.

Twinning in KTP has been seen. The twinning can be derived using the characteristic 'hole-sites' which are pseudo-symmetrically related to the site of the K atoms in the room-temperature structure. The holes are voids, actually part of the spiral-channels described above. Where the K ions are pushed through the structure to the hole site, they take the surrounding structure with them, twisting the octahedra and tetrahedra such that an inversion domain is created, and relative to the untransformed nearby structure, a twin is formed. The twin is a simple inversion-twin, resulting in domain-inverted behaviour in different parts of the crystal.

1.2.4 Limitations of pure KTP

KTP is an excellent technologically-proven NLO material, displaying qualities that set it apart from other inorganic materials. It does, however, possess specific limitations. KTP's birefringence is too small for frequency doubling of light below 994nm[30], which limits its value as a multiple-λ frequency-doubler, in particular in blue-SHG technologies. More particularly, the birefringence is such that the walk-off during type-II phase matching (where ordinary and extra-ordinary rays for pump and SHG light are divergent along crystallographic axes)

is still significant enough to reduce conversion efficiency.

The SHG wavelength-acceptance is also subject to other limitations. In hydrothermally-grown KTP, absorptions in the transmission spectra (at 2800nm) are attributed to O-H bond-stretching from incorporated water[31]. The sharp cut-off in the UV region found in both growth-types at 370 nm, thought to be due to the Ti-O bond absorption, also limits the wavelength windows. The absorption remote from this band-edge is also significant[32,33]: in the 500nm range it is ten times greater than at the 1μm range (around 1% cm^{-1}) which is technologically problematic, since for pumping at 1.06μm from Nd:YAG, KTP upconverts to the green at 532nm - its most useful property.

Hence green SHG is not optimal, and blue SHG from un-poled KTP is not a viable proposition. Blue output is possible through sum-frequency generation, but since this is technologically more demanding it is less attractive for compact blue-optics. For SHG into this wavelength region, the birefringence of KTP must be modified, and extensions made to the cut-off wavelength.

1.2.5 Device-modified KTP

The modification of KTP-family materials into devices for integrated optics has further extended the value of the materials, overcoming some of the limitations outlined in section 1.2.4. The modification is generally in the form of altered surface layers, forming waveguide optics: the indiffusion of ions into the surface after immersion in a nitrate bath doped with ions such as Rb, Cs, Tl[14], adjusts the structure of the KTP in a shallow surface layer which can possess improved NLO qualities. The advantage of such waveguide optics is mainly in confining the input and output light in a narrow interaction zone, such that energy transfer is maximised.

This technology is beyond the scope of this thesis, but the research performed here has relevance to the structural effects of modified-KTP device construction.

1.3 Doping of KTP

KTP is just a single member of its larger family. Whilst other members possess useful material and NLO characteristics (such as KTA, rubidium-KTA, and rubidium-KTP for example), slight modification of KTP itself is both possible and desirable to preserve the useful character of KTP in the resultant materials.

1.3.1 Doping mechanisms

Doping of KTP with substitution on the K site is possible (even up to 100%), producing such materials with modified non-linear optical responses as KNTP ($K_{1-x}Na_xTiOPO_4$)[35] and KRTP ($K_{1-x}Rb_xTiOPO_4$)[15]. The incorporation of ions such as these is pursued because they possess different polarisability from K. But the structural modification compared to pure KTP is marked due to the different ionic radii, and different growth morphologies are thus observed in materials with significantly different material and non-linear optical properties from KTP. For example, KNTP has poor NLO characteristics, whilst RTP's are approximately the same as KTP.

In KTP, the dopants can also occupy the Ti sites, and numerous family members with the formula: $KM_xTi_{1-x}OPO_4$ are possible, where M is Nb, Ta, Ga, Cr, V, Sc and others, and x varies, typically up to 0.5 for Nb-doped KTP (hereafter denoted Nb:KTP*[1])[36] although complete substitution is sometimes possible (i.e. achieving another family member from the KTP group). Various of these ions are observed to have higher take-up into the crystal than others, with for example, Ta being easier to incorporate than V[17].

Production of these doped analogues of KTP is generally achieved by single crystal flux-growth. The dopant ions are introduced in their oxide form as flux-components, and are then simply incorporated into the structure during the growth of the crystal. Growth generally proceeds as expected for pure KTP, and

*[1] The notation M:KTP will be used to denote samples of KTP where small percentages of dopant ion M have been introduced, as distinguished from materials where a greater percentage substitution of the ions results in a material more directly identifiable as KMP, or KMTP. The M:KTP materials are produced in general to modify the NLO performance from KTP's whilst preserving the excellent properties of the pure material.

seeding of the growth is possible, even using pure KTP seeds, since the process tolerates small structural mismatches by forming a mass of defects close to the seed crystal, until growth of an undisturbed crystal is established (see Figure 1.5).

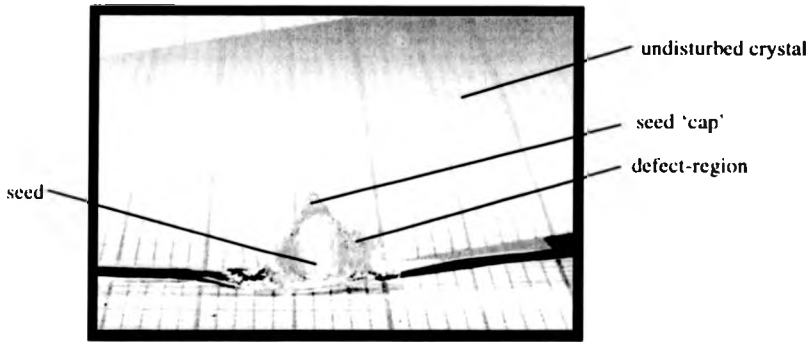

Figure 1.5 Photo of imperfect region surrounding seed in flux-grown KTP.

Within the scope of this thesis, the doping process has one main aim: to modify the optical indicatrix and hence birefringence of the material in the (001) plane relative to pure KTP. This is to extend the SHG wavelength acceptance of the material, such that the birefringence is extended in the blue spectral region. The sensitivity of the SHG process to variations even in the 4th dp of the refractive indices is known, and thus the slight modifications to the birefringence of KTP caused by structural-modification in doping can, in theory, be carefully controlled to produce a material with new, specifically-defined characteristics. For example, the sensitivity of the birefringence of KTA to Fe impurity is known (making the material phase-matchable, which it isn't otherwise), and KTP suffers similar sensitivity. Fe^{3+} is a common impurity at a level of ≈5ppm[38], and thus by deliberately doping KTP with Fe, modifications to the birefringence should be possible.

The doping process also is aimed secondarily at producing materials with modified ionic conductivities compared to pure KTP, since this characteristic defines the poling-capabilities of the crystal[38] and possibly the damage response.

1.3.2 The impact of doping

By doping KTP, the individual bonds within the unit cell are modified. The ion radii of dopants such as Nb and Ta vary from those of the Ti ions, and are generally incorporated in different oxidation states to the host Ti^{4+}, see table 1.2. Inclusion of the dopant ion thus induces strain and localised charge-balance violations, which are possibly compensated for by regionalised K vacancies allowing a doping tolerance for even very large, charged ions, such as Nb.

Ion	Radius (pm)
Ti^{4+}	60.5
-----	-----
Ta^{5+}	64
Nb^{5+}	64
Ga^{3+}	62
V^{5+}	54
Nd^{3+}	99.5

Table 1.2 Ionic radii of some typical ions used in KTP Ti-site doping, derived as 'effective' ionic radii by Shannon and Prewitt[39]

Inclusion into the TiO_6 octahedra of these ions results in slight angular variations which modify the geometry of the octahedra and hence the anomalous short/long Ti-O bonds. Notably, for the case of Nb-doping, in the adjusted Ti octahedra the Ti is observed to be more centric in doped KTP than in the pure material[40], though since the atomic shifts are only fractions of 1%, major structural alteration does not seem to be the cause of the birefringence modifications. The location of the electronic structure of the dopant ions is more likely to be responsible for modified non-linear response: if the surplus electron density found at the short Ti-O bond is adjusted, then the overall optical response will be modified too.

By considering a classical spring-model of the Ti sites in their octahedra, the physical modifications induced by doping become apparent. Changing the ion for a more polarisable one (softer springs) and modifying the octahedral geometry slightly will change the anharmonic response of the ion, and thus its

non-linear characteristics. The incorporation of these dopant ions, altering the geometry of the Ti-octahedra, results in a modification to the anharmonic potential that describes the motion of electrons in the Ti-O bonds, and hence to the χ coefficients of the material. Also, the ionic polarisability of the dopant ions is generally much larger than that of Ti, and this is significant for modification since it also determines the anharmonic response of the polarisation and changes the linear refractive indices.

1.3.3 Ti-substituted KTP derivatives

Niobium-doped KTP was first reported in 1990[40]. Its growth from a flux produces crystals of a fairly typical KTP morphology, though there is a significant tendency to form shallow plate-like crystals heavily contaminated by flux inclusions and defects. Structural refinement[40] suggests that the Nb ions preferentially occupy the Ti (1) site (see section 1.2) in a slightly less distorted environment than for pure KTP. The presence of K vacancies was also noted, appearing to cause slight structural modifications as well as charge compensation. The Ti-O anomalous bonds remained in a long/short alternate configuration along the polar axis. Later work[36] reported bulk SHG into the blue spectral region from samples of single-crystal Nb:KTP of various dopant concentrations (between 1 and 12%). In all these concentration-variants, significant birefringence enhancements (of up to 20%) over pure KTP's were noted. Also, SHG experiments noted a 100nm blue-shift in the SHG cut-off wavelength for a 12% Nb-doped sample, which is a highly desirable characteristic. The increased centricity of the Ti site was again noted, though the increased ionic polarisability of Nb over Ti was considered to be the main contribution to the increased birefringence. Tantalum doping of KTP was also reported in the same paper [36] but was described only in terms of its 'significant' modification of the birefringence over pure KTP.

Scandium-doping of KTP[41] was attempted to produce a novel periodical-poling in KTP for waveguiding purposes. Trivalent Sc was incorporated during flux-

growth at 925°C, resulting in doping levels in the region of 200ppm, including small contaminations of Na. Poling was possible for lower Sc levels, but the highly doped material resulted in frustrated poling. For the poled material, blue SHG was reported as up to 30% more efficient than in undoped (poled) KTP, with a slight improvement in recovery after optical damage. For a higher doping of 230ppm, the ionic conductivity was found to be approximately a factor of 30 lower than undoped KTP, whilst c-axis conductivity for 120ppm Sc:KTP was approximately that of pure KTP. The morphology of all Sc:KTP crystals has been seen to be distorted compared to pure KTP's.

Cerium doping of KTP has also been reported[42]. This paper describes the effects of joint Ce-doping and oxygen annealing of KTP, and particularly notes the resulting extension of the transmissivity of Ce:KTP into the UV region. The intention of both processes was to decrease the ionic conductivity of the material. The crystals were produced again by top-seeded flux growth, involving dopant levels of up to 2% Ce (by mass). In the resultant crystals, a distinct yellow cast was noted, and experiments showed a slight increase in their Curie temperature relative to pure KTP (up to 949°C). Optical SHG analysis noted a blue-shift in the UV cut-off and a modified phase-matching angle (consistent with birefringence modification). These characteristics match those required for extending the device-utility of KTP. Oxygen annealing is performed with the intention of increasing take-up of the Ce atoms, since the atom alone seems difficult to force into the KTP structure.

The team of McGee, Blom and Kostecky[37] report successful doping of KTP by a variety of ions, including Cr, V, Ga, and Al. Their experimental work was centred on successful production of such materials by flux-substitution techniques, and to optimise this process, and generally involved the use of ions required to lower the ionic conductivity. These ions were of lower valence than Ti, to charge-compensate for the loss of O_2, so reducing K vacancies. Their aim was to lower the conductivity of flux-grown KTP toward that of hydro-thermal KTP with the increased resistance to laser-damage this would bring. This result

was found successfully for ions of Ga, Al and Cr in some concentrations, though incorporation of Li proved impossible. They also noted the formation of green colour-centres in both V and Cr-doped KTP, and showed that this was due to new absorption bands between 400 and 700 nm. This research did not approach analysis of the structural features of these doped analogues of KTP, nor the implications for the birefringence or non-linear optical response, and thus is useful only to suggest that incorporation of ions of greatly-different valence and radii are possible, which can be used as an argument reinforcing the usage of co-doping to modify KTP since in this case ions of greatly different properties are introduced simultaneously.

It is clear that cationic doping of flux-grown KTP by numerous ion combinations has been demonstrated, with differing degrees of successful growth-quality. Modified structure, birefringence and non-linear optical response have been shown for various of these new materials, and in some structure-property relationships have been demonstrated. The process of cation doping of KTP is thus assured as a means of modifying the material properties in a controlled way to produce a new material with pre-desired characteristics and the proven benefits of the KTP class.

1.3.4 Summary for doped KTP

The pursuit of modified KTP has produced a variety of doped materials as described, with varying degrees of success in terms of growth morphology and adjusted NLO parameters. The incorporation of a few percent of a dopant ion on the Ti sites in the KTP structure allows a large number of potential new materials; a number which is increased when co-doping is considered.

This process involves the introduction of a further dopant ion into the structure, usually during the same flux-substitution method. This second ion is included to minimise the undesirable effects caused by the main ion, such as unfavourable growth-morphology, increased conductivity or susceptibility to laser damage. The second ion behaves as a charge-compensation mechanism, or facilitates

incorporation of the first dopant ion during growth. In the case of Ta/Ga co-doping for example, the intention of including gallium is both to increase the incorporation of the Ta ions into the crystal and to reduce ionic conductivity: other ionic arguments can be developed for other doping schemes.

There is also a possibility that doped KTP-variant can lase and upconvert in the same device. This could be achieved in the production of Nd:KTP, for example, though the inclusion of Nd and other suitable ions is not consistently achieved - generally since the Nd ion is approximately twice the radius of Ti^{4+} (see table 1.2). Incorporation of Er ions would provide a similar material, and successful Er doping has been achieved for this to a limited extent[43].

The main difficulty found in doping of KTP is that the quality of the crystal produced varies both with the dopant ion and its concentration. Many crystals produced in this way are found to possess yellow/green discolorations (signifying absorption bands at optical frequencies) or to possess large numbers of inclusions, fractures and surface striations. In extreme cases, e.g. Nb:KTP, the familiar KTP growth morphology is almost destroyed, leaving multiple-plate-like crystals[40]. In particular, frustration of the [100]-growth facet often occurs, such that growth proceeds as expected along the other growth facets, but barely exceeds the *a*-dimension of the seed crystals. This is a significant problem, since this direction is approximately the propagation direction for SHG, and thus the path-length, and hence SHG efficiency, is potentially limited by the available size of device crystals.

A difficulty from the point of view of novel-material production is that whilst it is relatively easy to identify candidate ions because of their existing characteristics, achieving incorporation of these ions into the structure of KTP is not assured, either due to ionic-radii problems, or energetic problems at the growing surfaces. This means growth can be a speculative process.

1.4 Scope of this thesis

Section 1.3 outlines cases of successful doped KTP, with a variety of dopant ions and different degrees of success in terms of growth and modified NLO responses. The attraction of the doped KTP variants has led to numerous experiments designed to produce efficient growths, or to analyse the NLO properties of crystals of the new materials. Structure-property relations have been investigated for some variants. The variants Nb:KTP and Ta:KTP[36,40] have been investigated, resulting in an understanding of the structural and NLO features of Nb:KTP and some of the NLO parameters of Ta:KTP. Both of these materials are particularly interesting since they can be grown with success, and possess desirable optical properties. A study of the crystalline quality of the materials had not been performed, and this is an important consideration if the materials are to be commercially useful, since the presence of high-density defects or domains can lower the materials' NLO efficiency. In this thesis, a high-resolution diffraction study is made of samples of Nb:KTP, Ta:KTP, and co-doped TaGa:KTP to gain an understanding of the structural quality of the flux-grown samples. The Ta:KTP samples were subjected to structural analysis, such that the solved structure would complement previous Nb:KTP structural work, and could be useful to future interpretation of the properties of the material. A simulation of the refractive index parameters for the material was also carried out to gain an insight into the structural features that contribute to the material's optical behaviour. Finally, the opportunity for synchrotron analysis was used to perform topographic studies of Ta:KTP and TaGa:KTP materials such that further information on their defect structures was obtained.

The improved structural and defect-structure understanding is designed to feed into the ongoing research effort into producing high-quality, feature-engineered doped KTP, since it can be used to gain improved understanding of the structural contribution of the doping ions.

1.5 References

[1] P.A. Franken, A.E. Hill, C.W. Peters, G. Weinrich. *Phys. Rev. Lett.* **7**, (1961) 188

[2] "Lasers and Electro-Optics, Fundmentals and Engineering" C.C. Davis, Cambridge University Press (1996)

[3] D.G. Sun, C. Zhao, R.T. Chen. *Proc. SPIE* **3005**, (1997) 212

[4] Y. Zheng, Y. Wang, V. Petrov, Y.J. Ding, J.B. Khurgin, W.P. Risk. *Conf. on Lasers and Electro-Optics Europe -Tech. Digest.* (1998) 73

[5] D.C. Grillo, M.D. Ringle, G.C. Hua, R.L. Gunshor, A.V. Nurmikko. *J. Vac. Sci. & Tech. A* **13**, (1995) 681

[6] "Physical Properties of Crystals" 2nd Ed., J.F. Nye, Oxford University Press (1985)

[7] R.I. Ristic, B.Y.Shekunov, J.N.Sherwood. *J. Cryst. Growth* **167**, (1996) 693

[8] W.L. Zhou, Y. Mori, T. Sasaki, S.Nakai. *Optics Comm.* **123,** (1996) 583

[9] J.A. Armstrong, N. Bloembergen, J. Ducing, P.S. Pershan. *Phys. Rev.* **127,** (1962) 1918

[10] Z. Li, B. Wu, G. Su, G. Huang. *Appl. Phys. Lett.* **70**, (1997) 562

[11] F.Q. Meng, M.K. Lu, Z.H. Yang, H. Zeng. *Mater. Lett.* **33**, (1998) 265

[12] L. Ouvard. *Compt. Rend. (Paris)* **111**, (1890) 117

[13] R. Masse and J.C. Grenier. *Bull. Soc. Franç. Mineral. Crist.* **94**, (1971) 437

[14] F.C. Zumsteg, J.D. Bierlein and T.E. Gier. *J. Appl. Phys.* **47**, (1976) 4980

[15] L. K. Cheng, L. T. Cheng, J. D. Bierlein, J. Parise. *Appl. Phys. Lett.* **64**,

(1994) 1321

[16] P.E. Perkins, T.S. Fahlen. *J. Opt. Soc. Am. B* **4**, (1987) 1066

[17] H. Kiriyama *et al. Proc. SPIE* **2700,** (1996) 262

[18] G. Huth and D. Kuizenga. *Lasers Optron.* **6,** (1987) 59

[19] T.A. Driscoll, H.J. Hoffman, R.E. Stone, P.E. Perkins. *J. Opt. Soc. Am. B* **3**, (1986) 683

[20] J. D. Bierlein, H. Vanherzeele. *J. Opt. Soc. Am. B* **6**, (1989) 622

[21] M. G. Roelofs. *J. Appl. Phys.* **65** (1989) 4976

[22] C.A. Ebbers, S.P. Velsko. *Appl. Phys. Lett.* **67,** (1995) 593

[23] V. K. Yanovskii, V. I. Voronkova. *Phys. Status Solidi A* **93,** (1980) 665

[24] Y.S. Liu, L. Drafall, D. Dentz and R. Belt. *Proc. Tech. Conf. on Lasers andElectrooptics*, Washington DC, June 1981, p.26.

[25] G. Rasenman, private communication.

[26] H. Vanherzeele, J.D. Bierlein, F.C. Zumsteg. *Appl. Opt.* **27**, (1988) 3314

[27] P.A.Thomas, A.M.Glazer, B.E. Watts. *Acta Cryst B* **46,** (1990) 333

[28] I. Tordjmann, R. Masse, J.C. Guitel. *Z. Kristallogr.* **139,** (1974) 103

[29] V.K. Yanovskii, V.I. Voronkova. *Soviet Phys.-Solid State* **27,** (1985) 1308

[30] W.P. Risk, R.N. Payne, W. Leith, C. Harder, H. Meier. *Appl. Phys. Lett.* **55**, (1989) 1179

[31] J.C. Jacco, G.M. Loiacono, M. Jaso, G.Mizell, B. Greenberg. *J. Cryst. Growth* **70**, (1984) 484

[32] R.F. Belt, G. Gashurov, Y.S. Liu. *Laser Focus* **21,** (1985) 110

[33] D.J. Gettemy, W.C. Harker, G.Lindholm, N.P. Barnes. *J. Quantum Electron.* **24,** (1988) 2231

[34] J.D. Bierlein, A. Ferretti, L.H. Brixner, W.Y. Hsu. *Appl. Phys. Lett.* **50,** (1987) 1216

[35] G. M. Loiacono, R. A. Stolzenberger, D. N. Loiacono. *Appl. Phys.* **64,** (1994) 16

[36] L. K. Cheng, L. T. Cheng, R.L. Harlow, J.D.Bierlein. *Appl. Phys. Lett.* **64,** (1994) 155

[37] T.F. McGee, G.M. Blom, G. Kostecky. *J. Cryst. Growth* **109,** (1991) 361

[38] P. A. Morris, A. Ferretti, J. D. Bierlein. *J. Cryst. Growth* **109,** (1991) 367

[39] R.D. Shannon, C.T. Prewitt. *Acta Cryst. B* **25,** (1969) 925

[40] P. A. Thomas, B. E. Watts. *Solid State Commun.* **73,** (1990) 97

[41] M.J. Jongerius,R.J. Bolt, N.A. Sweep. *J. Appl. Phys.* **75,** (1994) 3316

[42] P.F. Bordui, R. Blachman, R.G. Norwood. *Appl. Phys. Lett.* **61,** (1992) 1369

[43] K.M. Wang, M.Q. Meng, F. Lu, X.D. Liu, T.B. Xu, P.R. Zhu, D.Y. Shen, Y.H. Tian. *Mat. Sci.&Eng. B* **52,** (1998) 8

Chapter 2

Crystals and X-ray Diffraction.

2.1 Crystals

2.1.1 Crystal structure.

A crystal can be defined using only two mathematical ideas: the infinite repeating lattice, and convolution of this lattice with a motif[1]. Strictly, an infinite lattice **L**(r) consists of spatially-repeating delta functions in up to 3 dimensions. The motif, **B**(r) or "basis", is an object convoluted with this lattice such that a copy is made of it at each delta-function, or lattice point, and only at such points:

$$\mathbf{C}(r) = \mathbf{L}(r) * \mathbf{B}(r) \qquad (2.1)$$

A real crystal does not have infinite extent, so a "shape function", **S**(r), is included to limit the spatial extent of the crystal to provide a more realistic model. Inside the crystal **S**(r) has the value 1, outside 0:

$$\mathbf{C}(r) = (\mathbf{L}(r) * \mathbf{B}(r)) \wedge \mathbf{S}(r) \qquad (2.2)$$

The function **C**(r) now describes a crystal: and the basis describes the physical nature of the crystal. Any article can be used as a basis, but generally a "real" crystal is considered to have a basis consisting of atoms, ions or molecules, and this is what is described when referring to a 'crystal'. Whatever the basis, one of the most important features to arise from this definition is the idea of symmetry within the lattice.

2.1.2 Symmetry, unit cells and real crystals.

A symmetry operation is a mathematical operation that operates on an object, e.g. a lattice, and maps it onto itself - the simplest symmetry operator is the identity. Other operations involve glides, rotations, translations, screw axes,

mirrors and inversions and multiple combinations of all of these. The one constraint is that the permitted symmetry operations for a particular lattice are decided by its particular geometrical properties. In a strict group-theory analysis of the permitted operations that can be performed on a 3-dimensional lattice, only 32 different point groups can exist. Combined with the 14 permitted 3D lattices, the product is a set of 230 permissible space groups[2]. They are all categorised and described in the International Tables for Crystallography[3] (ITFC).

A real crystal's structure is maintained by the bonds between the atoms or molecules that constitute its basis. A fundamental unit cell of a small number of positioned atoms can be considered, and it is the repeat of this cell throughout the volume of the crystal that makes up the crystal itself. The unit cell must therefore obey the symmetry properties of the lattice. It is logical to draw the conclusion that physical properties of the crystal obey certain symmetry operations too - this is the Neumann principle, and has important implications for non-linear optics (see Chapter 1).

Thus we have arrived at the idea of a finite structure of systematically located ions/atoms/molecules possessing a characteristic symmetry as constituting a 'real crystal'. The symmetry is directly related to the physical properties a particular crystalline material will possess, and is, of course, the source of the consistency in physical habit between different samples of the same crystal.

The periodic nature of real crystalline structures permits investigation of their properties by various methods using x-rays, neutrons and electrons in diffraction experiments. Since x-ray wavelengths (order Å) are consistent with interatomic spacings (typically several Å), and x-rays are relatively easy to produce in a laboratory environment, then x-ray crystallography is the most common method of investigation of crystalline structures. Modern x-ray sources, including synchrotrons, combined with sophisticated computerised data-processing also make x-ray crystallography an extremely powerful investigative tool.

2.2 X-Rays and crystals

2.2.1 Lattices and diffraction

By orientating a 3-D lattice, the existence of regularly-spaced planes becomes apparent. In a real crystal, the direct equivalent is found as a series of regularly-spaced atomic planes. Since the electronic character of these atoms must also follow the regularity, then a series of planes of electron-density can be assumed to exist within a crystal, with various spacings and orientations caused by the particular symmetry and parameters of the crystal's unit cell. Since x-rays interact with charged particles, if the wavelength of an x-ray is of the same order of magnitude as the spacing between these planes then it can be seen how x-rays can diffract in interaction with crystalline structure.

X-rays scatter as they interact with electrons via the Thomson effect. Since the electrons act as a periodic scattering array, then diffraction occurs in much the same way as for light through an optical grating, with ongoing waves interacting after scattering, generating a diffraction pattern that is characteristic of the crystal.

Bragg's equation describes the conditions necessary for diffraction:

$$n \lambda_x = 2d_p \sin \theta \qquad (2.3)$$

(λ_x being the x-ray wavelength, d_p being interplanar spacing, θ being the angle of reflection) by describing the reflection of an x-ray beam from a plane within a crystal.

In real diffraction experiments, the crystal is carefully rotated such that the incident x-rays meet the reflecting planes within the crystal at the Bragg angle. The resultant diffraction 'spot' is sampled by a detection system, which could be as simple as a sheet of x-ray sensitive film. For each particular set of planes that can diffract within a crystal structure, a distinct Bragg angle exists and a diffraction spot, or 'reflection' can be formed from the ongoing x-rays if they are orientated correctly. Clearly there is some geometric relation between the real

space where the planes are orientated relative to the x-rays, and the space where the diffraction spots are related to each others' position. This latter space is known as diffraction, or reciprocal space.

2.2.2 Reciprocal space and the Ewald sphere

Reciprocal space is related to real space by the action of a Fourier transform, and another transform returns reciprocal-co-ordinates to real space. A plane in real space is transformed by a Fourier transform to produce a line perpendicular to the plane in reciprocal space, and the Fourier transform of an infinite stack of regularly spaced, mutually parallel planes is a point in reciprocal space - a semi-infinite stack of planes, however, will produce a point that has some finite extent.

Applying this to a real crystal: for every set of diffracting planes within a crystal, there exists a point in a reciprocal diffraction space that corresponds to the diffraction 'spot' (specifically its geometrical position). A reciprocal lattice therefore exists which describes all of the points corresponding to families of planes in the real crystal, and since these are related by symmetry operations, then the reciprocal lattice must possess the same symmetry as the real one. However, in reciprocal space length-scales are inverted, so two objects separated in real space by the distance d have reciprocal space equivalents separated by the distance $1/d$. Combining this idea with Bragg's law leads to the construction of the Ewald sphere.

A sphere of radius of $1/\lambda_{x\text{-ray}}$ is constructed in reciprocal space such that the x-ray beam passes through its centre, C (Figure 2.1). The set of diffracting planes sits at C, and is parallel to the line l. If the origin of the reciprocal lattice is assumed at O, then when the vector $\underline{r}^*$ (which describes the scattering vector mapping incident to reflected x-ray beam) lies at the intersection of l and the sphere, the planes of the crystal will make an angle θ with the x-ray beam, meeting the Bragg condition since:

$$OP = |O| \sin\theta = 1/d_{planes} = 2 \sin\theta/\lambda_{x\text{-ray}} \qquad (2.4)$$

So, the condition necessary to achieve strong Bragg reflection from a particular family of planes is that the scattering vector $\underline{r}^*$, corresponding to the particular

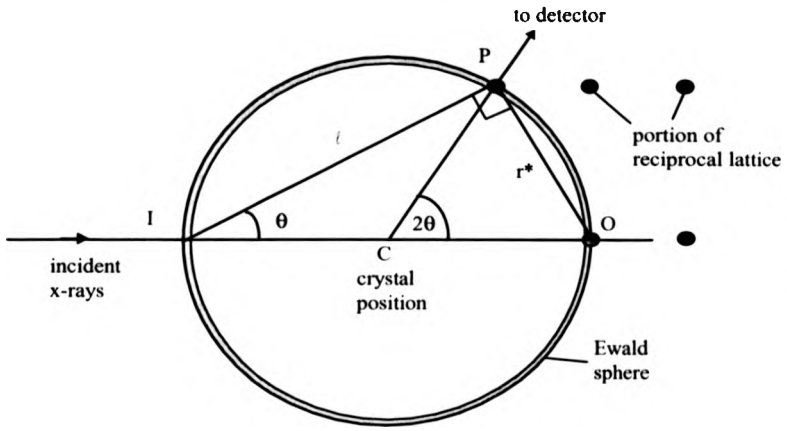

Figure 2.1 The Ewald sphere (in 2D projection onto diffraction plane)

reciprocal lattice point (RLP) of that reflection, crosses the Ewald sphere.

2.3 Diffractometers

Diffractometers comprise three main elements: a source of x-rays, an x-ray detector, and a manipulation system (goniometer) which can position the source, sample and detector such that x-rays are diffracted. Diffractometers can have different designs, sampling reciprocal space in various different ways, but all are capable of compelling one or many RLP's to cross the Ewald sphere, and thus allow x-rays to be diffracted and detected. The reciprocal points so collected can be used to generate different kinds of data about the crystal structure itself, from the atomic positions in the unit cell to the details of its perfection on a larger scale. For different requirements either single or multiple RLP data are collected, with either intensity or angular position being the more important. Two main types of sample are typically used: in powder diffraction a powdered sample's random orientation is used to simplify the manipulation needed for data collection, since the need for sample orientation is removed. In single crystal diffraction, where a single large (e.g. up to $1mm^3$) crystal is exposed to x-rays,

more operations are required for useful diffraction to occur.

If the experiment uses a white x-ray source, for example in a home-experiment, much used for protein crystallography, then many Ewald spheres can be imagined to be intersecting at the origin of reciprocal space - Figure 2.2. All of the shaded region of reciprocal space is useful for sampling RLPs. This is the condition required for Laue diffraction, which is useful since the experiment allows diffraction for numerous RLPs at once as their various inter-planar species select different wavelengths from the source.

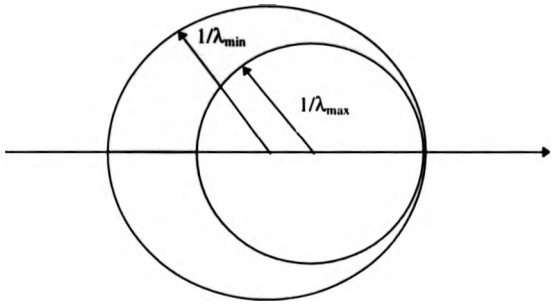

Figure 2.2 Ewald sphere for polychromatic x-ray source

Similarly, if the incident beam is monochromatic, but has significant angular divergence from the source, then the condition of Figure 2.3 is met, with the overlap between the two extreme Ewald spheres being the significant diffraction zone.

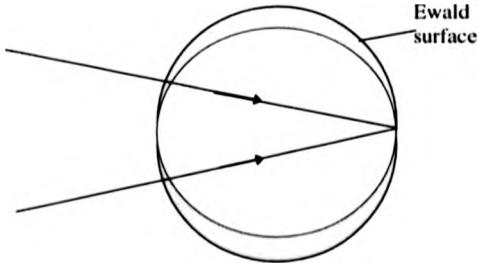

Figure 2.3 Ewald spheres for divergent source geometry

For a structure-determination experiment it is necessary to collect the intensity from many reflections along with data about their location in reciprocal space, such that this information can be passed on to a refinement program that refines the structure of the crystal being examined. Under such conditions a resolution $\Delta d/d$, expressed as about one part in 10^4, suffices. In this case the sample can be in powdered or single-crystal form for diffraction purposes. A four-circle diffractometer, named for its axes of manoeuvrability as shown in Figure 3.1 (chapter 3), can be used for such an experiment. A similar diffractometer (Figure 2.4) with an area-detector (which can collect lots of reflections simultaneously) is also a viable device. The x-ray beams used in such diffractometers require only moderate conditioning so that they do not introduce artefacts into the experiment. A simple monochromator, such as a graphite single-bounce monochromator, and a detector with a reduced sensitivity to background scattering is all that is necessary to condition the Ewald sphere such that the intensity and position of reflections are sufficiently defined.

If the structure of the RLP itself is of interest, then different criteria apply. The interest is raised when specific characteristics, e.g. defects or domains, in the crystal extend the RLP from its ideal point (see 2.2.2). When examining such RLP's, accuracy of positioning of sample and detector become important, and a well-defined reciprocal-space probe is needed to perceive the details of the RLP. Fewster[4] defines the criteria necessary for such a diffractometer. Beam conditioning before and after interaction with the sample is needed to modify the Ewald sphere and detector to produce the high-tolerances necessary to resolve features in the RLPs that may only be of order arc-seconds in width.

These two different end-uses require vastly different diffractometer design. An overview of one of each type follows.

2.3.1. Diffractometer for Structure-Determination.

An example of an efficient structure-determination diffractometer is one that combines a kappa goniometer (i.e. a manipulator with a fixed χ angle of 57°)

with a charge-coupled device (CCD) area-detector, as represented by Figure 2.4. This means that the diffractometer has only two degrees of angular freedom, but is able to sample large sections of reciprocal space in a single frame. The single-crystal sample is in the form of a randomly oriented sphere, mounted on a fibre at the centre of the diffraction stage, and can be rotated about both its own axis (ϕ) and ω to bring different sets of reflections into the detector, which can itself be rotated (to a few different 2θ positions, to cover low and high-angles).

The area detector acquires a particular frame and a computer analyses the position and intensity of x-rays detected across the frame. In a typical experiment, some preliminary reflections are gathered, and an initial orientation matrix is generated by refinement. This is used to locate the axes of the crystal with respect to those of the diffractometer, and gives a first approximation of the unit-cell parameters.

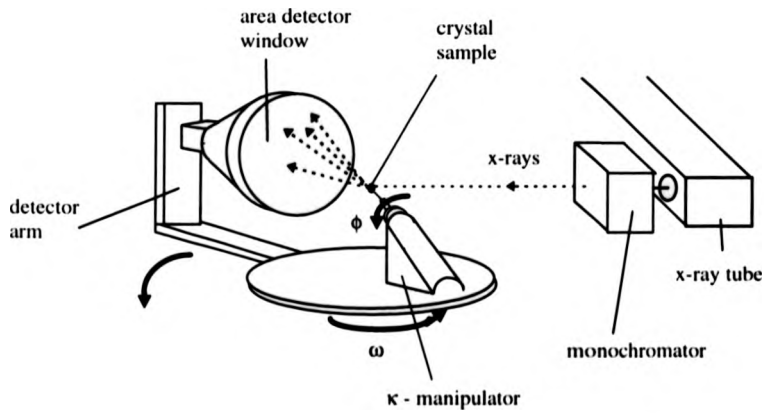

Figure 2.4 Schematic diagram of an area-detector diffractometer.

Within the scope of this thesis a good starting model for the structures studied exists and, using this as a basis, structural refinement is performed by computer, using a program such as CRYSTALS[5], which takes some initial model parameters (lattice parameters, space group, atomic co-ordinates) and operates

on the data to achieve a final, refined, structure. Programs like this first step through the raw diffraction data, removing extraneous reflections which are absent, or unobserved. The final outcome is determined by the user, who moderates the progress of the refinement by testing various variables of the model until they are within acceptable limits and a chemically-plausible structure is achieved.

2.3.2. High-resolution Diffractometer

2.3.2.1 Background

Figure 2.5 shows a schematic of a Philips high-resolution single-crystal diffractometer that uses a four-circle goniometer to position the detector and sample relative to the incident x-ray beam. The two circles ω and 2θ lie in the plane of diffraction, in which the x-ray beam is already conditioned by a monochromator (ϕ and ψ circles are found at ninety degrees to this plane, and allow for accessibility to different reflections, though chi is limited to ±10°). Rotations about these axes allow positioning of sample and detector, with respect to the incident x-ray beam, to allow access to large sections of reciprocal space. The advantage of such a diffractometer over 2-circle diffractometers is that for a single sample, a greater area of the diffraction space can be covered in one experiment, and this flexibility is advantageous where samples are small, difficult to produce or prepare, or are otherwise valuable.

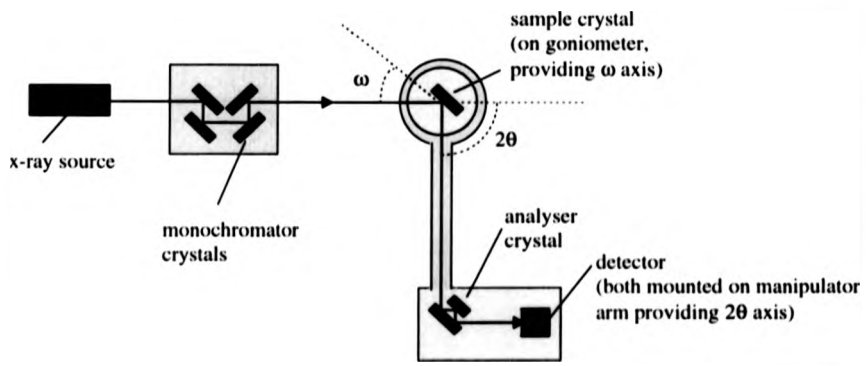

Figure 2.5 Schematic 8-bounce, 4-crystal diffractometer (after Fewster[4])

Here, the ω-circle controls the rotation of the sample (and hence the points of the reciprocal lattice) around the origin of reciprocal space, as in Figure 2.6.

Figure 2.6 also shows the effect of 2θ rotation on the detector. As the detector arm rotates, the detector itself is exposed to x-rays scattered into different directions by the crystal. These two rotations can be coupled, such that for any given angle-sweep of ω, 2θ sweeps twice the angle, and the product of such combined rotations is a relative motion of RLP and detector along the vector $\underline{r^*}$ - the scattering vector for the sample, geometrically perpendicular to the scattering planes themselves. In the high-resolution diffractometer described by Fewster[3,5], the angular precision of the ω and 2θ-circles is made high enough that the small arcs described in reciprocal space by rotations around them are approximately flat.

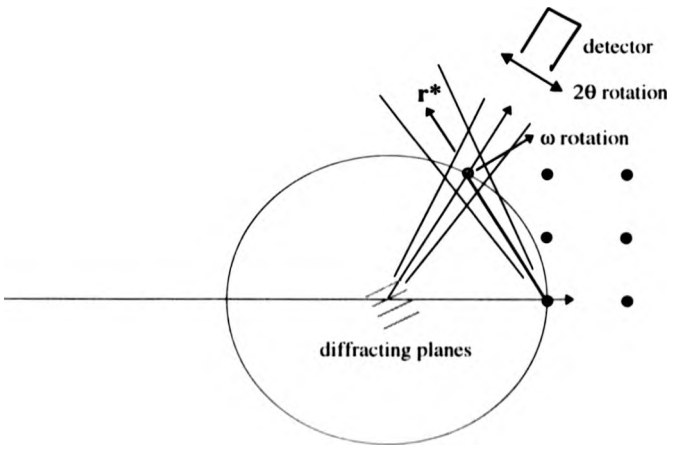

Figure 2.6 Diagram showing motion of detector and diffracting planes to give omega and 2-theta rotations, combined into $\underline{r^*}$.

By composing a series of ω/2θ scans, which move the detector across the RLP, with stepped rotations in ω (moving the RLP across the Ewald sphere) a "map" of the reciprocal space in the region of a single RLP can be created, as in Figure

2.7.

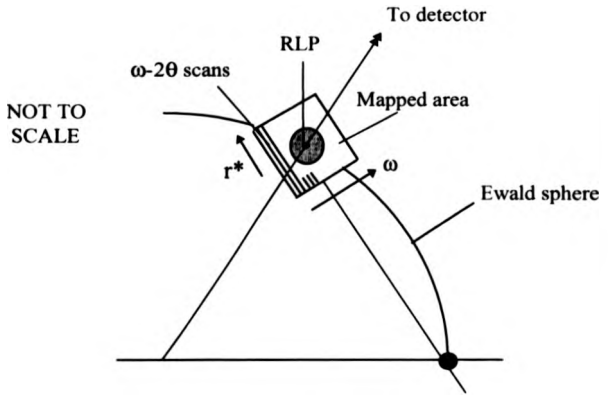

Figure 2.7 Diagram showing mapping of area in region of RLP by composing parallel r* scans offset by ω steps.

If an RLP is contained in this area, then all of its diffracted intensity can be recorded, and any of its structural features examined. There are, however, certain conditions which have to be met in order that this can be usefully achieved.

2.3.2.2 Beam conditioning.

To probe reciprocal space with high-resolution requires a probe design that is primarily smaller than the RLP it is examining. Since this probe is moved around in reciprocal space, it must also be of predictable shape, and introduce no artefacts which would obscure or confuse information from the RLP. These are the criteria described by Fewster[4], and they are achieved by firstly modifying the x-ray beam before it meets the sample, and then controlling the diffracted x-rays as they meet the detector.

A conventional sealed-tube x-ray source has a band of wavelengths in its output, centred around its characteristic wavelengths, which are superposed on a broad, white, Bremsstrahlung background. These emerge from the fine-focus tube as a divergent cone of radiation. Both these conditions have to be altered in order to avoid the Ewald-sphere modifications seen in Figures 2.3 and 2.4 - i.e. to achieve as near as possible an infinitely thin sphere. In the 8-bounce, 4-crystal high-

resolution diffractometer (8B4CHRXRD), the modifications to the incident x-ray beam are achieved by a 4-bounce Bartels monochromator, which sits at the emergence point of the x-rays from the tube. Two channel-cut Ge crystals (with the 110 plane as the face of the cut) are set as in Figure 2.8, modifying the x-rays before they proceed to the sample.

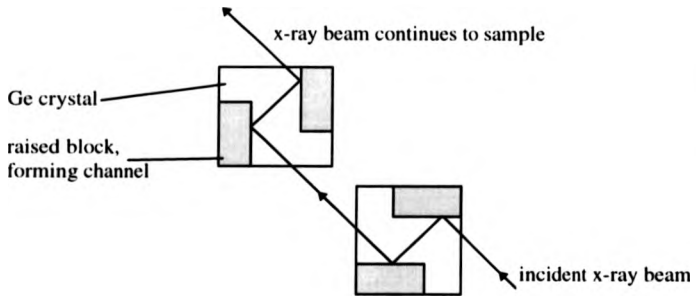

Figure 2.8 Representation of monochromator reflections for Bartels monochromator.

All bounces from the monochromator remove x-rays that fall outside the reflectivity profile for the Ge 220 reflection. By arranging the Ge crystals such that four bounces take place, both divergence and monochromaticity are minimised[6]. The primary reflection coarsely selects the wavelength range that fits under the reflectivity curve. This wavelength group passes onto the second bounce (set non-dispersively) and makes the beams of different wavelength more parallel by cutting the tails of the distribution. The third bounce is set dispersively, and disposes of beams arriving at large wavelength deviation, since the angular difference is doubled. It also serves to remove more intensity from the tails. The final bounce narrows the peak still more, and also returns the beam to its initial direction of propagation. By thus using the intrinsic-reflectivity profile of the Ge 220 reflection as a "filter", the beam that proceeds to the crystal has a virtually tail-less profile, and a tight wavelength spread. In fact the divergence in the diffraction plane is only 12" or less, and the wavelength spread (for Ge 220), $\Delta\lambda/\lambda$, is $6.9 * 10^{-5}$ - also around 12" equivalent[4]. The beam is also

almost completely polarised, in the vertical plane, after the four reflections each with an angle of reflection near 45°.

The monochromator thus produces an Ewald sphere which has near-ideal geometry. Though it must be remembered that if an RLP is moved through a probe with such a shape, any fine-structure the RLP has will be lost in convolution with the shape function of a coarse detector.

A typical 2-dimensional RLP image from such a diffractometer for an ideal, strongly scattering crystal, has two streak-like distortions in reciprocal space. The first is the crystal truncation rod (or surface-streak) and is caused by the sampling of a finite number of planes at the surface of the crystal. The second is an instrumental function, caused by the angular resolution of the detector, and is the analyser streak.

Thus for true high-resolution analysis of reciprocal space, beam conditioning must also be performed at the detector. If the detector is to have a fine angular acceptance, in order to discriminate the spatial distribution of x-rays coming from the sample, then another multiple-bounce technique can be used. For extremely high angular discrimination such as in the 8B4CHRD[4], a 3-bounce channel-cut Ge crystal is used, as in Figure 2.5, and carries the benefits of not reducing the intensity of the signal to the extent that a slit would. The triple-bounce causes an extremely fine angular selectivity, as in the monochromator.

2.3.3 The applications of High-Resolution X-Ray Diffraction.

The reciprocal space probe produced by the conditioning described above is extremely small in the plane of diffraction and has a definite characteristic in reciprocal-space, as can be seen in Figure 2.9 (ideally, width ≈ 5-6").

The applications of such a tightly-defined probe come from considering a non-ideal RLP for a particular reflection from a crystal. Assuming the RLP has a definite intensity distribution, by moving the reciprocal-space probe around inside the RLP, and detecting with high accuracy the intensity scattered from each point, a map of the intensity distribution can be generated. This sampling

can take the form of line-profiles, 2-dimensional "slices" through reciprocal space, or 3-dimensional volume maps[7] - all created by synchronised movements of the RLP and the probe.

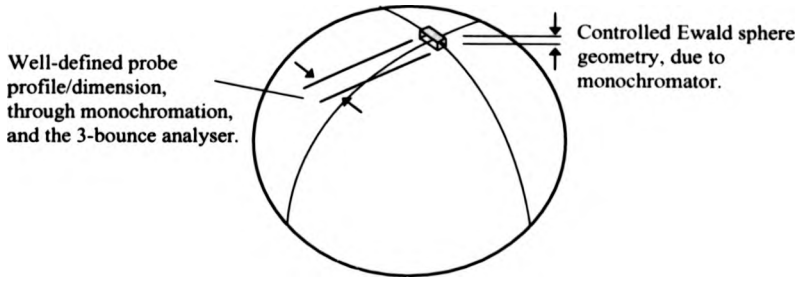

Figure 2.9 Representation of reciprocal-space probe geometry. Showing predictable thickness to Ewald-sphere, and a reliable shape (not to scale).

The diffractometer used at Warwick has the geometry of the 8B4CHRXRD described here. It is a Philips High-resolution diffractometer, with Cu long-fine-focus x-ray tube, Bartels 4-bounce monochromator and 3-bounce analyser: it also has an intensity of ~100k cps at the detector from a standard 004 reflection from pure silicon, and can discriminate features down to 6' in extent in angular-space.

Where such a diffractometer's value lies is in its superiority over diffractometers that produce only 1-dimensional curves, or diffractometers which can achieve only coarse angular discrimination in angular-space. The defect properties of a crystal (described in section 2.4) can result in lattice modification (local expansion or contraction, angular inconsistencies) which will influence the RLP profile in analysis of the defective region. With the high-resolution diffractometer, where the reciprocal-space probe is designed to be smaller than the interesting RLPs, the quality of the crystal can be examined by examining the RLPs and attributing the features they exhibit to particular defect-structures. This analysis has mainly been applied to semiconductor materials, particularly strained-layer heterostructures, since it permits non-destructive analysis of the quality of the layers in terms of defects and percentage strain[8]. By careful

analysis of the positions and intensities of peaks from such layers and substrates, physical information about the layers can be inferred which outline the success of a particular growth-experiment, for example. Where topography is combined with this technique, the relatively low defect-densities seen in semiconductors can permit excellent interpretation of the nature of, and quality-impact of, defects which can then be returned to the crystal growers to optimise subsequent growths.

2.4 Structural features of Crystals

The ideal crystal described in 2.1.1 assumes that in a crystal each atomic location is correctly filled at all times, that lattice planes are uninterrupted, and that at a surface the structure is simply discontinuous. In a real crystal, it is impossible for these criteria to be met, and in a certain sense it is undesirable for them to be, since the non-ideal quality extends the RLP and makes the detection of x-rays diffracted from a real crystal possible.

A real crystal possesses disruptions to the long-range order necessary for simple diffraction. Where a crystal possesses a defect on a microscopic scale, the perfection of the structure will be ideal up to the defect, but then discontinuous across it. The defect can be a point defect, or a defect taking the form of a line or plane in the crystal, and if defects are plentiful, it can be seen that macroscopic-scale imperfections in the crystal structure can exist.

2.4.1 Imperfect crystal features.

A highly non-ideal crystal structure can have a high density of defects, randomly located, such that the long-range order of the sample is severely disrupted. Or, one might find large, relatively perfect sections of crystal that are adjacent, but have a structural rotation with respect to each other. In the former case, the high-defect density might separate the crystal into small chunks, each having high-perfection, but randomly orientated at small angles to its neighbours. This is known as a mosaic structure. In the latter case, where twinning is said to have

occurred, the crystal is separated into large scale regions related by some symmetry operation, and the defect is the plane at which they meet. (Azaroff[9] gives a good account in Ch.10).

2.4.1.1 Point defects.

A real crystal structure will never have every atom in its allotted location. The interruption can be caused by a vacancy - a missing atom/ion - or a vicarious atom, an impurity. The impurity atom can be a foreign atom sitting in a site where it is not expected, or an atom at some stable point between other atoms - an interstitial. A Frenkel defect is formed where a missing atom or ion is found at such an interstitial location. Whichever is the case, nearby atoms are spatially shifted, with corresponding strain in their bonds. The overall result is a disruption to the regularity of the lattice, and hence any x-ray diffraction from planes in this region will perceive the difference in atomic spacing compared to the otherwise perfect local structure.

Furthermore we find that the point defect may have a local charge effect that violates the balance of charge within the rest of the structure. To tolerate this, the crystal can form a charge-compensation site, which is possibly the vacancy of one or more 'home' ions of the opposite charge (a Schottky defect), or in other cases the deliberate incorporation of a compensating ion: both restore the electrical neutrality of the crystal.

Singly, the effect of the point defect can be limited in extent, yet if numerous point defects congregate, then a line defect (a dislocation) or plane defect might be formed.

2.4.1.2 Line defects and plane defects.

A line defect is caused by a dislocation running through the structure, either as a line or a screw. In an edge dislocation, a lattice plane is found to stop in the bulk of a crystal, where the planes around it are continuous. As they continue past the end of the interrupted plane, they close together inducing local stress and disruption to the structural order. In a screw dislocation, a portion of the structure

is dragged along one line, and matches up with the bulk again one spacing along the lattice. A tracing of a particular plane around this defect finds that it spirals along the line of the defect. In either sense, the crystal immediately in the vicinity of the defect is distorted, as the structure attempts to close around the disruption to order - whilst at great distance from the defect, the crystal is ideally undistorted. A dislocation can have components that are partially line and edge at varying points along its path.

The Burgers vector is a way of characterising the nature of a dislocation. An imaginary closed path (Burgers circuit) circles the dislocation line, without crossing it, starting at a lattice point and returning there. When the defect is removed, the vector that defines the now missing part of the Burgers circuit is the Burgers vector, $\underline{b}$. For an edge dislocation, $\underline{b}$ is normal to the dislocation line, and for a screw dislocation $\underline{b}$ is parallel, and falls at some other angle for a mixed dislocation.

2.4.1.3 Planar defects

A planar defect is found where, if the crystal is imagined as being built of layers of different types in a repeating order, that order is violated, and hence in a direction that crosses the planar defect a disruption is perceived. Hence a planar defect is a stacking fault, and the crystal may or may not have a symmetry-related structure either side of the plane of the defect. If the stacking repeat is continued as expected after the defect, then the crystal structure proceeds as if the defect were not present. If the crystal one side of the plane has a particular symmetry relation to the structure the other side of the plane, then a twin has formed - and the two portions of the crystal are identical, but spatially related by some rotation or mirror function.

2.4.1.4 Volume defects

A volume defect is found where over a region within the crystal there is catastrophic disruption to the structure. A void in the crystal is such a defect, or the void can be filled with some material alien to the structure. This latter case is

an inclusion, where material is contained during the growth of the crystal or is precipitated into a void. The crystal structure around a volume defect depends on the size of the defect and its nature, for the structural strain it induces may provide the source for both line and plane defects in its vicinity.

2.4.2 Structural implications of defects

Singly, all the defects defined above violate structural order within a region around the defect itself, whilst at some large distance away (many unit cells) the structure is unaffected by the defect. The impact of a single defect also depends on the crystal-type, and its end-use implications vary accordingly. For example, in a highly-perfect semiconductor crystal, relatively low defect densities may render the crystal useless for device purposes: the same defect density might be tolerated in an application that uses a different crystal for its optical properties (see[10] Ch.1 and 2).

Grouping of defects can also be seen as forming the regions that isolate individual mosaic blocks from each other – forming the small angle grain boundaries that separate regions of otherwise highly-perfect crystal.

2.5 X-ray topography.

2.5.1 Topographic methods

In an x-ray topography experiment, the diffracted intensity from an extended region of the sample single-crystal is captured as an image - usually on photographic film. Spatial variation in scattering efficiency in the exposed region of crystal thus appears as contrast variations in the topographic image, such variations being caused often by the defect structure of the crystal, since the scattering efficiency varies with the local structure.

Depending on absorption in the sample, topography can either be performed in transmission, where thin or low-absorbing samples are used, or reflection, where thicker or highly-absorbing samples are used.

In the transmission Lang method, a sample is set at the Bragg angle for the

chosen reflection relative to a collimated x-ray beam (Figure 2.10a). The direct beam is blocked by a screen, and the image of the transmitted x-rays is captured on a photographic plate.

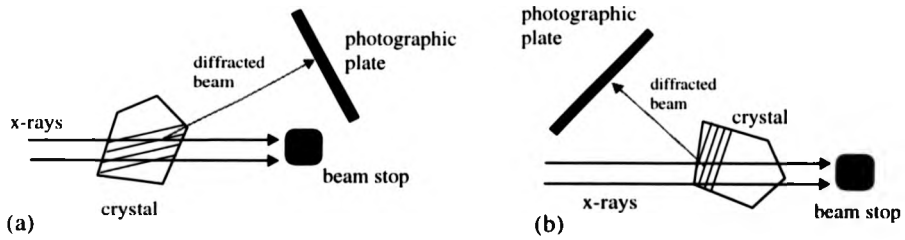

Figure 2.10 Lang topography schematic diagrams. (a) transmission geometry case (b) reflection geometry case.

When the crystal is immobile, and the beam is narrowed in the dimension perpendicular to the scattering planes, this method is also known as section topography, since the x-rays penetrate as a plane and hence a single 'slice' of the crystal is examined at a time. In the back-reflection method, the crystal is again set at the Bragg angle, but the photographic plate is positioned to capture x-rays in back-reflection from the sample (Figure 2.10b), and hence this method does not perceive volume effects in the same way as section topography since only the structure within the x-ray penetration depth contributes to diffraction.

The Philips diffractometer shown in Figure 2.5 can also be used to perform reflection topography, exploiting the same diffraction-space probe designed for reciprocal-space mapping to extend understanding of the crystal under investigation. Where a photographic emulsion is placed before the analyser, the same back-reflection results can be achieved as above. But where a photographic emulsion is placed after the analyser crystal, i.e. a 4-crystal setup, the x-rays gathered can demonstrate the distribution of scattered intensity from any particular region of the probed area, for any particular reflection. The probe's small size and high-resolution angular discrimination allows real-space

interpretation of the contrast seen in the topographs, although a degree of geometrical broadening occurs. The technique has been used in semiconductor studies to interpret the defect-sourced diffuse scattering near to Bragg peaks[11], allowing the identification of specific defects. The one limitation for this particular technique is that whilst the 8-bounces allow excellent angular discrimination for the topography, the relative intensity of the reflection must be high enough to allow a high enough photon throughput to the emulsion itself.

Both methods have specific uses - for example section topography is ideal for determining volume flaws in optical or gem crystals. Back reflection topography is ideal where manipulation of the sample is difficult or undesired - it is the method used for *in situ* examination of the defects in the aluminium skin of aircraft fuselage components, for example. It has applications for crystals which are difficult to obtain in large volume or are otherwise difficult to prepare into sufficiently thin samples to account for absorption, or limited photon-flux is available, as in the laboratory.

2.5.2 Topograph contrast mechanisms

The mechanism for defect contrast in a topograph is complex, and can be described in terms of three main types: scattering contrast, orientation contrast and dynamic contrast (see Giacovazzo[12], Chapter 9)

The region around a defect is imperfect, and is revealed as scattering-efficiency contrast in a topograph, simply because this distorted structure sits in a non-ideal Bragg configuration (in monochromatic radiation). Thus where the perfect region around a defect presents a smooth contrast across the image, the defect itself will be visible as either dark or light contrast relative to this. If the defect scatters more, then it will be dark in the diffracted beam - a kinematic scattering effect.

From a dislocation, contrast in a topograph is also sourced in the propagation of x-rays through the surrounding distorted crystal. A direct image of the dislocation is formed, since the lattice parameters in the strained structure are no

longer suitable at the chosen Bragg angle - a scattering contrast effect. If there is no component of the strain field parallel to the diffraction vector, then topography will not see the dislocation. In terms of the Burgers vector, conditions for viewing are:

$$\underline{b} \cdot \underline{g} \neq 0 \quad \text{and} \quad l \wedge \underline{b} \cdot \underline{g} \neq 0 \tag{2.5}$$

where $\underline{b}$ is the Burgers vector, $\underline{g}$ is the diffraction vector of the Bragg planes and l is the line vector corresponding to the dislocation.

In a highly-perfect crystal the incident and diffracted wave-fields interfere as they progress through the crystal. The standing wave formed as a result takes the shape of a triangle in cross-section, and is known as the Boorman fan. Where a defect is present in the crystal in the region of the Boorman fan, it is revealed directly as a dynamic image - a white shadow in the fan. The ongoing diffracted waves that diffract at the dislocation also interfere with this wave-field, and generate their own interference fringes (Pendellosung fringes) in the diffracted x-ray beam.

If a white-beam experiment is conducted to probe a region of mis-orientated perfect structure within a crystal (i.e. a mosaic block), redirection of the diffracted beams results in a shifted image of the block in the topograph if the angular deviation is enough, or the sample-film distance is sufficiently large. The block can then be individually imaged by using collimated single-λ radiation and looking for this orientation contrast. Using a double-crystal technique, where an analyser selects the angular acceptance range of the topograph, the particular mis-alignment of the blocks can be discovered. Separate rotations of ω and 2θ then determine if the contrast is due to orientation, or lattice distortions - making this a very powerful technique for examining defects.

2.5.3 Anomalous scattering

The 11 Laue classes of crystal symmetry are formed by considering that the distribution of x-ray reflection intensities has a centre of symmetry. This is

known as Friedel's Law. Expressed in terms of reflection structure factors this is:

$$|F_{hkl}|^2 = |F_{\bar{h}\bar{k}\bar{l}}|^2 \qquad (2.6)$$

Scattering from all crystals was initially assumed to obey Friedel's law, such that a centre of symmetry was seen in x-ray diffraction patterns at all times. The phenomenon of anomalous scattering, coupled with an improved model of the mechanisms of scattering and improved x-ray detection provided the solution to this problem. James[13] provided one of the first works to address this effect, and it remains a principal reference alongside more recent discussions in the ITFC[3]. Friedel's law is now known to hold only for cases where the structure is centrosymmetric, or there is only one scattering species in a non-centrosymmetric crystal, or there is no anomalous scattering.

The source of anomalous scattering comes from modifying the scattering as found for a classical electron to include the effects of absorption of the radiation. This introduces a phase-shift other than the classically-derived, π, to the scattering and leads to the corrected form factor:

$$f_j = f_{oj} + \Delta f'_j + i\Delta f''_j \qquad (2.7)$$

where f_{oj} is the Fourier transform of the electronic distribution, and the remaining two factors are real and imaginary segments of the dispersion correction for the j^{th} atom. The original model only accounted for the simple-harmonic motion of electrons classically bound to the nucleus, ignoring the resonance that can occur when an electon is excited by the incident x-rays. This case is anomalous scattering, and when the structure-factor calculations incorporate this scattering factor with dispersion corrections:

$$F_{hkl} = \sum_j (f'j + if''j) \exp(2\pi i[hx_j + ky_j + lz_j]) \qquad (2.8a)$$

$$F_{\bar{h}\bar{k}\bar{l}} = \sum_j (f'j + if''j) \exp(-2\pi i[hx_j + ky_j + lz_j]) \qquad (2.8b)$$

it leads to F_{hkl} and $F_{\bar{h}\bar{k}\bar{l}}$ no-longer being complex conjugates, and equation

(2.6) is no-longer valid. Schematically, this is represented in Figure 2.11

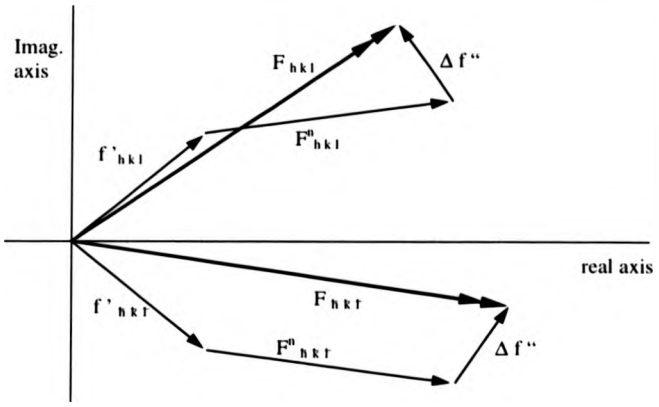

Figure 2.11 Relation between F_{hkl} and, $F_{\bar{h}\bar{k}\bar{l}}$ when anomalous dispersion is present. F_{hkl} and $F_{\bar{h}\bar{k}\bar{l}}$ are the structure factors for normally-scattering atoms (F^n_{hkl} and $F^n_{\bar{h}\bar{k}\bar{l}}$), and f' and Δf' for the anomalous scatterers

The contribution of anomalous scattering should, by differential structure-factors, make 180° polar domains visible by topographic methods. This has, for example, been performed on artificially induced domains in $BaTiO_3$[14], where Lang topography revealed contrast differentials across the modified crystal.

2.5.4 The applications of topography

What topography always perceives is the changes in scattering across an extended part of the crystal, sourced in its defect or mosaic/domain structure. Amongst many uses, Lang topography is particularly useful in selection of single-domain crystals for seed-growth experiments, since the local strain around a growth-sector boundary is imaged. For other work, such as examining semiconductor wafers, double-crystal topography is highly efficient at imaging the dislocations in the otherwise highly perfect structure, since the topographic image can contain shadows and interference fringes that relate to the location and

type of defect found in the material and hence identify faults in the growth processes.

Synchrotron radiation, due to its high brightness, is ideally suited to topographic experiments, since samples do not have to be prepared as critically thin for absorption. The large area available in a synchrotron can also permit sampling of large areas of crystal at once, which reduces both the time necessary for experimentation, and may also be important where too much sample preparation may induce artefacts into the crystals themselves. The high collimation of the beam also provides useful, low divergence, conditions excellent for determination of misorientations, and not usually achievable in the laboratory. In particular, the x-rays can be selected from a polarised source, allowing still more experiments, and the white-beam characteristic allows either white-beam Laue-type experiments, or selection of single wavelengths.

2.6 References

[1] "Crystal structures: A Working Approach" H.D. Megaw, publ. W.B.Saunders Co., London (1973)

[2] "Space Groups for Solid-State Scientists" G. Burns and A.M.Glazer, Academic Press, London (1978)

[3] International Tables for Crystallography, publ. for the International Union of Crystallography by Kluwer Academic Publishers, London 1995.

[4] P. F. Fewster. *Appl. Phys. A* **58** (1994) 121

[5] D.J. Watkin, J.R. Carruthers, P.W. Betteridge. CRYSTALS User Guide. Chemical Crystallography Dept., University of Oxford, England

[6] P.F. Fewster. *J. Appl. Cryst.* **22** (1989) 64

[7] P.F. Fewster, N.L.Andrew. *J. Phys. D:Appl. Phys.* **28**, (1995) 97

[8] P.F. Fewster. *Appl. Surf. Sci.* **50,** (1991) 9

[9] "Elements of X-Ray Crystallography" L.V. Azaroff, McGraw-Hill Co., London (1968)

[10] "Characterisation of Crystal Growth Defects by X-Ray Methods" Ed. B.K.Tanner and D.K.Bowen, Plenum, London, (1980)

[11] P.F. Fewster. *J. Appl. Cryst.* **24** (1991) 178

[12] "Fundamentals of Crystallography" Ed. C.Giacovazzo, publ. for IUCr by Oxford University Press, (1995)

[13] "The Optical Principles of the Diffraction of X-Rays" R.W. James, Bell and Sons Ltd., (1965)

[14] N. Niiekii, M. Hasegawa. *J. Phys. Soc. Japan.* **16** (1964) 550

Chapter 3

High Resolution X-ray Diffraction

3.1 Introduction

The use of the high-resolution x-ray diffractometer (see chapter 2) allows access to data on the structure of a crystal sample that would otherwise be difficult to obtain. In particular, details of the defect or mosaic structure of a sample can give important clues to its perfection, which can then be related to its physical character. This information could, in the case of KTP and its family, give important information on the optical performance of the samples, since their non-linear performance is reduced by the differential scattering caused by the presence of defects, such as domains, dislocations, or large-angle mosaicity.

3.2 Experimental details

3.2.1 Features of the High-resolution X-ray diffractometer

The Philips Materials Research Diffractometer (MRD) is a high-resolution x-ray diffractometer, with an 8-bounce 3-crystal set-up, driven by a dedicated PC with associated proprietary software. A Bartels 4-bounce monochromator (Ge-220) conditions the x-rays produced by a Cu-Kα long-fine-focus conventional x-ray source. The x-rays scattered by the sample crystal are collected by a proportional gas counter, either entering directly via a slit ("receiving slit"), or via a 3-bounce analyser system. This analyser uses three Ge-220 bounces to determine the angular-resolution of the high-resolution mode of the diffractometer, giving the detector a window approximately 6 arc-seconds wide in the high-resolution direction, and having a virtually tail-less profile.

Sample and Ewald sphere manipulation is achieved by an open Eulerian cradle, with ω, 2θ circles and ϕ and χ axes: an x-y motor translation stage designed for

semiconductor wafers can be used to select the area of the sample exposed to x-rays (see Figure 3.1). Samples are generally fixed to this stage using adhesive tape if the sample is thin or high-temperature wax if the sample is significantly thick. The use of adhesive tape had been previously found to provide adequate control of the sample fixing, and to induce minimal strain across the sample surface.

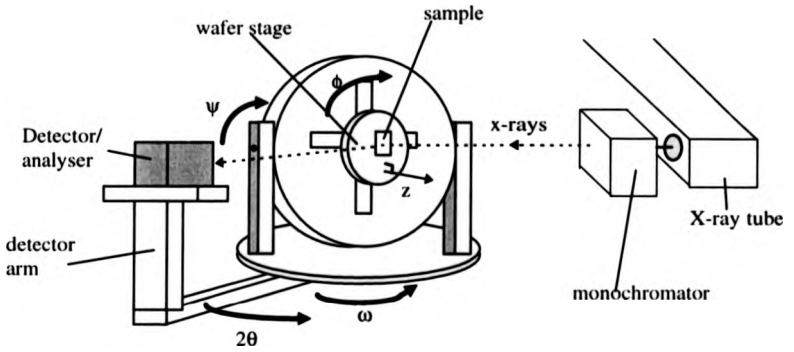

Figure 3.1 Schematic representation of the Philips MRD

The diffractometer is zero-aligned by setting the diffractometers' circles in their nominal zero positions, and then arranging a custom knife-edge to halve the straight-through beam from the monochromator: this is itself aligned using a standard silicon sample. The absolute angular location is then measured relative to these zeros by angle-encoders on the manipulation circles, sensitive to 0.00025° on the ω circle and 0.0005° on the 2θ circle, with lesser resolution (not optically-encoded) on the other axes (such as 0.1° on the ϕ circle). The repositioning error is of the order of a few steps on each circle, and back-lash errors are minimised by approaching positions from the same direction.

3.2.2 A typical experimental run

A typical experimental run will follow this series of processes:

1) The detector arm, ω-stage and other axes are driven to their zero-stops. The

sample is fixed to the wafer-stage, positioned approximately at the centre of the goniometer, but translated in z away from the x-ray beam. The surface to be exposed is then brought into the centre of the diffraction plane and ω-circle by using it to halve the direct-beam intensity as measured by the detector. This ensures the surface of the sample is centred on the diffraction axis, to avoid the geometrical effects which can cause mis-interpretation of the diffracted intensity such as apparent 2θ variations caused by the surface of the sample being away from the centre of the straight-through x-ray beam.

2)Using a set of pre-calculated angular parameters, or using the angles calculated by the MRD from the materials' lattice parameters, the diffractometer is driven to the approximate angles such that the diffraction condition is met. This is generally achievable by only two or three rotations, first bringing the reciprocal space node onto the diffraction plane, and then onto the Ewald sphere. The limitations of the geometry of the diffractometer, and the angular range of the various circles place limits on the choice of reflection available from a particular sample.

3) Using the open slit configuration the intensity at the detector is maximised as the RLP is placed on the Ewald sphere. This configuration allows an angular acceptance of 2° in the 2θ direction, which is broad enough to permit approximate first alignments, which can then be refined. Positioning is performed by small rotations around ϕ and ψ then re-optimising the ω axis, since the peak generally possesses a three-dimensional distortion. Geometrical effects, for example, mean that the peak is smeared into a curve in the ψ-ω plane, and the particular alignment may mean the central rocking curve for the set-up slices the curve, giving a ψ-rocking curve with two peaks[1]. In this case the goniometer is centred between the two peaks, and then re-optimised in the ω direction.

4) At this point, a rocking-curve is generally taken. These are the data generated when the intensity received at the detector is plotted versus the angle driven by the diffractometer as it translates both ω and 2θ (i.e. a translation in the direction

of vector $\underline{r}^*$, see chapter 2). A similar data set is taken as the diffractometer sweeps out an arc in ω. These two scans give a sense of the general character and size of the RLP in reciprocal space, and allow a map to be planned.

5) The diffractometer is changed into high-resolution mode, by moving the analyser into place between the sample and the detector aperture. This reduces the intensity received at the detector by approximately a third, but also improves the selectivity of the 2θ axis to 6'. This necessitates further optimisations of ψ and then ω and 2θ (ϕ has a particularly coarse angular resolution of approximately 0.1°, and is hence generally left at the previously determined angles) in order to centre the diffractometer on the diffraction peak.

6) A reciprocal-space map is generated, using angular dimensions determined from section 5. The diffractometer sweeps out a series of $\omega/2\theta$ scans separated by small steps in ω, a process which generally takes a number of hours. The choice of angular step takes into account, amongst other things, the dwell time of the reciprocal-space probe at each point of the map. This parameter will determine the quality of the map, for it discriminates the signal/noise ratio. For the purposes of most scans, from a moderately intense KTP reflection (say, above 2000 cps at the peak in high-resolution mode) a dwell time of over 1 second per pixel has been found to provide sufficiently accurate data, with good discrimination of the 5cps background level.

7) Observation of the map can decide if the details of the particular reflection warrant a high-resolution topograph. If so, then the diffractometer is repositioned at the relevant angular co-ordinates that either correspond to the interesting feature in the reciprocal-space map, or reveal extra information about it (such as strain influences). When positioned, a slide containing the x-ray film is inserted between the analyser exit-aperture and the detector. The Ilford L4 25μm film used requires a photon density of greater than 10^9 photons in the exposed area to reveal significant contrast. Exposure times are typically between 1 and 10 hours

though positional drifts prevent longer exposures.

The x-ray film can be placed before the analyser, for a low-resolution topograph, and then the effect is as the back-reflection Lang topograph described in Chapter 2.

3.2.3 Example reciprocal-space maps

The diffractometer is supplied with a standard silicon wafer (with the 111 planes parallel to its surface), though it is possible to use a piece of silicon fixed to the wafer-stage in the manner used for thin KTP samples. In either case, a reciprocal space map of the 111 reflection from silicon provides a typical data set, which, taking advantage of the high purity and perfection available from silicon crystals, serves to exhibit the diffractometer characteristics.

An example map from such a reflection is seen in Figure 3.2, in reciprocal-space co-ordinates. The sample is a lower-grade Si wafer, damaged by cold-soaking in liquid nitrogen to demonstrate defect-sensitivity of the diffractometer, and bringing the reciprocal-lattice point closer to that generally seen for pure KTP.

Notably, the peak is of a high intensity, approaching one tenth of the direct beam intensity from a typical 40kV 30mA setting for the x-ray tube. This is due to the high reflectivity of silicon, and contrasts enormously with a typical background count for the diffractometer of below 5 cps. With a high enough dwell-time per pixel of the map, the counting statistics of the data set can allow discrimination of this 5 cps contour in the reciprocal-space maps, making the diffractometer suitable for examining either small, or low-reflectivity samples. For an undamaged Si crystal, intensity at the RLP can be as high as one third of the direct-beam radiation.

The large central peak of the map, the reciprocal space node itself, is visibly symmetrical, with one greatly-extended axis (vertically) which is characteristic of the surface-termination problem of diffraction experiments - it is the crystal truncation rod. The smaller, diagonal, streak is present as the tails of the intrinsic beam profile of the diffractometer (caused by the diffraction effects in the

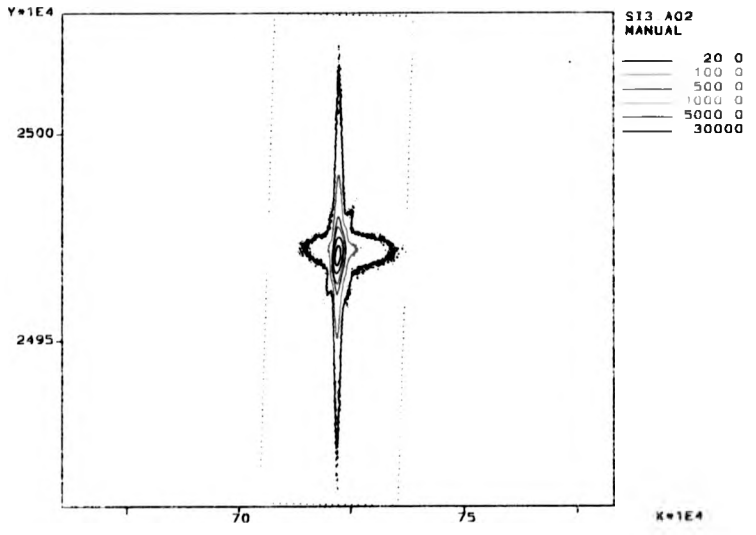

Figure 3.2 Reciprocal-space map (in reciprocal-space coordinates) for the 111 reflection from Si.

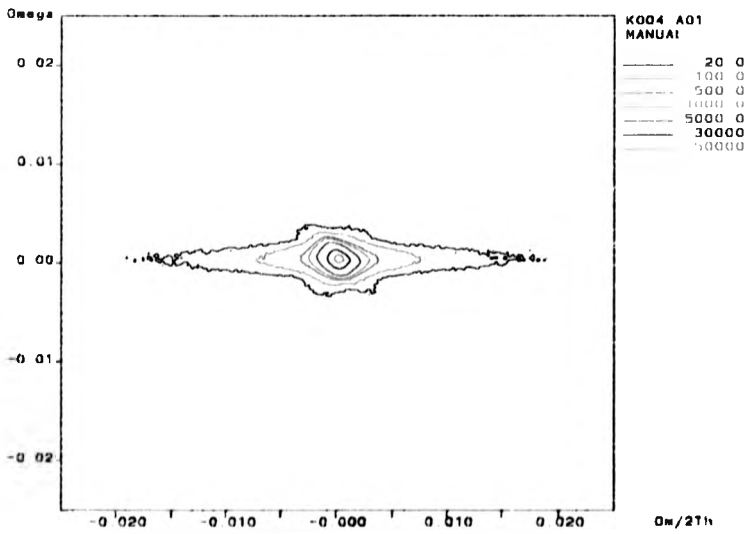

Figure 3.3 Reciprocal-space map (angular coordinates) for the 004 reflection from pure KTP.

analyser) pass across the Ewald sphere during the experiment, and a slight corresponding stretch in the RLP can also be seen. If the analyser had a lower selectivity (as in the case of a two-bounce Ge analyser) then the streak would be more significant, distorting the data from the RLP more. A similar streak would be introduced by the monochromator if the beam conditioning by the monochromator were not as good, such as in a monochromator with fewer bounces. Due to the low intensity of these features, they are generally only seen in reflections with high structure-factors, and with the three-bounce Ge analyser, the analyser streak is much diminished. The lateral streak is extended diffuse scattering, characteristic of the lattice-damage induced by thermally-shocking the surface layers.

A similar map for the 004 reflection from a high-quality sample of pure KTP is seen in Figure 3.3 in angular co-ordinates (the apparent rotation of the reciprocal-space streaks is due the geometrical translation of the two map-types). Generally, the same features are present, with the main differences being the lower peak intensity and different surface streak proportions, determined by the different structure-factors, absorption depths and surface perfections of the two materials. This map, when compared to the same reflection from different KTP samples can be used as a fast comparison of the relative qualities of the materials due to its high intensity and regular profile. For example, the higher perfection of the Si sample leads to potential scattering in the monochromator streak (just visible as the vestiges of a tail crossing the RLP in the opposite sense to the analyser streak in figure 3.2). The undamaged surface of the KTP (compared to the deliberately damaged Si) causes a more symmetrical peak, not showing extended diffuse scattering. Where significant defect structures are present in the irradiated portion of the samples, the deviation from these ideal peak-profiles would reveal their existence. Lattice tilt defects are seen as distortions in the ω or surface-equivalent directions, and *d*-spacing defects are seen as distortions in the ω-2θ direction (and its equivalent in reciprocal-space co-ordinates).

3.2.4 Sample preparation

The requirement for accurate reflection from a sample surface for the MRD is a flatness to a fraction of the x-ray wavelength. Where surfaces do not possess this flatness, a high-resolution study will not reveal any additional information about the sample quality itself, since diffraction from the crystal bulk will be confused by surface, or preparation, artefacts. Similarly, a bent or strained sample will not provide a 'true' set of diffraction data due to the distortion of the lattice planes in the surface of the sample, and the data from the x-ray experiment would simply quantify this physical distortion.

For KTP-family materials, this flatness is achievable by careful polishing, and etching can be performed as a final surface preparation. Samples are cut as thin plates for ease of mounting (aligned by Laue diffraction), from the bulk crystal by a diamond saw. This leaves highly damaged surfaces, so a series of polishing processes is followed. An automated polisher applies the first set of polishes, using diamond-loaded pads of grades down to a few μm. This coarse polishing removes the larger surface scratches and distortions, but leaves the surface still damaged and strained. Hand polishing is generally used to apply the final 1 μm to 0.3 μm finishes that remove this damage, and leave the surface free from strain.

For larger samples, the same procedure is followed, though the sample may not take the form of a thin plate, and repeated hand-polishing is often the simplest way to achieve an acceptable surface finish.

In general, following such a regime has been found to produce useful samples with a surface flatness within acceptable tolerances, such that little evidence of surface strain is found during the x-ray experiments. The application of strain is further minimised by the use of adhesive tape to fix thin samples to the x-y wafer-stage of the diffractometer. Scotch Magic tape is used, since this is produced without residual strain. Where thicker samples are waxed to the stage, it is assumed that the strain induced on one facet by the cooled wax is dissipated

in the bulk of the crystal, leaving the exposed surface free of strain.

Handling of the samples is performed with some care to avoid introducing artefacts, and surfaces that are to be x-rayed are cleaned with methanol or iso-propanol to remove fingerprints and other contaminating materials.

3.3 Results

3.3.1 Nb:KTP

Nb:KTP has been the subject of some investigation[2,3]. It has been found to possess the extended birefringence desired technologically, and is capable of being grown in various Nb concentrations by the flux-growth process. A structural analysis has been performed[3], and the material performs promisingly as an SHG crystal. A high-resolution study had not been performed, and the need for such an investigation was implied by the highly distorted surface seen on some of the bulk crystals and the radically different flat growth-morphology seen for some growth experiments. Such a frustrated growth process was thought to be responsible for a significant defect structure in the crystal itself.

3.3.1.1 Sample preparation

The sample of Nb:KTP (10% Nb) was cut from the tip of the as-grown crystal (see Figure 3.4). The as-grown crystal was produced by flux growth, including a 10% direct mass substitution for Ti in the flux components, and the final crystal possessed a slight yellow cast, and had limited growth in the a direction (compared to favourable growth in the other directions) of only approximately 7mm, and possessed a few small cracks near the seed.

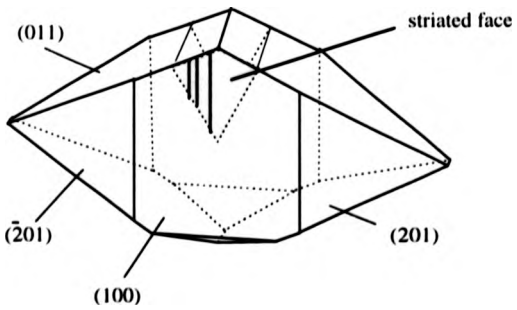

Figure 3.4 Location of Nb:KTP sample in the bulk crystal.

This roughly triangular sample had an a surface which was heavily striated, as did the {201} faces of the bulk crystal. There was seen to be a varying density of striations across the surface, though the larger scale striations were up to 400μm in depth, and smaller striae were determined at micron-size by optical microscopy. The striations ran parallel to the b-axis, such that they stacked along the c-direction. They were assumed to be facets of the familiar {201} growth-surfaces, bordered by edges parallel to [010], but were too small to be individually x-rayed. An investigation using an atomic-force microscope to analyse the surface was made difficult by the mixing of larger (i.e. fractions of a mm) striations with smaller (micron-size) ones. Establishing the angles of the striae facets was not possible, though the investigation did confirm the varied size of the striae and the random nature of their distribution.

For preparation for high-resolution x-ray analysis, these surface striae were removed by diamond-saw cutting a shallow (0.5mm) layer from one of the a-faces (Laue aligned) and then coarse-polishing approximately 0.1mm of the sample away, using 1200-grade alumina paper. This left the surface scratched and strained, but free of coarse steps. The strain and scratches were removed by successive polishings at finer grades until 0.3μm, leaving a surface flat enough for high-resolution analysis. The sample was only prepared on this face, to retain the striations for information. Thus the sample was wax-mounted onto the sample stage of the MRD, its thickness dissipating the effects of stress induced by the wax cooling, such that the examined face was assumed to be flat.

3.3.1.2 Results and discussion

Initial scans using the 4 0 0 reflection, amongst other symmetric reflections, with the b, c axes randomly orientated with respect to the diffraction plane, produced symmetrical rocking curves, with a marginally higher tail density than seen in other KTP samples, and comparable peak intensity (around 10^4 cps). For the 400 reflection, rocking curve FWHM's were in the region of 0.002°, which is very close to comparable FWHMs for KTP (≈0.0027°). An intensity two or three

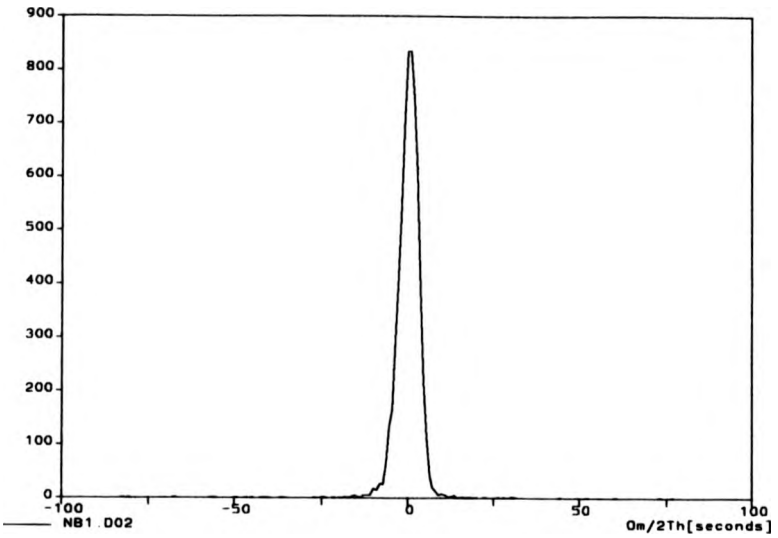

Figure 3..5(a) ω-2θ scan for 400 reflection from Nb:KTP, noting the symmetry of the peak.

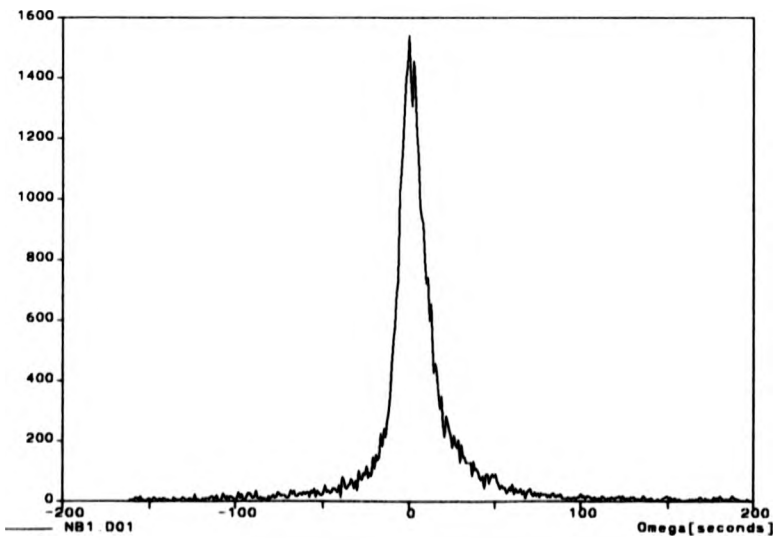

Figure 3.5(b) ω-scan for the 400 reflection from Nb:KTP, noting the shoulder on the high-ω side of the peak.

times that of background (taken as 5cps) was found in the tails up to 0.01° remote from the central peak, which is more intense than the typical KTP case. However, a realignment of the crystal, by an arbitrary ϕ angle i.e. such that [010] and [001] were at a different unknown angle relative to the diffraction axis, displayed a different effect. Example rocking curves for one particular setting (with the b-axis of the sample close to the vertical axis of the diffractometer) are shown in Figures 3.5(a) and (b). The curves are clearly symmetrical in the $\omega/2\theta$ case, and hence suggest a crystal with a high degree of lattice perfection. The ω rocking curve, in a receiving-slit mode, showed distinct broadening, and the corresponding high-resolution map of the RLP showed a marked diffuse-scattering, and distortion of the RLP in the ω direction (see Figure 3.6) (not associated with the surface streak).

This effect was investigated by orienting the crystal such that the b and then c axes were in the plane of diffraction, and performing new 400 rocking curves. By rotating the sample in ϕ close to and then far from the position found for b, and re-optimising the diffractometer, it was determined that the peak distortion effects were related to the angle from the b-axis. The rocking curves for the alignment with b parallel to the high-resolution direction showed no interest, and maps confirmed that diffraction appeared as normal. A typical 400 reciprocal-space map of the sample when the c-axis was in the plane of diffraction is seen in Figure 3.7. The notable features are the distorted diffuse scattering and slight extension of the peak in the direction corresponding to angular tilt. This suggests that the sample area contained a mosaic structure, with an angular mis-alignment between each block which is compressed into this one-dimensional distortion by the nature of the map. A slight *d*-spacing-equivalent displacement is seen in this streak, complementing the slight $2\text{-}\theta$ stretch of the peak in Figure 3.6.

A series of scans was performed where the sample was translated in the x and y directions such that a slightly different surface region was irradiated each time. The possibility that the features described above were related to a single defect or

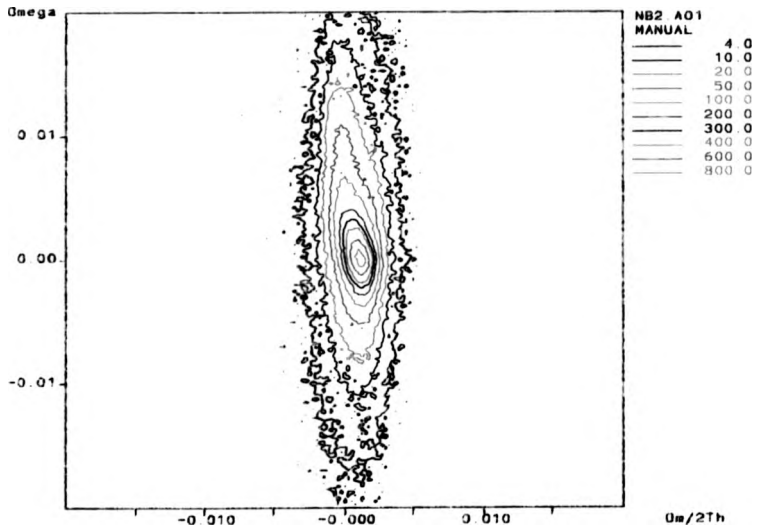

Figure 3.6 Reciprocal-space map for 400 reflection from Nb:KTP, showing distortion of the peak in the ω-direction.

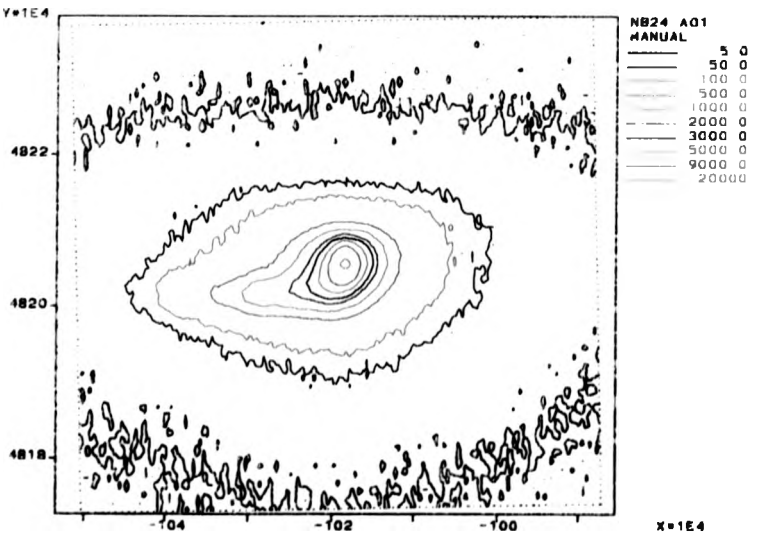

Figure 3.7 Reciprocal-space map of 400 reflection, with [001] in plane of diffraction.

region was removed, when similar peak-distortions were seen from different regions of the sample as the sample was translated. For the different 400 reflections, the peak splitting effect was inhomogeneous across the sample area, with some regions exhibiting the effect to different extents, and others presenting undistorted maps.

The 800 reflection was observed, due to its high structure-factor leading to large count rates at the detector. The higher Bragg angle means that this reflection is also more bulk-sensitive than the previous scans. By translation and preservation of the diffraction condition, the same inhomogeneous peak distortion was seen across various regions of the sample. No evidence was found of *d*-spacing variation in any reciprocal-space maps. All rocking curves were close to the 0.0035° FWHM seen for pure KTP. Perhaps the most striking effect was the significantly higher diffraction present in the tails of the rocking curves, extending for many FWHMs to either side of the centre at a level of several times background. Figure 3.8 shows an example reciprocal space map, showing a clear extension of the diffuse scattering in the omega direction.

The asymmetric reflection 810 was studied, primarily because of its proximity to 800 meaning a similar region of sample was irradiated. It was chosen for its comparably high brightness, and the fact that the b-axis crossed the high-resolution direction of the diffractometer in this configuration. The crystal was first aligned by finding reflections such as 402 and 410, then driven to the angle for 810. This reflection is found at a similarly steep incidence angle to 800, so that surface effects can be better discounted in diffraction features.

The reciprocal-space map in figure 3.9 shows a gross RLP distortion for this reflection. The RLP is smeared out along the ω-direction, and has two satellite peaks, approximately 0.01° away on the ω axis, of significant intensity. The angular displacement in the ω-2θ direction is small, and not due to poorly-optimised geometry (as several ψ-stepped scans confirmed). A study of the 207 reflection at this position, whilst involving a slight ϕ and ψ-adjustment, also

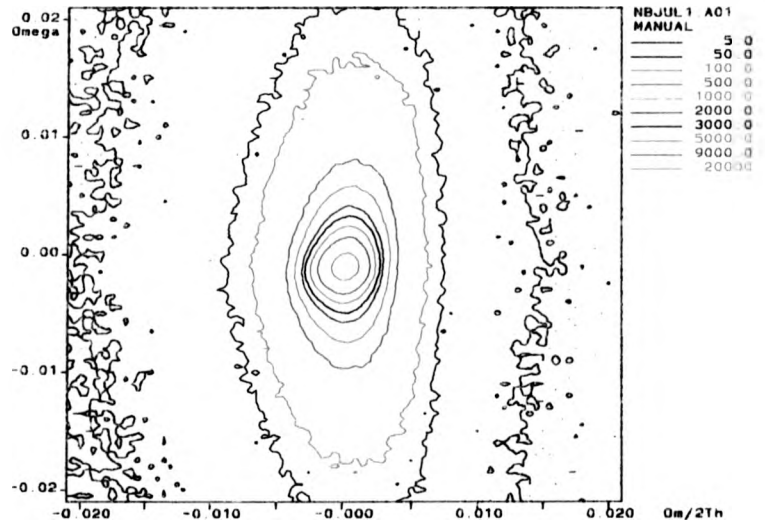

Figure 3.8 Reciprocal-space map for 800 reflection from Nb:KTP, showing distortion of the peak in the ω-direction.

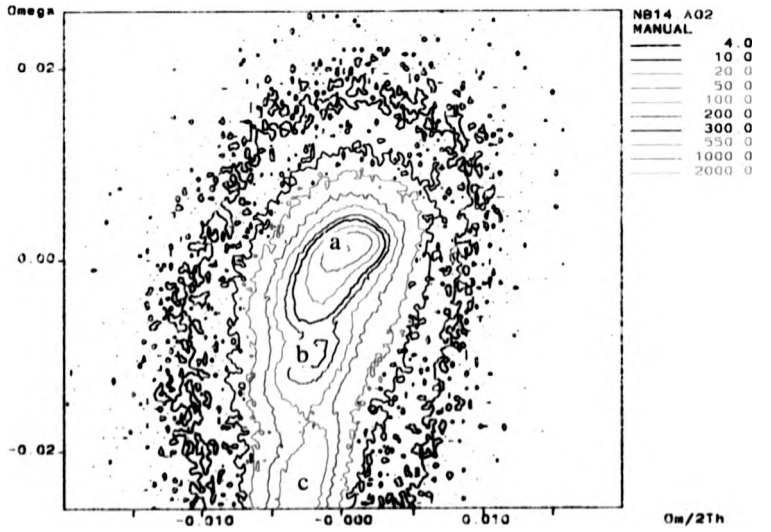

Figure 3.9 Reciprocal-space map of 810 reflection, showing a gross distortion of the peak in the ω-direction into satellites.

showed a *d*-spacing alteration, though the satellite peak was seen only as a shoulder on the main peak (the 207 asymmetry gives a slight compression of the area irradiated due to the reflection geometry). Tracking of the x-rayed area by only 0.1mm in x or y near this position revealed no other similar effects, suggesting that the effect was confined to a very small region, most likely a single growth block with slightly modified structure.

Triple-crystal topographs were taken at the points shown in Figure 3.9. These can be seen in Figure 3.10. The presence of non-uniformity in the topographs is clear, with topograph (a) showing strong diffraction across most of the peak with several areas of missing intensity. Some of the missing intensity from the right of topograph (a) is recovered in the second topograph (b), which is found by an ω-rotation and a small 2θ rotation. Faint, fine diagonal lines are also seen in this

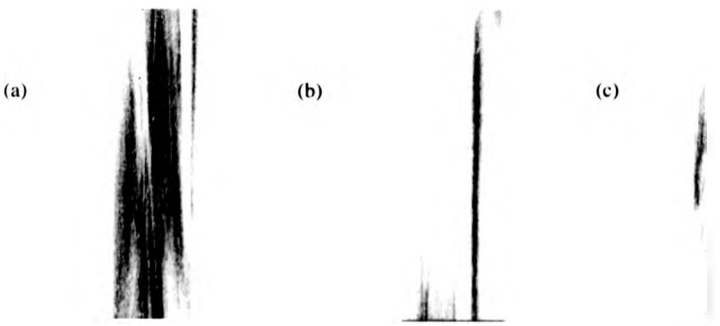

Figure 3.10 Topographs from the regions marked in Figure 3.9 (a) central peak, (b) satellite peak, with ω and ω-2θ offset, (c) greater offsets.

topograph, and may represent scattering from dislocations. Topograph (c) shows scattering from another small block, and faint dislocations, found by a greater displacement in ω and ω-2θ. These topographs clearly point to the mosaic-nature of the peak-distortion effects, with one (or more) blocks present in the x-rayed area, with a slight *d*-spacing difference between the blocks and the presence of dislocations.

Other reflections, including 410 and 600, also displayed similar evidence of

large-scale blocks, to differing extents depending on the reflection and the area of the sample exposed to x-rays.

3.3.1.3 Conclusion

The sample possesses a non-ideal structure, caused mainly by large mosaic effects, showing it to be imperfect compared to a similar pure KTP crystal. The mosaic structure is inhomogeneous across the sample width, with some regions exhibiting increased peak-splitting in the reciprocal-space maps compared to others. Topography shows the mosaic blocks have different dimensions. Significantly, the effect appears to have some correlation in the b-direction of the sample, such that along b the defect properties are similar, and for reflections that sample b parallel to the high-resolution direction of the diffractometer, peak distortions are absent.

The significance of the presence of peak-distortion only when the b-axis of the sample is perpendicular to the high-resolution direction of the diffractometer is that this implies the physical features in the crystal that are the cause have some degree of organisation - specifically that their dimension in the c-direction is probably smaller than in the b-direction. The fact that this correlates with the alignment of the surface striae is noted. Whilst bulk-imperfection in the form of high mosaicity can be randomly arranged in a crystal, it appears that in this case it can be related to the surface distortions such that mosaic blocks are either longer in the b-dimension, or have similar tilts in this direction. This may explain why the peak-splitting effects are seen differently for different exposed regions of the sample crystal. The block-feature imaged in Figure 3.10b is, for example, lengthened in the direction parallel to the surface striae for the alignment of this reflection.

Physically this can be interpreted by the presence of homogeneous growth within a sector bounded by the edges of one large striation or group of striations, which is slightly mis-aligned with respect to the growth in a neighbouring region. This corresponds to a suggestion that the striae, and associated mosaic blocks can be

smaller than the dimension of the x-ray beam in the diffraction-plane, i.e. ≈1mm (depending on reflection geometry), borne out by the fact that the block in Figure 3.10b is contained within the width of the beam. Dislocations are also seen, suggesting further imperfections in the sample.

3.3.2 Ta:KTP

The sample of Ta:KTP was grown by a 4% substitution by mass into the flux components. The crystal was free of coloration, and was chosen because it exhibited comparatively lower surface striation effects (unlike other members of the Oxford Ta-doped growths with higher Ta concentrations) visible to the naked eye, and comparable to some pure KTP growths. It possessed the typical geometry of the KTP family, and unlike the Nb-doped crystal of section 3.3.1, suffered less severe frustration of the growth in the a-direction, or the other growth facets. Similarly, the a-faces appeared generally free of surface striations and other visible defects. The crystal was grown around a pure KTP seed, and showed a region of dense defects and fractures around this, extending a millimetre or so from the seed itself. Remote from the seed the crystal appeared unflawed under optical-microscopic inspection.

The a and c samples were harvested in the manner that device-crystals would be: from the large flat regions to either side of the central seed, to obtain representative samples that would reflect the features a typical device sample would possess. The b-sample was obtained from the central portion of the crystal. The samples were first aligned with Laue diffraction, then cut with a diamond saw into approximately 25mm^2 prisms, each 0.5mm deep. Polishing with a selection of grades of diamond-loaded pads (see section 3.3.1.1) produced optically flat samples, of a consistent thickness. Under an optical microscope, the samples showed no unusual effects, and appeared generally free of imperfection.

3.3.2.1 Results and discussion

The HRXRD study of the Ta:KTP samples revealed a material largely free of reciprocal-space features associated with defects, pointing to an overall high

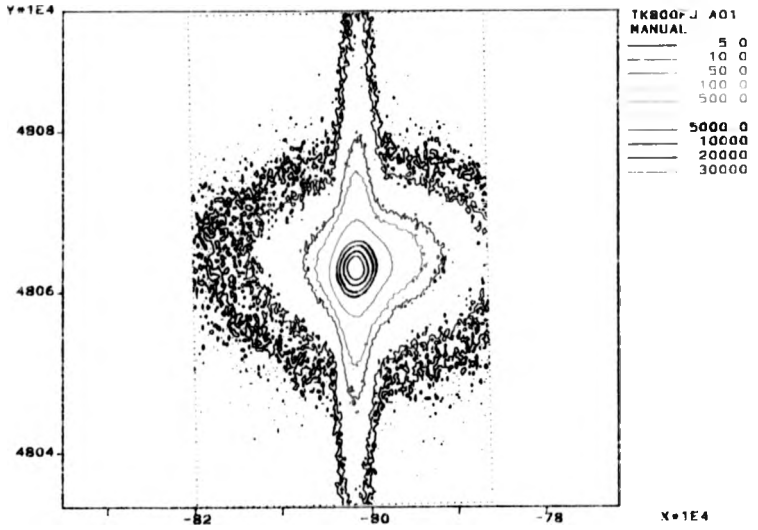

Figure 3.11 Reciprocal-space map for 800 reflection from Ta:KTP.

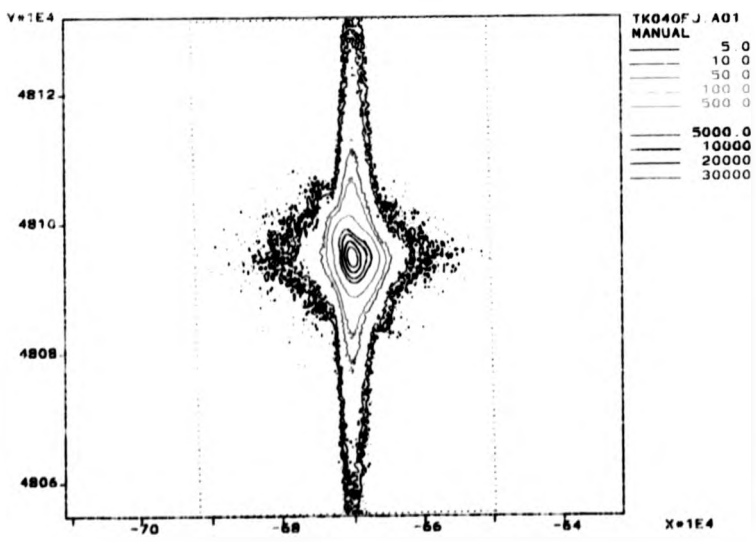

Figure 3.12 Reciprocal-space map of 040 reflection from Ta:KTP, showing generally symmetrical profile.

perfection of the crystals themselves. Particularly, analysis of both sides of the a and c-axis samples revealed only rocking curves and maps as may be expected from pure KTP, possessing both similar FWHM parameters and similar peak intensities as well as symmetric, undistorted RLPs. An example reciprocal-space map is seen in Figure 3.11 and is generally symmetrical with a strong surface streak and extended diffuse scattering in the ω-equivalent direction, implying a degree of mosaicity.

Simple symmetric reflection studies of the b-sample did reveal some features associated with imperfect structures. In particular, evidence of peak distortion in the rocking curves was found, and reciprocal-space-map analysis of the RLPs revealed similar peak-splitting to that found in Nb:KTP. The peak distortion and splitting was more limited in extent, not achieving the multiple-peak splits seen for Nb:KTP. The effects were observed in 040 and 080 reflections, with the crystal axes randomly arranged around ϕ, and were inhomogeneous across the sample width. The reflection of figure 3.12, for example, has a strong surface streak, and only slightly extended diffuse scattering meaning the region exposed here was close to ideal.

Perhaps the most striking feature was that seen in Figure 3.13. This reciprocal space map was taken of a simple 040 reflection with the sample aligned (by previous optimising of the 201 reflection) such that the a-axis was perpendicular to the high-resolution direction of the diffractometer, and a region towards the edge of the sample was irradiated. A rocking-curve ω-scan suggested a highly-distorted diffraction peak. High-resolution scans then suggested acquiring a reciprocal-space map: in several regions, the central peak possessed a distortion and several satellites in the same ω-direction, each with lower intensity. Translating the sample, and then re-optimising the reflections revealed different peak-splitting. The reciprocal-space map of Figure 3.13 exhibits the most dramatic effect, with effectively two RLPs, separated by a slight omega-offset, and of comparable profile and intensity. The peaks also demonstrate a slight *d*-

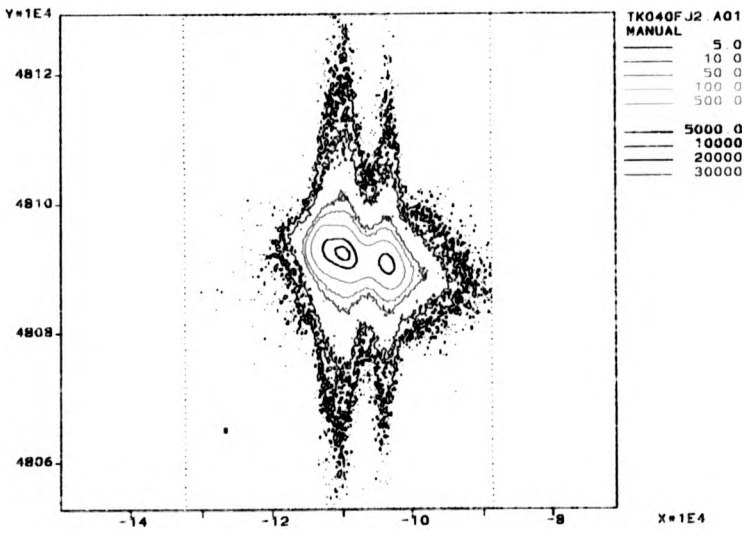

Figure 3.13 Reciprocal-space map for 040 reflection from Ta:KTP, showing two distinct Bragg peaks, each with surface-streak.

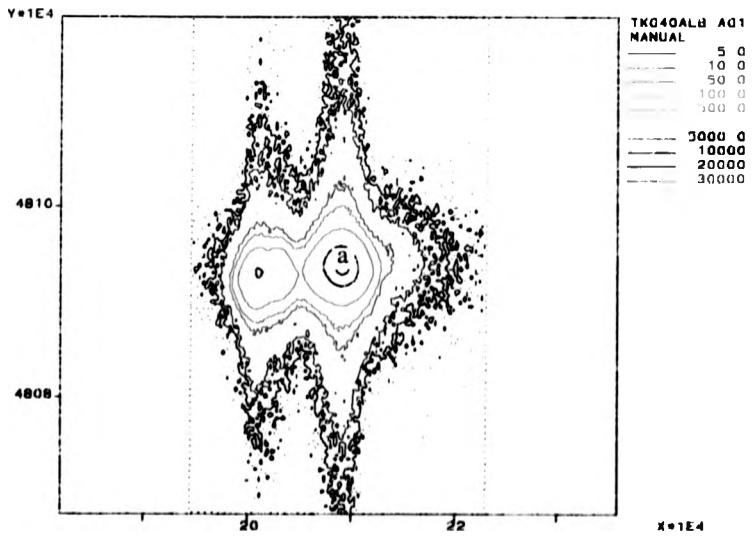

Figure 3.14 Reciprocal-space map of 040 reflection from Ta:KTP, obtained by a 0.05° rotation in ψ, and showing different intensity distribution to Figure 3.13.

spacing irregularity. By rotating the sample in ψ and quickly re-mapping, this *d*-spacing separation reduced, and then reversed, showing this to be merely a geometrical effect and not correlated to real *d*-spacing variation. Figure 3.14 is the inverse case from that in Figure 3.13, with the less intense peak in Figure 3.13 now the most intense. Whilst the geometrical effects of a ψ-rotation mean a slightly different region of the crystal is x-rayed, the general similarity of the maps suggest that the same features are present in each. The diffuse halo around each peak possesses a surface streak that suggests relatively high perfection. The topograph of Figure 3.15a is from the position marked (a) at the peak of the reciprocal space map in Figure 3.14, and reveals that the crystal is scattering in distinct portions. The photograph of figure 3.15b is an expansion of the 040 topograph taken from the peak of a distorted RLP (simply possessing extended diffuse scattering in ω), scattered from a nearby region of the crystal. It shows evidence of dislocation networks, and missing intensity, though not to the extent seen in Figures 3.13 and 3.14. This region is a conventionally mosaic structure, with dark dislocation-lines and angular tilts extending the diffuse scattering, and is typical of the only other defect structures found in this sample, generally in the same half of the crystal.

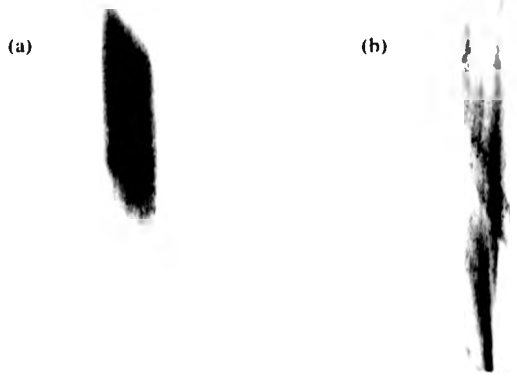

Figure 3.15 Topograph from 040 reflections from Ta:KTP (a) peak of grossly-distorted map in Figure 3.14, (b) nearby region of crystal, showing simply dislocations and small-scale mosaicity.

Amongst the various other reflections examined from all three samples, both sides, high-resolution scans showed only features as may be expected for pure KTP and exhibited no distinctive features. For some reflections, marginally higher intensity was seen in the ω-scan tails than might have been expected, though this is probably attributable to regionalised defects or mosaic blocks.

3.3.2.2 Conclusions

The perfection of the Ta:KTP sample produces almost ideally undistorted reciprocal-space nodes during the high-resolution analysis. Where the b-sample shows significant evidence of a block-structure in the material, with one particular portion of the crystal possessing a giant-block effect, and a nearby peak showing evidence of dislocations, the nature of the crystal is shown by synchrotron topography in Chapter 5 (section 5.3.6). The crystal has a large growth-sector boundary, the meeting of the {001} and {011} facets, to one side of the centre. Since the high-resolution study found evidence of the tilted block in one region of the crystal only, and the angular separation was large enough to cause the peak-splitting seen in figure 3.13, it seems likely that the high-resolution axis of the diffractometer was sampling the regions either side of the GSB. These can possess angular inconsistency with respect to each other, and indeed modified dopant take-up. If this latter occurred, it was not significant enough to demonstrate *d*-spacing adjustments in the crystal. Whilst the topograph of the nearby portion of the crystal shows evidence of high-defect-density, it is regionalised and can be associated with defect propagation from the GSB or seed/sample interface. Such defects are indeed imaged in the topographs of section 5.3.6, propagating out from the central region. They were not seen in other HR experiments, since no evidence of peak distortion was found for the rest of the bulk crystal. Whilst they would have been imaged in the relevant HR topographs, their contribution to structural distortion is thus confined close to them, and they do not influence the bulk perfection greatly.

3.3.3 TaGa:KTP

The sample of 4%Ta4%Ga:KTP was cut as an a-plate from near the centre of the as-grown crystal, since this sample would cover the region extending into the bulk of the crystal in which any grown-in defects would be found.

3.3.3.1 Results and discussion

The initial symmetrical-reflection analysis, performed using 400 reflections, was obtained by irradiating separate regions of the sample. Then, further 800 reflections were used similarly to section 3.3.1.2, since these are less surface-sensitive and would probe any bulk defect-structure. Further to this, random orientations of the in-plane crystallographic axes were used with the same regions exposed to x-rays at the setting for 800 to determine if any defects found were direction-sensitive, as found in the Nb:KTP case.

The rocking-curves for all of these reflections in general revealed no significant features, presenting undistorted profiles, intensities and FWHM's generally in close agreement to those of pure KTP for the same crystal settings. Similarly, the reciprocal-space maps generated from selected diffraction experiments were symmetrical and undistorted, with the only effect being an indication of mosaicity in some of the maps. Figure 3.16 shows the 800 reflection from one section of the sample, where the b-axis of the sample was perpendicular to the high-resolution direction. The peak has a strong surface-streak, and distortion in the diffuse scattering.

Interest was, however, seen for certain of the 820 reflections, where peak-splitting distortions were visible on rocking-curves in high resolution scans centred at the RLP. Figure 3.17 shows a reciprocal-space map for this reflection. This map possesses a surface streak, and shows evidence of peak-splitting with angular variations and *d*-spacing differences (confirmed by ψ-optimising).

The topographs of Figure 3.18 are taken at the points indicated on Figure 3.17. The topograph in Figure 3.18a shows strong scattering from a region to the bottom left of the exposed area and missing intensity above this. A part of this

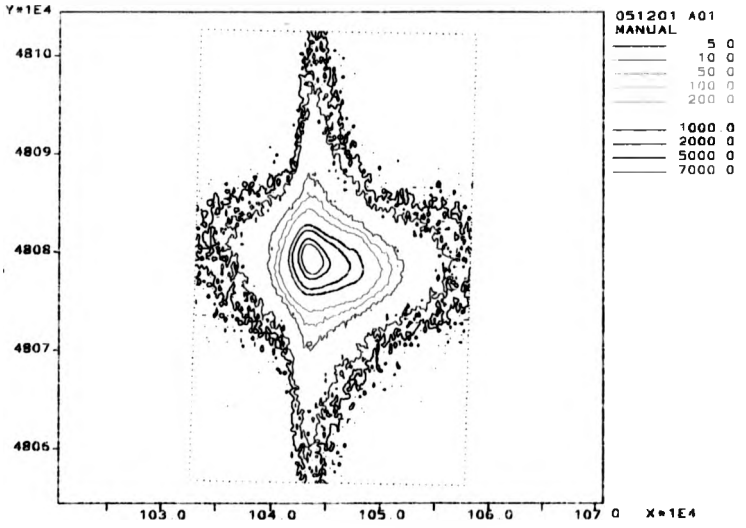

Figure 3.16 Reciprocal-space map for 800 reflection from TaGa:KTP, showing distinct surface-streak.

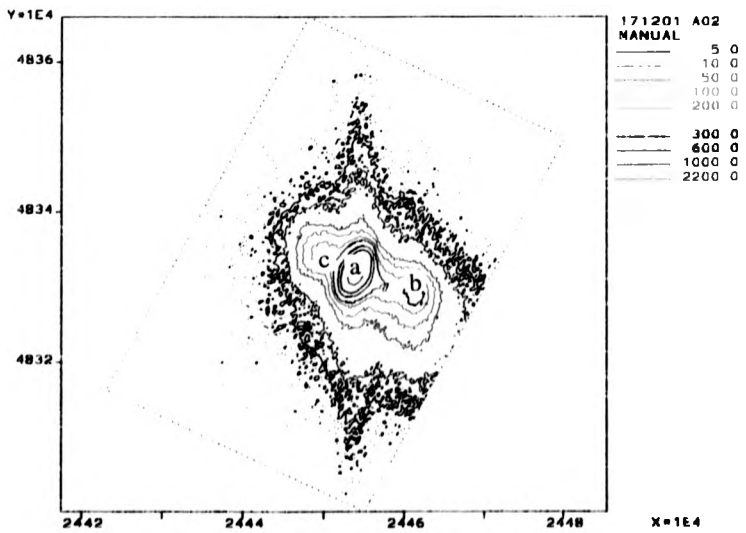

Figure 3.17 Reciprocal-space map of 820 reflection from TaGa:KTP, possessing multiple satellite peaks indicative of defect structures.

intensity is seen in Figure 3.18b, which has different tilt and *d*-spacing (and is fainter). The image in Figure 3.18c is an expansion from a topograph taken from near the smaller satellite of Figure 3.17. It shows a complex distribution of intensity, possibly due to the presence of dislocations in the region being irradiated.

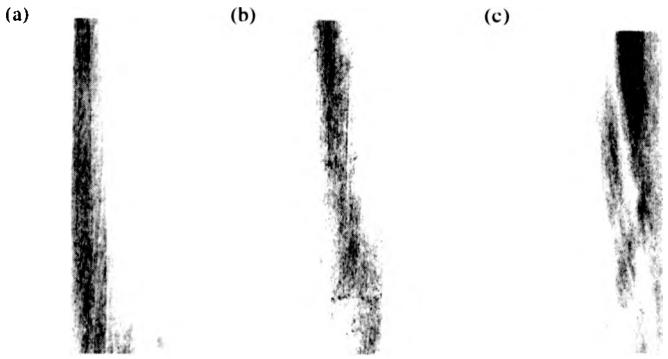

Figure 3.18 Topographs for the 820 reflection from TaGa:KTP. (a) from peak in Figure 3.17, (b) from intense satellite to peak, (c) expansion from topograph from near to the least intense satellite to peak in Figure 3.17, showing dislocations.

These topographs suggest that this region of the sample crystal possessed both gross block mis-alignment and *d*-spacing differences, possibly attributable to different dopant take-up in the blocks. The blocks also appear to be larger than the sampling width of the x-ray beam, at least in one dimension. Dislocations are seen in the same region.

Analysis with reflections with high anomalous-scattering contributions was performed. This produced evidence of similar defect-sourced peak distortion, but to a lesser extent to that in Figure 3.17. Figure 3.19 shows a map from a 2 0 10 reflection which has slight asymmetry in the diffuse scattering, and is typical of the effects seen. This suggests the features found in 3.17 are regionalised, and not necessarily seen elsewhere in the sample by chance.

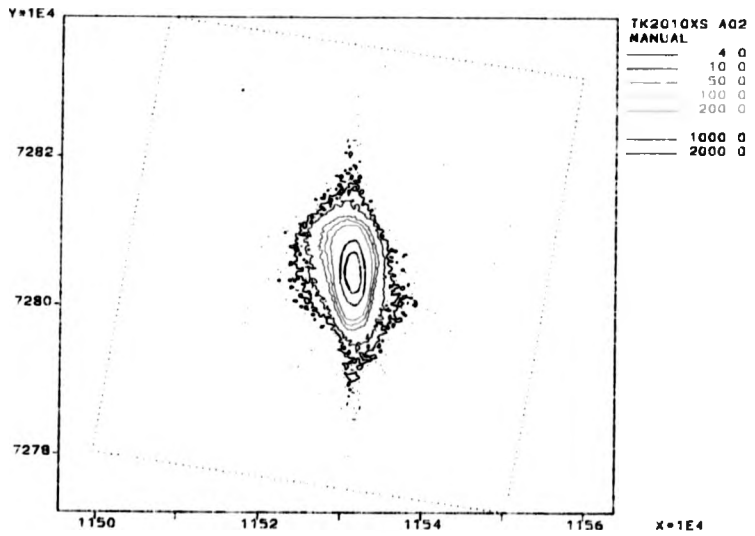

Figure 3.19 Reciprocal-space map of the 2 0 10 reflection from TaGa:KTP, possessing only a slight distortion in the diffuse scattering.

Whilst anomalous-scattering reflections can be used to verify the existence of domains through differential scattering, in this case this was not possible due to the difficulty of locating the same area to x-ray on opposite faces of the sample.

3.3.3.2 Conclusion

The reciprocal-space maps and topographs taken for this sample demonstrate that it possesses imperfections similar to that seen in the Nb:KTP case, though not to the same degree. Regionalised blocks with angular tilt and *d*-spacing differences are seen, though not necessarily correlated to the alignment of the sample with respect to the diffractometer axes. Reciprocal-space maps and topographs from the 820 reflection from one region of the sample demonstrated these effects the most, probably due to the bulk-probing geometry of the reflection.

3.4 Summary

The 10%Nb:KTP sample showed evidence of large block features, correlated with the striations seen on the sample surface. When the b-axis of the sample was perpendicular to the high-resolution axis of the diffractometer, this is seen in reciprocal-space maps and associated topographs, and demonstrates that the sample is highly imperfect, caused by possibly inhomogeneous growth. Dislocations are seen, and the long blocks can be significantly smaller than the dimension of the x-ray beam in the high-resolution direction (≈1mm). Changes in *d*-spacing between blocks were suggested by some of the reciprocal-space experiments.

The 4%Ta:KTP sample has a higher degree of perfection, and produces reciprocal space maps ideally close to those from pure KTP. Regionalised defects are seen, such as dislocations, and one feature appeared to affect the whole width of the sample. This was identified in reciprocal-space maps as two regions with significant angular misalignment between them, but each possessing a degree of perfection and scattering intensely. Evidence from Chapter 5 was used to illustrate that this feature is a growth-sector boundary crossing the width of the sample. The high-resolution analysis suggested the different growth-

sectors possessed the same *d*-spacings, which implies similar dopant take-up. Dislocations were seen in high-resolution topographs from regions near the growth-sector boundary.

The sample of TaGa:KTP produced reciprocal-space maps and topographs that indicated similar defects to those seen in Nb:KTP, though to a lesser extent. Large-scale blocks and evidence of *d*-spacing differences were seen, but were not correlated to sample alignment, or, more particularly, surface striae.

The suggestion is made that the mosaic structure can be related to the surface striae, with small-grain boundaries that run in sheet-like fashion at some angle relative to the c-axis and parallel to the b-axis. This would correlate with differential crystal growth on the striae surfaces during the flux-growth process. As growth proceeded, block-like features would form in the striae directions, with each block possessing a degree of perfection, but being mis-aligned with respect to its neighbouring blocks. Whilst Ta:KTP does not exhibit this effect in the reciprocal-space analysis, this is most likely due to its relative perfection compared with the other samples. The block-structures in TaGa:KTP are more difficult to correlate to surface striae, but the crystal itself showed frustrated growth, and the presence of other defects may hide the effect. Some evidence of correlation to sample alignment of TaGa:KTP was still seen.

3.5 References

[1] P.F. Fewster. *J. Appl. Cryst.* **18,** (1985) 334

[2] L. K. Cheng, L. T. Cheng, R.L. Harlow, J.D.Bierlein. *Appl. Phys. Lett.* **64,** (1994) 155

[3] P. A. Thomas, B. E. Watts. *Solid State Commun.* **73,** (1990) 97

Chapter 4

Structure determination and refractive index simulation for 4% Ta:KTP

4.1 Crystal structures and structure determination

The analysis of a crystal's structure can give a vital physical basis for understanding or predicting the properties the bulk material will have. Previous structural knowledge can also lead to theoretical prediction of the likely structure a new material, with desired properties, may possess, or point to the particular problems associated with an existing material.

Various x-ray methods can permit the determination of the absolute atomic positions in the unit cell of a crystal: such structure-determination experiments have become more powerful tools as computer technology has evolved since the 1960's. Early structure determination relied on chemical experiments and the symmetry data from diffraction results (such as Laue photographs), or powder diffraction to solve simple unit cells. Modern diffractometers permit rapid access to reciprocal-space data, from even single-crystal experiments, and desktop computing power allows rapid processing of the data along with sophisticated electron-density models to produce solved structures for the most complex of unit cells.

4.1.1 The SMART system diffractometer, and CRYSTALS.

The Siemens SMART diffractometer is a conventional laboratory x-ray diffractometer, driven by a dedicated computer system and software. It combines a conventional molybdenum x-ray source with a κ-goniostat for sample manipulation, and a CCD area detector system with a fixed 2θ (low and high-angles) setting - see Figure 2.4 (Chapter 2) for a schematic representation of such a diffractometer. An Oxford Cryosystems cooling device is also available for low

temperature diffraction experiments. Samples take the form of a prepared sphere, with dimensions that take note of the absorption coefficient of the sample. The sphere is glued to a quartz fibre which is carefully positioned at the centre of rotation of the diffraction stage in the plane of incidence. A succession of rotations around the κ axis combined with low and high angle placings of the area detector allow access to large areas of the reciprocal space of the sample.

A typical experiment will first acquire several frames from the sphere in a random orientation. This allows a visual inspection of the data that can determine if the sample is free from defects such as cracking or twinning. A short data collection run is carried out, with coarse steps covering a modest volume in reciprocal space. These data generate an orientation matrix for the sample, and the software suggests the path that the diffractometer will take as it carries out the full diffraction experiment. This path takes account of the volume of reciprocal space to be covered, the geometry of the diffractometer and the time taken for the whole experiment. The whole scan will then acquire thousands of frames each sampling a specific region of reciprocal space, taking up to 45 seconds each for up to 14 hours.

Once these raw data are collected, a spherical absorption correction (see ITFC Vol. III[1]) is applied by a software procedure. The data are then converted into a listing of *hkl*, F^2_{obs} and σF^2_{obs} for input into a refinement program. The refinement package used here is the CRYSTALS program, written by Watkin, Carruthers and Betteridge[2]. The input model data includes cell parameters with e.s.d's, space-group and atomic positions. The program firstly removes reflections that are unobserved, systematically absent or badly measured, and merges the equivalent ones, disregarding the weakest reflections (which improves the statistical confidence). Then refinement then proceeds by full-least-squares analysis. As each cycle of calculation ends, a residual, or R-factor is produced which measures the confidence of the refinement.

The parameters to be refined during the process are scale, the extinction

parameter, the enantiopole parameter, and the individual atomic parameters.

Scale

This brings observed and calculated data on to the same scale.

Extinction parameter

This corrects for systematic errors due to isotropic extinction. These errors make $F_{obs} < F_{true}$ and an adjustment is made to F_{calc} to reflect this. The corrected structure factors are calculated using expressions of the type:

$$F'_{calc} = F_{obs} \{ 1 - nX (F^2_{calc} / \sin \theta) \} \qquad (4.1)$$

where n is a small constant and X is the extinction parameter.

Enantiopole or Flack parameter

This corrects for the presence of a degree of inversion/polar twinning in the crystal. The model for the corrected intensities of specific reflections is thus:

$$I_{total} = (1 - x) I_{h\,k\,l} + x I_{\bar{h}\,\bar{k}\,\bar{l}} \qquad (4.2)$$

where x is the Flack parameter, and can vary from 0 to 1; 0 meaning there is no contribution from the inverted structure. This can be related to the presence of twinning in the crystal.

Atomic parameters

These are the atomic co-ordinates, the isotropic thermal parameter Uiso, and the anisotropic components U_{11} to U_{12}, and the site occupancy. Observing these parameters as the refinement progresses allows an interpretation of the successfulness of the refinement if similar values for model materials are known, or physical information can be inferred from the parameters themselves.

Measuring the goodness of fit

The final stage is to assess the goodness of fit between calculated structure and the details of the real data. The primary parameter used for this is the R-factor.

The R-factor is a good measure of the match between the refined structure and the structure of the crystal because it is related to the observed structure factors, F_{obs}, and the computed ones, F_{calc}. The observed structure factors are obtained directly from the intensity data, and then R is calculated as: (summed over all of the reflections)

$$R = \frac{\sum_i [F_i^2{}_{obs} - F_i^2{}_{calc}]}{\sum_i F_i^2{}_{obs}} \qquad (4.3)$$

If a data set has been collected well, with efforts taken to minimise systematic errors such as absorption effects, an R-factor of 3% or less can be expected for a KTP-like structure once the model is correct. In least-squares refinement, a model can be assumed to be "correct" once the refinement has converged. Structural models that contain errors are not improved by successive refinements, and thus do not converge to produce a small R-factor.

The weighted residual, R_w, is a corrected R-factor that takes note of the individual contributions of the data reflections:

$$R_w = \frac{\sum_i w_i \{ [F^2_{obs} - F^2_{calc}]^2 \}^{1/2}}{\sum_i w_i F^2_{obs}} \qquad (4.4)$$

where w_i is a weighting parameter introduced to give the individual observations differing significance, reflecting strong and weak reflections and their proportional importance in the refinement. The weighting parameter can be defined in many different ways, depending on the quality of the data. For the refinement performed here, the weighting scheme was chosen as a simple $w=1/\sigma^2$ since the data covered many thousands of reflections, giving good statistics.

The R-factor (in correspondence with the weighted R-factor) is not by itself a reliable guide to the correctness of a model structure. It must be considered

together with other parameters of the model, and finally the structural details such as particular bonds and positions, which must be chemically sensible.

When all these parameters take acceptable values, and the refined structure is sensible (i.e. particular bonds are as expected, the charge-balancing is correct) and the R-factors suggest the refinement has converged, then the refined structure can be assumed to be a good fit to the experimental data, and represent a good model of the real crystal structure.

4.1.2 Sample preparation and data collection

The sample of 4%Ta:KTP was coarsely broken up in an agate mortar and pestle. By examining the fragments under an optical microscope, a selection of regularly - shaped micro-crystals approximately 1mm in diameter was made. These were placed in a spheruliser, where the microcrystals are blown against emery paper by a continuous low-volume stream of N_2 gas, gradually removing protruding angles. When the crystals were removed, the most spherical of the micro-crystals was selected, and several samples of approximately 0.3mm in diameter were chosen. These were cleaned of the fine dust remaining from the spherulising process, since such crystalline debris still adhering to the samples may diffract, and contribute segments of powder rings to the diffraction data. The samples were mounted onto the tip of quartz fibres, with diameters below approximately 0.2mm, using a resin glue. These fibres were then fixed with wax into copper studs (which fit into the goniometer of the kappa-manipulator on the diffractometer) such that approximately 1cm of the fibre was free - in order that the copper stud did not impinge on the x-ray beam.

By viewing through an optical telescope and repeating 90° rotations of the kappa goniostat, adjustments to the screw-positioners were combined to locate the crystals onto the centre of the diffraction stage, with a centricity error significantly smaller than the diameter of the crystal.

Where fast scans of the samples revealed distorted or split diffraction peaks, as displayed by the software, the sample was discarded. Such features are

characteristic of either a fractured or twinned crystal, or one with large lattice defects, and these would provide data of insufficient quality to be used in a structural refinement.

The optimally prepared Ta:KTP sample was approximately 240 μm in diameter, checked by optical microscopy and initial x-ray scans. It was cleaned in a stream of N_2, and fixed into a stub on a quartz fibre of approximately 200μm diameter. Data collection was performed at room temperature. The angular ranges over which data were collected were: 2θ low (28°), ω = 28°, ϕ from 45° to 225°, 2θ high (56°), ω = 56°, ϕ from -90° to 180°, capturing 22011 reflections. Each frame lasted 10 seconds, with a total experimental running time of ≈15 hours. File handling and treatment were performed at the data-collection workstation, with a reduced raw data set transferred to PC for refinement.

4.1.3 Results

Summary of parameters of data collection and refinement are in Table 4.1

	4%Ta-doped $KTiOPO_4$
Crystal shape and size	Sphere, diameter 240μm, accurate to ≈10% on two axes.
Linear absorption coefficient (cm^{-1})	41.3
Diffractometer	Siemens SMART
Scan	ω-2θ
Radiation	Mo $K\alpha$
Lattice Parameters (Å)	a = 12.821(1), b = 6.408(1), c = 10.595(3). Unit cell volume 870.45(2) $Å^3$
Ranges of h, k, l measured	h -22 to 22, k -11 to 11, l -19 to 19
Intensity control	Automatic
Number of reflections measured	22011
Number of reflections used for refinement	5488 when merged, 4477 satsify I > 10σ(I)
R_{int} (%)	4.34
Absorption correction	Empirical (spherical)
Data processing	CRYSTALS[1]
Model structure	$KTiOPO_4$
Refinement method	Full-matrix least-squares (CRYSTALS[1])
Weighting scheme	$1/\sigma^2$
Number of parameters	153
R (Weighted R) (%)	1.92 (2.80)
Extinction parameter	188.2(5)
Flack parameter	0.03(1)
Δρmin , Δρmax (e $Å^{-3}$)	-1.29, 1.69

Table 4.1 Details of data collection and refinement.

Refinement began without allowance for any Ta occupation on Ti sites, and after isotropic refinement of scale factors, the R-factor settled at a high value of ≈5%. It was noted that the extinction parameter also took a high value (compared to typical values found for KTP[3], ≈130) of 227, whilst the enantiopole parameter was 1.22, suggesting a large problem with the model. At this point, the structure was inverted, to change from enantiopole ≈1 to 0, so that co-ordinates of peaks in the difference map could be read reliably. Observation of the difference map then showed a peak of electron density of 2.8 e $Å^{-3}$ at the Ti(1) site, whilst Ti(2) possessed only 1.92 e $Å^{-3}$, implying the need for inclusion of a heavier scatterer than Ti on Ti sites. A small percentage of Ta, occupancy 0.04 (based on assumed 100% incorporation of the Ta dopant), was therefore introduced at the same co-ordinates as Ti(1) and Ti(2), and the two atom types were constrained to be equivalent.

Isotropic refinement for this model achieved an R-factor of ≈ 4.1% with up to 5 additional peaks appearing in the difference maps. The Ta(1) site refined to a higher occupancy of 5% compared to the 3% at Ta(2). Anisotropic refinement improved the situation somewhat, producing a sensible enantiopole parameter of 0.019, whilst the extinction parameter continued to vary. A better R-factor of 2.09% (weighted R, 3.33%) was achieved, and the difference map was considerably cleaner with $\Delta\rho_{max}$ of 1.7 e $Å^{-3}$ and $\Delta\rho_{min}$ of -1.77 e $Å^{-3}$, the mean electron density was -1.07 e $Å^{-3}$, meaning $f_{calc} > f_{obs}$ on average. Further peaks were seen in the difference maps when the cut-off level was dropped to 1 e $Å^{-3}$ in view of the better refinement.

The potassium occupancies were then refined, to check for charge-compensation by potassium vacancies (with reference to the previous Nb:KTP study[4]) and to improve the difference map by removing the extra peaks. Anisotropic refinement produced a much-improved R of 1.92%, and a weighted R of 2.80%. The final K occupancies were 94(1)% on the K(1) site and 92(1)% on the K(2) site. The difference map, however, showed two significant extra peaks, of 1.77 e $Å^{-3}$ and

1.68 e $Å^{-3}$ respectively, with a reduced $\Delta\rho_{max}$ of 1.77 and $\Delta\rho_{min}$ of -1.29 but an increased mean electron density of -2.11 e $Å^{-3}$, though several of the additional peaks seen previously disappeared.

Since the occupancies of Ti and Ta were fixed until this point they were refined, beginning with an assumed 4% Ta occupancy on Ti(1) and deleting Ta on Ti(2), to determine if the Ti(1) site was dominant. But this refinement produced a higher R-factor of 8% and numerous extra peaks in the difference map. The Ta on Ti(2) was reintroduced, and the two occupancies were allowed to refine themselves, achieving a final occupancy of 3.9%Ta on Ti(1) and 2.6%Ta on Ti(2). Attempts to refine the remaining P and O occupancies resulted in O occupancies of >100%, probably due to correlations, and so the P occupancies were fixed at 100%, and anisotropic refinement resumed to achieve a final refinement with an extinction parameter (of 188) more within the expected range for KTP-type compounds. The R-factor was 1.93% (weighted 2.79%), suggesting a good convergence, with a difference map showing two extra peaks of 2.15 and 1.80 e $Å^{-3}$ and a smaller mean residual density of -2.0 e $Å^{-3}$. Analysis of these two peaks showed that they were located precisely at the hole-sites in the KTP unit-cell.

The model achieved here was certainly acceptable, though it presented problems of K vacancies at too high a level (compare Nb:KTP structural study). It is the model summarised in Table 4.1. The existence of a few significant residual peaks in the difference maps for KTP-like materials was previously related to possible occupation at the hole sites in the structure, and the K-vacancy problem was associated with this. With reference to recent studies[5], the refinement was continued for a limited number of cycles to attempt to incorporate O vacancy and improved K-vacancy statistics by refining these site occupancies.

The $I:\sigma(I)$ ratio was changed from 10 to 3, such that more weak data were included in the refinement. A difference map then revealed peaks on K(1), K(2), and the hole site adjacent to K(1), but not on the other hole site. Attempts to

refine oxygen occupancies resulted in similar difficulties to the earlier attempts: occupancies tended to refine to >100%, and so O occupancies were fixed at 100%. The K occupancy was then increased to 100%, and allowed to refine, achieving the same final K occupancies found above (i.e. K(1)=94%, K(2)=92%), meaning that the structure was still not charge-balanced and suggesting an inadequacy in the model.

Because of this, the K occupancies were fixed at a level (0.96) commensurate with a charge-balanced structure (assuming 100% Ta-take-up), and the whole structure was allowed to refine anisotropically to investigate whether a closer refinement could be made. Observation of the difference map now revealed a significantly different picture: one of the K(2) peaks and the final hole-site peak were absent. This strongly suggests that they may originally have been symptoms of incorrect, low, K-site occupancies. Two peaks of poor shape, of 1.7 e $Å^{-3}$ remained at K(1) and K(2), but are likely to be artefacts. The remaining major peak had a high density value of 2.13 e $Å^{-3}$, a good shape, and was located in the structure at a site very close to K and O(1) and O(2), distances of 1.63Å, 1.60Å, and 1.26Å respectively.

4.1.4 Discussion

The structural co-ordinates for the final refined model are given in table 4.2.

The refinement brings several important things to light. Firstly, the dominance of the Ti(1) site in attracting the dopant ions is demonstrated by the improved difference maps when the ions are included, and by the fact that the two sites subsequently refine to 3.92% on the Ti(1) site and 2.66% on the Ti(2) site. This is in agreement with previous structural refinement performed for Nb:KTP[4], where the Nb ions were found to enter the structure preferentially on the Ti(1) site, though in this case the difference between Ti(1) and Ti(2) was much greater. The radii of Nb^{5+} and Ta^{5+} are comparable, hence the difference in site take-ups must be due to electronic structure differences.

The mean bond lengths and significant bond angles for Ta:KTP and undoped

KTP in Table 4.3 show that mean bond-lengths for both Ti sites are slightly increased, which is consistent with the increased unit-cell volume for Ta:KTP compared to undoped KTP.

Atom	*Occ.(%)*	*x*	*y*	*z*	U_{iso}
K(1)	94.3(2)	0.37821(4)	0.78095(7)	0.31116(5)	0.3782(1)
K(2)	91.2(2)	0.10509(3)	0.69781(8)	0.06670(5)	0.1051(1)
Ti(1)	96.1(6)	0.37293(2)	0.50025(3)	0.00117(2)	0.3726(2)
Ti(2)	97.34(5)	0.24717(2)	0.26763(3)	0.25211(2)	0.2472(1)
Ta(1)	3.92(6)	0.32761(2)	0.50016(3)	0.00100(2)	0.3726(2)
Ta(2)	2.66(5)	0.24713(2)	0.26770(3)	0.25201(2)	0.2471(1)
P(1)	fixed	0.49821(3)	0.33709(5)	0.25980(4)	0.4982(3)
P(2)	"	0.18110(3)	0.50182(6)	0.51216(4)	0.1811(1)
O(1)	"	0.4856(1)	0.4864(2)	0.1491(1)	0.4856(2)
O(2)	"	0.5101(1)	0.4667(2)	0.3823(1)	0.5101(1)
O(3)	"	0.40050(9)	0.2000(2)	0.2795(1)	0.4005(4)
O(4)	"	0.59366(8)	0.1936(2)	0.2407(1)	0.5937(2)
O(T1)	"	0.2244(1)	0.9656(2)	0.6427(1)	0.2244(3)
O(T2)	"	0.2240(1)	0.0409(2)	0.3895(1)	0.2240(2)
O(5)	"	0.11234(9)	0.3115(2)	0.5401(1)	0.1123(1)
O(6)	"	0.11165(9)	0.3115(2)	0.4867(1)	0.1117(1)
O(7)	"	0.2528(1)	0.5404(2)	0.6272(1)	0.2528(2)
O(8)	"	0.2532(1)	0.4614(2)	0.3988(1)	0.2532(1)

Table 4.2 Atomic positions and isotropic temperature factors for the unit cell.

The bond-angles in the Ti-O chains are all very slightly altered in the doped case, as expected. The intra-octahedral bond angles for both Ti(1) and Ti(2) are increased by ≈0.2°, whilst the inter-octahedral angles are decreased by ≈0.12°, meaning that the octahedra are widened along c - as expected for inclusion of the larger Ta atom. The long axes of the two octahedra are also at less of an obtuse angle to each other, bringing the Ti sites into closer proximity.

The average deviation from the mean bond-length is reduced for the Ta:KTP case, being 0.084 for Ti(1)-O, and 0.071 for Ti(2)-O (cf. 0.090, and 0.079 for pure KTP). This suggests an increased symmetry of the TiO_6 octahedra: the Ti(Ta) site is thus found to have slightly increased centricity compared to KTP (involving modest shifts - note the similarity of the mean Ti-O bond-lengths for both cases), with a slight preference for the Ti(2) site. The Ti(1)-OT(1) and Ti(2)-OT(2) long bonds are both reduced (by ≈0.7%) compared to KTP, and the

Ti(1)-OT(2) and Ti(2)-OT(1) short bonds are increased (by ≈1.2%) in length. Thus the Ti-site is indeed more centric, whilst the anomalous short/long nature of the Ti-O chain is reduced by ≈1% in bond-lengths. The incorporation of the larger Ta atoms thus seems to force the structure to eliminate some of the distortion to the TiO_6 octahedra. Since the substitution of Ta averages to only 3.3%, and the centricity of the Ti(Ta) sites alters the short/long bond pattern by shifts of only 1%, it seems that the centricity is unlikely to be the source for significant NLO property modification in the material.

Mean Ti-O bond-lengths (Å) *(and average deviation from mean (Å))*	**4% Ta:KTP**		**KTP**
Ti(1) - O	1.973(0.084)		1.972(0.090)
Ti(2) - O	1.969(0.071)		1.967(0.079)
Ti - OT - Ti chain linking angles			
OT(1) - Ti(1) - OT(2)	94.82°		94.74°
OT(2) - Ti(2) - OT(2)	175.44°		175.14°
Ti(2) - OT(1) - Ti(1)	135.85°		135.99°
Ti(1) - OT(2) - Ti(2)	133.23°		133.36°
Bond lengths, and error (Å)		*(proportion)*	
Ti(1) - OT1 *(long)*	1.964(1)	<	1.981(1)
Ti(1) - OT2 *(short)*	1.735(1)	>	1.716(1)
Ti(2) - OT1 *(short)*	1.756(1)	>	1.733(1)
Ti(2) - OT2 *(long)*	2.078(1)	<	2.092(1)

Table 4.3 Bond-lengths and bond-angle comparison for Ta:KTP and undoped KTP case.

When the model reached acceptable status (prior to the final O/K vacancy refinements) the two good-shaped peaks in the difference map of 2.15 and 1.80 e $Å^{-1}$ appeared exactly at the hole sites already well known for KTP-materials[6]. Whilst this residual electron density could be evidence of genuine crystallographic site occupation, recent research[5] suggests that such features can also be introduced by refinement of erroneously low K-occupancies in KTP

analogues. The K vacancy for this model averaged to ≈5%, whilst the Ta doping averaged to ≈3.3%. Since Ta is a pentavalent substitute for Ti^{4+}, this K vacancy is too large by almost a factor of 2, and thus displays the problem of attributing the residual electron density.

The final attempts to address this, and refine the K occupancies resulted in similar charge-balancing problems and O occupation problems. Only when the K vacancy was fixed at a charge-balancing level (4%) did residual electron-density disappear at one hole site, and then anisotropic refinement removed density from the other hole site. This suggests that they were indeed artefacts of an incorrect model. The final, good-shape peak in this map sits very close to K, ≈1.63Å, and is 1.60Å from O(1) and 1.26Å from O(2). Its size and good shape suggest it may be a real feature. There is a possibility that it is related to the real position of Ta in the structure - up until this point, Ta has only been allowed to sit at the Ti(1) and Ti(2) sites in the structure, consistent with other previous findings for doped KTP. Since the Ta atoms appear to sit preferentially at Ti(1), then inadequacies in the model close to the Ti(1) are to be expected. The newer structure does, however, charge-balance to a better degree and may be considered more structurally pleasing.

4.1.5 Conclusion

The bond-angle adjustments and average Ti-O bond changes found in the Ta:KTP case point to an increased centricity of the Ti sites in the Ta:KTP structure compared to the positions found for pure KTP. Whilst these shifts destroy some of the anomalous short/long character of the Ti-O chain deemed responsible for KTP's NLO behaviour, the chain does still possess an anomalous short/long nature. The small percentage shifts in position are unlikely to be the source of modified NLO response: the electronic character of the Ta atoms is the contributing effect. The occupancies of the two Ta sites suggest that, consistent with the Nb:KTP case, the Ta atoms prefer to site at Ti(1). Thus we see that the Ti(2) octahedra are proportionately smaller, and are twisted towards the Ti(1) octahedra in the Ta:KTP case. The Ti(1) octahedra remain more distorted than

for Ti(2) (i.e. larger average deviation from mean for the Ti-O bonds), and the Ti(2)-O average deviation from mean has been affected to a greater extent by the doping, which is consistent with the preference of the Ti(1) site.

The structural refinement gives non-sensible values for K vacancies if these are allowed to refine independently. Refinement of O vacancies then gives non-sensible O occupations, and so when the K occupancies are held at charge-balanced ratios, a different structural interpretation is seen. This suggests a possible new site for Ta atoms, close-to a hole site and the two tetrahedral O sites O(1) and O(2). The previously modelled Nb:KTP structure[2] suggested that the increase in average K-O bonds is due to the lack of K atoms acting as "spacers" in the structural framework, which can also account for the shorter Ti-O bonds, as the remaining structures nearby to a K vacancy contract inwards. Compared to the structure found in this case, the K vacancies could act in this manner, affecting the local structure, yet the modifications to the Ti-O bonds may also be caused by the interstitial position of Ta, close to O(1) and O(2), remotely affecting bonds in the Ti-O chain. The combined effect may be responsible for the increased centricity of the Ti sites.

4.2 Refractive indices

Since the refractive indices of non-linear optical crystals are vitally important for understanding both the non-linear activity and wavelength window capabilities of the materials, accurate measurement of the birefringence is vital. Simulation of the refractive indices from structural data is also important since it can explain the source of the materials NLO response, which can then be used to suggest improvements to the structure.

To measure the refractive indices of a material can, however, involve complex experimentation if accuracy beyond the 3rd decimal place of the index is required. Similarly, to simulate the optical activity of the crystal structure can involve a long iterative process if the refractive indices obtained by experiment are to match sufficiently those obtained by the simulation.

4.2.1 The critical angle technique for refractive index measurement

There exist many methods of measuring the refractive index of a material, with various accuracies depending on the method. The best known high-accuracy technique (typically to the 4th decimal place) is the minimum angle technique. This technique requires forming the sample into a highly perfect prism, with extremely accurately characterised angles, such that the entry and exit angles of the probe light source can be measured accurately as it traverses the prism. For fast measurements of the refractive index, for measurements for extremely small samples, or for measurements where the material is hard to prepare into a suitable prism, this method is demanding in time and technology and may even be impossible.

An alternative method, that can provide the same accuracy with a reduced sample preparation is the critical angle method. Here a well characterised reference prism is placed in contact with the sample, and light is introduced along the interface as a parallel beam. This being the critical angle condition, measuring the angle of exit of the light from the reference prism, and knowing its refractive index can give the refractive index of the sample to an accuracy proportional to the accuracy of angular measurement. The most significant advantage is that only one face of the sample need be prepared, by flat-polishing. Where a birefringent sample is used, then several samples corresponding to the principal axes are required, though of course each sample need only have one facet prepared.

In this manner, a high-resolution critical angle experiment has been set up at Warwick, using an optical angle encoder on a PC-driven goniometer arm to measure the exit angle accurately, and with a cubic zirconia reference prism. Light is provided by a mercury-vapour lamp with a telescope and slit assembly to collimate the input light, and with wavelengths selected by appropriate filters from the mercury spectrum. The experiment has been calibrated with reference high-accuracy glasses, and reliably returns refractive indices with errors in the fourth decimal place of order 0.0004.

4.2.2 OPTACT

The optical properties of crystals can be successfully calculated using the established polarisability theory. By using a model where each atomic position of the unit cell is described as a point-dipole oscillator, the optical activity and refractive indices can be found to be in close agreement with experiment. The approach works by calculating the response of each dipole to the propagating light-field and then summing all the responses to give the global optical polarisation. Particularly, from this component-based approximation it is also possible to gain important insights into the source of the materials' characteristic optical behaviour by identifying the important ionic configurations in the unit cell. Information gained about the linear optical response of a material can, by the Miller rule, be related to the NLO response as well, further extending the value of this kind of simulation.

The OPTACT program, by Devarajan and Glazer[7], is a dedicated point-dipole theory program that operates on the polarisation ellipsoid associated with each atomic position in a model unit cell, and was designed to produce accurate optical activity simulation for crystals. The program is a reworking of several successive theories for the computation of optical activity. It is based mainly on the work of Reijnhart[8], who applied a theory by Ewald that the response of each atom or ion in a medium to an incident light-field can be considered to be represented by an infinitely small electron-oscillator at its centre. This electron possesses an isotropic free-atom polarisability, and is the basis of the 'point-dipole' model. OPTACT achieves its simulation by combining the microscopic analysis (formed from the summation of the point-dipole oscillators) with a macroscopic analysis based on Maxwell's equations applied to calculating polarisation. This essentially 'classical' solution has its own flaws, since it makes no allowance for quantum-mechanical interactions during optical activity, and since in a classical model, all the interaction between dipoles are assumed as the same type. This latter problem causes the calculation to fail in situations where atoms in a crystal see a highly irregular environment.

The program requires an input data set describing the wavelength of the radiation used for calculation[*1] , a number of parameters that control the convergence of the summation (in real and reciprocal space, usually set at $\pi^{1/2}$ and the cube-root of the cell-volume). A list of the unit-cell co-ordinates of the crystal is combined with a list of the isotropic polarisability volume ($Å^3$) associated with each atom-type. The initial values of these volumes are generally obtained by intuitive guesses based on previous analyses.

Calculation sums the response of the crystal's point-dipole oscillators, and tries to find an effective polarisability for each atom in the unit cell (an explanation of the mechanisms of the calculation is beyond the scope of this thesis).

Amongst the output of the program, such as a calculation of the optical rotatory power of the crystal, is a calculation of refractive indices (for each crystal axis) and the associated birefringences the material should possess at the simulated optical frequency. These parameters are the data of interest here.

4.2.3 Results of refractive index measurements for 4%Ta:KTP

Sample preparation from the crystal followed the established procedure of Laue-alignment and cutting and polishing (similar to that followed in section 3.2) of the sample into a cube approximately 3mm across a side.

The sample data obtained is presented in table 4.4. The wavelength was chosen as the central wavelength amongst those available from the experiment. The data were taken as a result of 3 separate measurements, and the repeatability error accounts for the error figures in the data - these random errors are larger than the systematic experimental error, and probably result from inconsistencies at the sample/matching-fluid/prism interface, as well as placing errors as the automated system finds the edge of the refracted light beam from the prism.

[*1] Since the program's calculation is essentially a 'static' simulation, the wavelength parameter only enters the calculation to scale the output refractive indices from the calculated polarisations.

Table 4.4 Experimental refractive indices and birefringences for 4%Ta:KTP.

Wavelength: 5766 Å

$n_x = 1.7686(2)$ $n_y = 1.7807(3)$ $n_z = 1.8869(3)$

$\Delta n_{xy} = 0.0121(5)$ $\Delta n_{yz} = 0.1062(6)$ $\Delta n_{xz} = 0.1183(5)$

The measured birefringences demonstrate an increase over those found for pure KTP (at this λ) of: Δn_{xy} =0.0102, Δn_{yz} = 0.0934, Δn_{xz} = 0.1036. n_z in particular is much larger in the 4%Ta:KTP, consistent with Ta's greater polarisability than Ti influencing the Ti-O chains in the unit cell. Comparison to the n_z for 2%Ta:KTP[9], n_z = 1.8817(8) show that increasing Ta doping increases refractive indices, and birefringences, particularly Δn_{xz}. Incorporation of the larger Ta on Ti sites dilates the Ti octahedra, and hence alters the unit cell and induces increases in the refractive indices.

4.2.4 Optical simulation for Ta:KTP

The input parameters for the OPTACT simulation were built up from the atomic position data for the unit cell of the sample, generated by the refinement process on single-crystal diffraction data in section 4.1. Each atomic position was also accompanied by a three-parameter sequence defining the ellipsoid of the ionic polarisability of that site.

The refinement was performed by defining the polarisation ellipsoid of the two P atoms as negligibly small in order to remove this degree of freedom from the simulation, a procedure previously deemed acceptable[2]. Therefore, concentration is mainly on the TiO_6 octahedra and the K-O cages[10]. Initial values for these remaining atoms were taken from the values arrived at from previous pure KTP experiments. The various O atoms were initially assigned identical values, though in refinement, different atoms took different values reflecting the individual behaviour of the O atoms in KTP-materials. The value for the K ions were kept constant (with one exception) throughout the simulation since previous experience suggested that their contribution is less important to achieving a

match than modifying the various O parameters[2]. For example, the polarisability ellipsoids of the O atoms in the Ti-O bond chain (labelled OT(1) and OT(2)) are crucial in modifying the simulated birefringence, as they reflect the important contribution to the SHG characteristic of KTP. Table 4.5 shows the input parameters for the first approximation.

Ion	*Polarisability Volume* ($Å^3$)
K(1)	0.90
K(2)	0.90
Ti/Ta(1)	0.185
Ti/Ta(2)	0.185
P1	0.001
P2	0.001
O1	1.656
O2	1.656
O3	1.656
O4	1.656
OT1	2.66
OT2	2.66
O5	1.656
O6	1.656
O7	1.656
O8	1.656

Table 4.5 Input parameters for OPTACT modelling.

By iterative inquiry, and using knowledge gained from previous investigations of pure KTP simulation, the polar parameters of Ti/Ta, OT(1) and OT(2), then O(3) to O(8) were modified sequentially, bringing the output refractive indices of the simulation closer to those found experimentally. Since the iterations mapped a process effectively operating in many-dimensional parameter space, the closest point of approach of model and data could be found in several polarisation-set configurations. Some of these could of course be discounted due to physical unsuitability, and the final parameters were determined as the best approach of the simulation to the experimental values found amongst the possible outcomes.

4.2.5 Results

The output for the initial polarisability volumes in table 4.5, gives the corresponding simulated refractive indices as: n_x = 1.7812, n_y = 1.7867, n_z = 1.8578. These n_x and n_y values are less than 0.6% higher than the correct values,

whilst n_z was 2% too low. The first adjustment made was a reduction of the volume of both K sites to 0.85 $Å^3$ as a concession to the K-vacancies seen in the refined structure of section 4.1. This produced output refractive indices of: n_x = 1.7766, n_y = 1.7820, n_z = 1.8550, which are closer to the correct values. Further decreases in these volumes produced a linear reduction in all three indices, taking n_z further below its correct value. The K-ion polar volume of 0.85 $Å^3$ was thus retained as the basis for further simulation, since it brought n_x and n_y into closer agreement, is only an ≈5% reduction from initial values, and is an allowance for K-vacancies seen in the structure.

Since the Ta substitution introduces a pentavalent ion onto the Ti site, the polarisability volume of the two Ti sites was increased by a nominal amount. This affected the value of n_z the most. Increasing the volume to 1.86 $Å^3$ gave output values of n_x = 1.7766, n_y = 1.7820, n_z = 1.8550.

Next, the volumes of OT(1) and OT(2) were varied to fit the n_x and n_y parameters. Since these bonds are chiefly responsible for the NLO response of the KTP family, forming the anomalous-linked Ti-O chain in the c-axis, the volume of both ions was increased from the starting value of 2.66 $Å^3$. A volume of 2.8 $Å^3$ produced a 0.8% increase in n_x, a 1% increase in n_y and a 2% increase in n_z, bringing n_z to 1.8893. Increasing the volume of OT(1) and OT(2) to 2.9 $Å^3$ increased all three indices again, giving a final n_z of 1.9164. Whilst n_x and n_y were now too large, the polar volume of OT(1) and OT(2) was left at 2.9 $Å^3$ since the modifications to the other O ion volumes were not found to influence n_z to the same degree as this, and thus in reducing the n_x and n_y values by further simulation, n_z would be brought closer to the correct value.

By varying particular pairs of atoms, the individual refractive indices were adjusted. Though altering the polarisability volume of any atom in the structure affects all of the optical indicatrix, one refractive index can be affected to a greater extent than the others. O(3) and O(4) corresponded to greatest variation in n_x, O(5) and O(6) to n_y, and O(7) and O(8) to n_z. Figure 4.1(a) to (c)

demonstrates the relationship for the three refractive indices to the relevant polarisability volume, each graph starting from the same initial model: for example, for Figure 4.1(a) the gradient of the line corresponding to n_x is the greatest. All three relationships are linear in the three graphs.

By balancing the adjustments made to these pairs of atoms, the simulated refractive indices were brought close to the experimental data. However, whilst a close match could be achieved for both n_x and n_y simultaneously, n_z remained furthest from its correct value. By adjusting OT(1) and OT(2), and then reoptimising the O(3) to O(8) atom pairs, this situation was improved, but the closest match was achieved by increasing O(1) and O(2) and reoptimising O(3) to O(8). O(1) and O(2) scaled all three indices by approximately the same amount.

(a) (b)

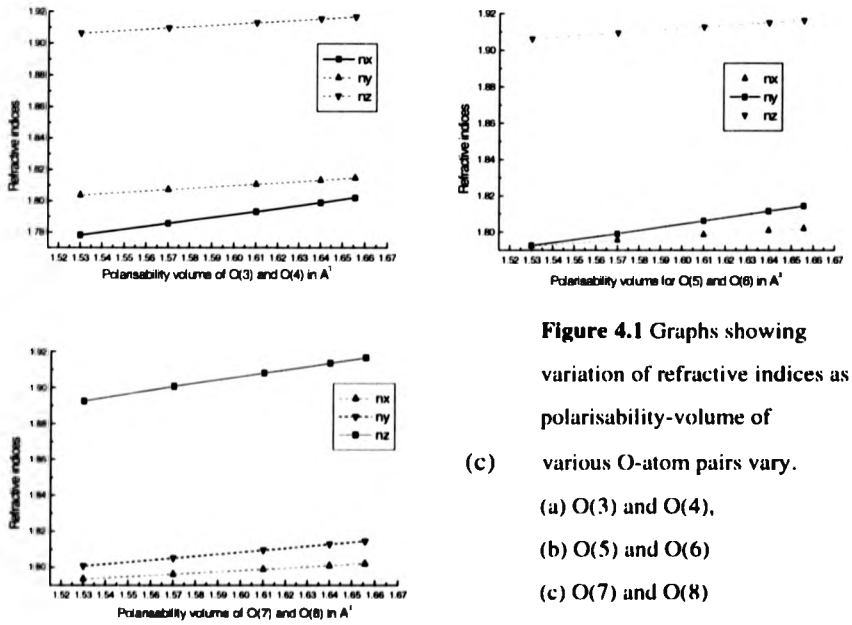

(c)

Figure 4.1 Graphs showing variation of refractive indices as polarisability-volume of various O-atom pairs vary.
(a) O(3) and O(4),
(b) O(5) and O(6)
(c) O(7) and O(8)

The final parameters, where a good match was found for all three refractive

indices, are shown in Table 4.6, and give a refined OPTACT output for refractive indices summarised in Table 4.7. This final model was determined as the product of useful iterative modification to the polarisability volumes.

Ion	*Polarisability Volume* ($Å^3$)
K(1)	0.85
K(2)	0.85
Ti/Ta(1)	0.186
Ti/Ta(2)	0.186
P1	0.001
P2	0.001
O1	1.659
O2	1.659
O3	1.528
O4	1.528
OT1	2.911
OT2	2.911
O5	1.590
O6	1.590
O7	1.557
O8	1.557

Table 4.6 Final input parameters of polarisability volume for the OPTACT simulation of refractive indices

Model wavelength: 5766 Å
$n_x = 1.7681$ $n_y = 1.7826$ $n_z = 1.8861$
$\Delta n_{xy} = 0.0145$ $\Delta n_{yz} = 0.1036$ $\Delta n_{xz} = 0.1179$

Table 4.7 Table of OPTACT refined refractive indices and birefringences.

Notably, these data are a close match, but not necessarily within the experimental error boundaries of the critical-angle measurement. This is consistent with previous such refinements for KTP, where the convergence of experiment and simulation for KTP-family members has been found difficult. A match of the order seen in this data is acceptable, and whilst further iterations of the polarisability parameters may achieve closer match for some of the refractive indices, no further important physical information is likely to be gained.

4.2.6 Discussion and conclusion

The contribution of O(3) and O(4), O(5) and O(6), O(7) and O(8) to the refractive indices n_x, n_y and n_z in that order is due to their location in the unit cell of KTP. By examining the partial unit-cell shown in Figure 4.2, it is clear that these atom pairings sit at the extremities of the Ti octahedra in the relevant crystallographic directions. The contribution to axial electron-responses of these pairs is thus along the axis that separates them, though the sum effect influences the global electronic signature, and thus affects the other refractive indices, to a lesser extent.

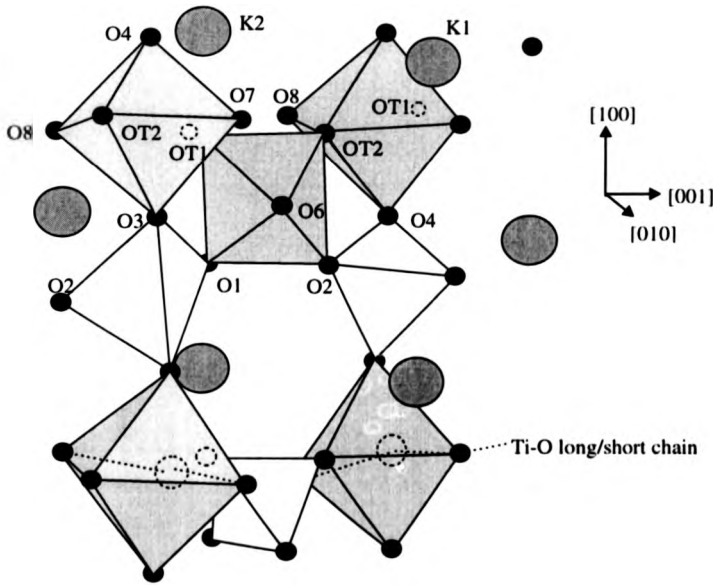

Figure 4.2 Schematic diagram of generic KTP structure. Darker octahedra are Ti, lighter tetrahedra are P, larger spheres are K, smaller spheres are O. The diagram represents a partial unit cell, demonstrating the significant O ions, and showing the Ti-O chain.

Similarly, the significance of OT(1) and OT(2) for modifying n_z is clearly due to

their location in the unit cell, though the significance of the presence of these atoms in the anomalous short/long Ti-O bond chain (the source of KTP's nonlinear response) is marked by the increased polarisability volume ascribed to them compared to O(7) and O(8) (also in the c-plane of the Ti octahedra). This larger volume also reflects the fact that the incorporation of Ta into KTP involves placing an ion that is more polarisable than Ti on the same site in a unit cell.

The volumes of OT(1) and OT(2) had the most significant impact on the refractive index n_z, yet the balance of the O(3) to O(8) parameters, in parallel with the adjustments made to the K, P, and Ti parameters corresponding to physical arguments, could not achieve the closest match to the experimental data. The O(1) and O(2) parameters remained as the last contribution to matching the two sets of data. Given the suggestion in section 4.1 that Ta may site at an interstitial location between O(1) and O(2), the increases in the polar volume of these sites that brings about the close match may substitute for the contribution of Ta, which was not included in the input data set at the new location.

The increased birefringences compared with KTP, seen for the simulated and measured refractive indices, account for potentially increased optical performance of the material over that of KTP. The cause of this increased birefringence is the large polarisability volume of the Ta atoms, which acts primarily to increase the refractive index along the polar, c axis of the material. The possible interstitial site for the Ta atoms suggested by the structural refinement in section 4.1, is reflected by the influence of O(1) and O(2) in the simulation of refractive indices.

Incorporation of Ta, at the 4% level, achieves extension of the birefringence of this KTP derivative compared to that of KTP, and thus it has potentially an improved optical performance. Whilst the centricity of the Ti sites is increased in the doped case, the similar effect seen for Nb:KTP suggests that the NLO character of the material is not lost, and underlines the role of Ta's large polarisability in the NLO character of Ta:KTP.

4.3 References

[1] International Tables for Crystallography, Kluwer Academic Press, London (1995)

[2] D.J. Watkin, J.R. Carruthers, P.W. Betteridge. CRYSTALS User Guide. Chemical Crystallography Dept. University of Oxford, England.

[3] P.A. Thomas, S.C. Mayo, B.E. Watts. *Acta Cryst. B* **48,** (1992) 401

[4] P.A. Thomas, B.E. Watts. *Solid State Comm.* **73,** (1990) 97

[5] P.A. Thomas, M.N. Womersley. *Acta Cryst. B* **54,** (1998) 645

[6] P.A. Thomas, A.M. Glazer. *J. Appl. Cryst.* **24,** (1991) 963

[7] V. Devarajan, A.M. Glazer. *Acta Cryst. A* **42,** (1986) 560

[8] R. Reijnhart. Dissertation, Delft (1970).

[9] C. Schetelich, private communication.

[10] P.A. Thomas. Inst. Phys. Conf. Ser. No 103:Part 1(1989) 59[3]

Chapter 5

Synchrotron topography of Ta and TaGa:KTP

5.1 Introduction

The growth characteristics of Ta/Nb doped KTP have already been described (see chapter 1). Many doping experiments result in a crystal with high defect-density, including coarse inclusions, growth steps (i.e. surface striae) and dislocations. The examination of crystals with defects by synchrotron topography is a powerful way to determine the nature of the defects due to the radiation's high-brightness, low divergence and large and wavelength-spread. It provides a rapid method of imaging the defects, and in a white-beam topography experiment multiple images can be collected simultaneously using only the simplest of alignments. Hutton *et al*[1] performed such topography to assess the quality of their TSSG KTP, whilst Liu *et al* [2] used the technique to examine crystals of ≈5%Nb:KTP.

Here, various doped KTP samples have been examined using white-beam synchrotron topography, and the features seen in the images are related to growth striations, growth-sector boundaries, dislocations and ferroelectric domains.

5.2 Experimental procedure

6.1.1 High-resolution study

Synchrotron topography (see section 2.5) can be performed in a number of experimental configurations, each extracting different information from the diffraction at the crystal such as the volume-effect probing of transmission-Lang topography.

5.2.2 Synchrotron details

The topography experiments took place at station 7.6 (Topography) of the Daresbury Synchrotron Radiation Source (SRS), UK., with beam currents of between 100 and 200 mA. The station is a large distance from the storage ring, some 80m, and provides intense, highly-collimated white-beam radiation, which is gathered from a standard bending magnet.

Inside the station hutch a remotely-controlled vertical/horizontal slit assembly is available, and since each blade of the slits is independently controlled, they can be used to define the profile of the x-ray beam proceeding onto the sample.

The topography experiments used the white-beam radiation camera in a transmission-Lang configuration. This camera is a large open Eulerian cradle centred on the diffraction axis, with rotation axes remotely controllable by computer and precise to approximately 0.1° with automatic back-lash removal. The detector arm and goniometer assemblies provide multiple fixing points for a variety of detection/sample mounting options. Figure 5.1 is a schematic diagram of the set-up used in these experiments.

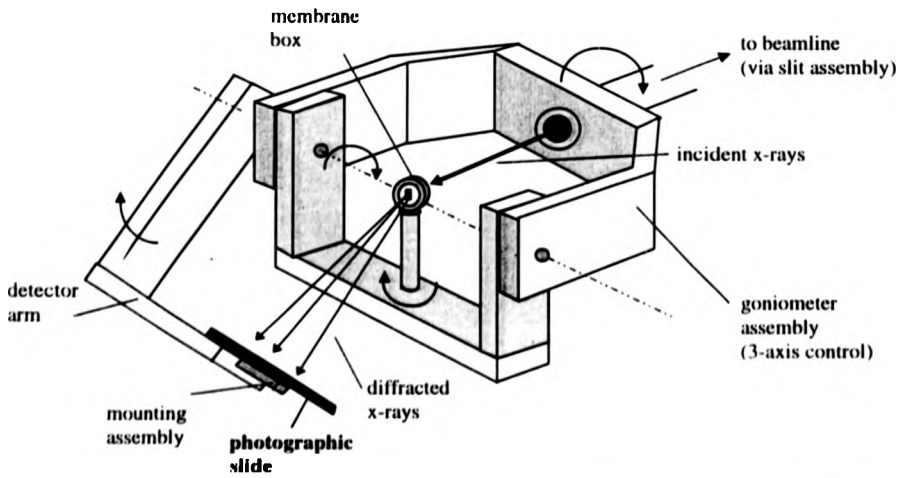

Figure 5.1 Schematic representation of white-beam radiation camera

5.2.3 Sample identity and preparation

The samples used in these experiments were: 4%Ta:KTP and 4%TaGa:KTP.

All sample crystals were flux grown by the crystal-growth group at the Clarendon Laboratory, Oxford.

In transmission topography, the absorption of x-rays within the sample becomes important. The equation:

$$I/I_0 = e^{-\mu Tc} \tag{5}$$

describes the intensity drop for a thickness Tc for absorption from incident intensity of I_0, with the linear absorption coefficient:

$$\mu = \rho \sum_i g^i \mu^i_m \tag{6}$$

g^i is the mass fraction of element i in the unit cell, μ^i_m is its mass absorption coefficient, and ρ is the crystal density.

For transmission experiments, an intensity drop of <90% is required during traversal of the crystal. This gives a maximum thickness of 300μm for the 4% Ta-doped KTP samples, with μ calculated assuming that the contribution of the dopant ion is negligible. In calculation, λ was set at the wavelength of Mo kα (0.71069 Å). This value was used for all samples prepared for consistency, because samples of this thickness are still robust, to a degree, and the intensity available in the synchrotron beam was so high.

The samples were cut as plates from large crystals, which were aligned perpendicular to the crystallographic axes of KTP. Cutting was performed by a diamond saw, leaving a surface which was highly scratched. Initial coarse-polishing (using 50μm polishing paper) was performed to reduce this damage before the samples were etched, but this practice was later abandoned due to its inhibiting effect on the etching process: the etches' aggressive chemical attack on surfaces is highly sensitive to surface area and hence surface roughness. When a rough surface is sufficiently eroded, the shallow surface containing damage and

associated strain is removed, leaving a final flat surface suitable for x-ray topographic experiments. Etching was initially performed by immersing the samples in a reversed Aqua Regia concentrate (i.e. HCl and HNO_3 in a 2:1 ratio) at room temperature, though later a 1:1 ratio gently heated to ≈ 323K was found to reduce etching times to approximately 2 hours. This process produced samples that showed little or no evidence of surface damage in topographs taken of them.

5.2.4 Experimental details.

The samples were mounted between two sheets of polyethylene in a membrane box, held in a manual goniometer at the centre of the white-beam camera. This provided for excellent stability and visual alignment of the sample in the x-ray beam. To negate extraneous scattering effects, the x-ray beam after it passed the sample was first observed by a fluorescent screen/CCD camera and its cross-section was stopped-down using the fine-axis slits to match the sample size. The detector assembly was designed around a fixed mounting on the detector arm which allowed accurate and fast replacement of a film cartridge in the same position once the diffraction experiment was set-up.

Primary sample alignment was performed by using point-Laue imaging, using Polaroid film for speed. Here the film cartridge was aligned perpendicular to the x-ray beam using the alignment laser in the station, then the crystal was repositioned until a symmetrical Laue image was achieved, which also allowed for identification of the crystallographic orientation of the sample.

Specific reflections were then selected by driving the goniometer and detector to precalculated angles (calculated using lattice-parameters for undoped KTP - fine optimisation was performed by repeated experimental adjustments), and the x-ray images were captured on Kodak D4 and D2 x-ray emulsion film, requiring maximum exposure times of 45 minutes when the beam intensity was at its lowest. With some specific reflections the geometry required that the direct-beam radiation passing through the sample was absorbed using a 3mm-thick lead beam-stop to prevent these x-rays from over-exposing the film.

The choice of reflections was limited by the particular alignment of the samples chosen, and the angle-limits of the goniometer and white-beam camera. Symmetrical reflections such as 004 or 080 were collected first, since these required only small angular adjustments and thus involved the minimum of error. Symmetrical reflections are also neither compressed nor expanded by the diffraction process and are therefore easiest to interpret. Furthermore, absorption correction is simplest in the symmetrical case. Then some specific reflections were chosen that could reveal information about the polar domain structure of the samples, such as reflections that possess large anomalous scattering contributions.

5.3 Results and Discussion

The experiments were performed in a series of individual investigations over a short period of time. Initial experiments were performed to determine the value of the procedure, and once this was assured further diffraction experiments were selectively performed. White-beam topography was found to present enough information to identify the significant defect features seen in the samples.

5.3.1 Preliminary results

Initial experiments were performed on several samples of Ta:KTP and TaGa:KTP, which had been cut perpendicular to the major crystal axes, a and b for the TaGa sample, and a c-sample in Ta:KTP. The samples had been cut, polished and etched to a thickness of approximately 0.4mm.

The first topographs were taken of the Ta:KTP, and in initial 0 4 0 reflections appeared to show a series of dislocation-contrast lines randomly arranged across an even contrast background. This reflection also showed bands of dark contrast running approximately parallel to the a axis, with some broader bands only partially extending across the bulk of the sample. These features were identified as sample effects up to 0.5mm in width, and were also visible in the 2 0 10 reflection, with slightly increased contrast relative to the background. Also visible were distinct growth sector boundaries that corresponding to the typical

growth facets of the KTP family, which appeared as faint lines of dark contrast generally in a Y-shape. These features showed altered contrast in reversed crystal settings.

Topographic study of the TaGa:KTP showed that this material was richer in terms of contrast features. The same banding was seen, paralleling the a-axis in reflections from the b-sample.

The most significant effect in topographs from both crystal-types was the numerous thin lines of both dark and light contrast that crossed the topographs in random directions. These were determined as surface scratches and other damage resulting from sample preparation. These features partially obscured the contrast effects assumed to be coming from the bulk defect structure of the crystals, which were notably dim in any case.

During the etching of the Ta:KTP samples, it was discovered that this material was significantly resistant to the etch used, compared to other samples etched at the same time (undoped KTP and TaGa:KTP) despite their identical preparation techniques. Etch times extended to twice that for other samples, and topographs still showed notable evidence of surface damage. All samples were therefore thinned to accommodate absorption correctly, to approximately 0.3mm and carefully repolished and etched.

However, under re-examination by topography the observed defect contrast was adjusted: the a-parallel contrast bands in the Ta:KTP sample were significantly less dominant, and the surface damage resulted in even more distinct contrast features for all samples. This was assumed to be due to the ineffective etching caused by over-polishing the samples, giving a reduced surface area for etch-attack, and a narrowing of the defect structure in the direction of propagation.

For the following series of topographic studies, the samples were coarse-polished only (with paper of ≈5μm, i.e. to remove the worst cutting-damage), and the etching process was modified to the heated 1:1 HNO_3 and HCl solution which was found to be a more effective, faster etch requiring only 1-2 hours. This

technique was found to overcome the topograph imaging difficulties found previously by removing most of the surface damage features from the topographs.

5.3.2 Pure KTP topography

Topographs of pure KTP are generally found free of contrast related to defect structure, because the growth of the material is optimised. The photograph of Figure 5.2 shows an expansion from the topograph of an 040 reflection from an a-sample of undoped KTP, the [010] direction is the shortest dimension in the picture (proportional to a real crystal size of 2mm). Typical defects seen in pure KTP are dislocations, and here they are seen with a low average density of a ≈1 per mm^2, proceeding at small angles to [010] in relatively straight-lines, not quite mutually parallel, labelled A. The dislocation marked B shows several curved portions to its length in the image. Absolute interpretation of the type of dislocation is difficult from this image alone. Evidence from other topographs points to the mixed character of the dislocations, partially edge, partially screw.

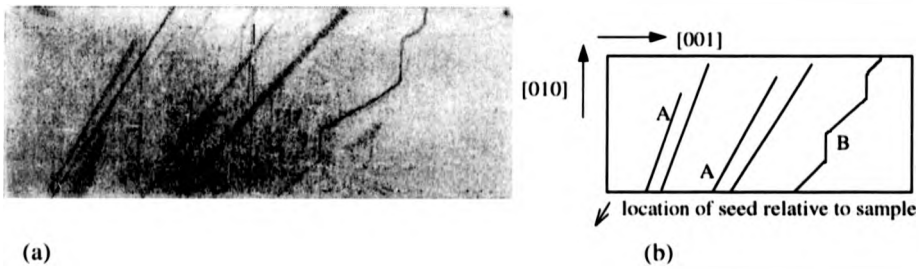

Figure 5.2 (a) Topograph for the 040 reflection from pure KTP (b) Key to features in the photo, showing the dislocation and sample orientation.

The darker contrast seen at the left was attributed to surface preparation damage. The dislocations are also most dense at the left edge of the image, and the right portion shows none. For a typical KTP-growth, this would indicate simply that the seed was located to the left of the sample as imaged, and the dislocations ran from the seed interface into the crystal bulk.

The direction-reversals in dislocation B do not suggest that post-growth motion has occurred, since they are not reversed with respect to the likely direction of growth. Rather the dislocation appears to have encountered different energetic conditions during propagation, perhaps a growth-step on the growing surface, since no growth-sector boundary seems present nearby. In other topographs, The edge of the crystal to the right shows Pendellosung fringes, that are introduced due to the slight wedge at this face. They are typical evidence of high local perfection, and hence quality, suggesting that optimum growth had been established for this portion of the crystal.

Defects such as inclusions or voids are absent in perfectly-grown KTP, and under optimum growth conditions defects like dislocations or point-defects are also minimised. If the growth occurs below Tc then domains will be absent too. Such crystals are highly perfect, and possess the ideal quality required for device production. The worst-case scenario is exhibited by the topograph of Figure 5.2, and since such defect features are absent in perfect KTP topographs, the Figure serves as a good comparison for the following studies of KTP variants.

5.3.3 Topographic studies of TaGa:KTP

The 4%Ta4%Ga:KTP was prepared by cutting a series of samples across the width of an as-grown crystal. Particularly, a large sample was cut perpendicular to the b-axis, since this would be the cross-section that would demonstrate the various features related to growth, which is laterally across this sample, from the seed at the centre, see Figure 5.3. Similarly, the a-sample covered a large part of the bulk width of the sample, such that any grown-in features/defects are contained in the sample width.

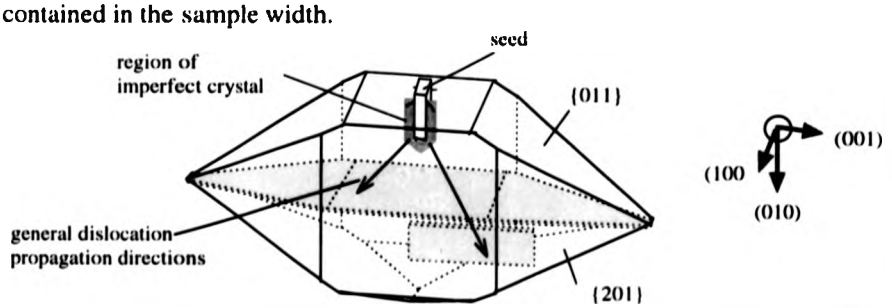

Figure 5.3 Diagram showing location of samples cut from TaGa:KTP

The sample was of interest because TaGa:KTP has produced crystals with radically damaged morphologies, resulting in crystals with no a-growth beyond the depth of the seed, and dense surface striation to the extent that no [100] facet is seen for some crystals. The take-up of Ga is also below detection limits in the crystal[4], yet it appears to affect the morphology and quality of the resulting material. In a simple NLO experiment, a polished block of TaGa:KTP was coarsely positioned and rotated in the output beam of an OPO light source, and demonstrated frequency doubling into the violet visible to the eye.

5.3.4 Results and discussion for TaGa:KTP

5.3.4.1 [100] sample

The symmetrical topographs of the a-sample of the crystal showed evidence of multiple surface scratches as dark contrast lines that had no common direction, but proceeded at approximately 45° to the b-axis, i.e. close to 90° from the [011] or [0 $\bar{1}$ $\bar{1}$] directions and formed cross-like structures. The strain contrast associated with the scratches was imaged in many separate topographs as thin lines with small, irregular deviations along their path.

More significant contrast was revealed by numerous screw-dislocations, present in all reflections with a density of several per mm^2. Similar dark-contrast lines approximately perpendicular to the [011] direction, and with reversed contrast in different images were also seen. In Figure 5.4 the 008 reflection, these features are labelled E, and show dark contrast, which is reversed in the topograph of the 040 reflection in Figure 5.5. Dislocation bundles, labelled B, seen in all the topographs, show this particular region is rich with multiple-type dislocations. The fringes at the right of this image are associated with a region of highly non-ideal growth, since they present modified contrast in different reflections and show numerous internal details.

Figure 5.4 Photograph of the 008 topograph from TaGa:KTP a-sample

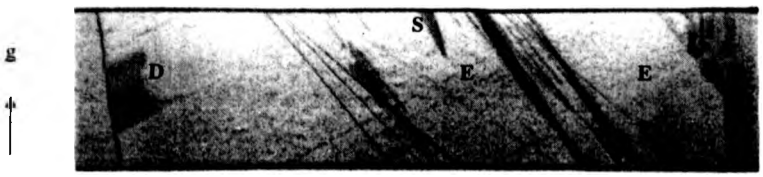

Figure 5.5 Photograph of the 040 topograph from TaGa:KTP a-sample

Other significant contrast features are seen in these topographs. In Figure 5.5, the 040 reflection, a small dark defect with irregular outlines is seen, with one side parallel to a dislocation defect, labelled D. This topograph also shows limited numbers of dislocations, and a small dark contrast feature labelled S (compare to Figure 5.4 which shows the 008 reflection, with modified contrast in this region and many more dislocations). In Figure 5.6 the 2 0 10 reflection is given, and

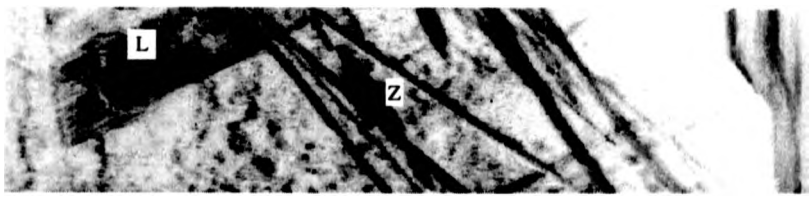

Figure 5.6 Photograph of the 2 0 10 topograph for TaGa:KTP a-sample

displays this same irregular dark feature as part of a larger dark pattern (labelled L) that extends with long axes parallel to the {011} face of the crystal. The presence of parallel lines inside the body of this feature itself, parallel to the edges, is noted. The 008 reflection shows no dark contrast in this region of the sample, save for a line that borders the feature labelled D seen in the 040 reflection from the extended feature, L. The dislocations seen in previous

topographs are visible again here, but are magnified by the reflection geometry.

The large feature L (and D, combined) is a domain, split into two distinct segments, possibly by the action of another defect cutting across its width (the curved line, possibly a dislocation). The geometry of the feature finds it parallel to the 011 growth-facet of the bulk crystal, and bounded on the left by a distinct growth-defect. Where a growth event caused the beginnings of the domain, the imperfect region propagated until a different event reorganises the growth, and thus the feature as a whole is formed parallel to the 011 faces. The faint linear-features inside the domain L are parallel to its edges, and appear to be real, as opposed to being fringes. They may represent local variations in the structure of the domain. Small regions exhibiting the same contrast behaviour elsewhere in the sample are labelled Z, and are likely to be local domains, possibly interrupted in their propagation by the nearby dislocations. Whilst these features could be identified as stacking-faults, their contrast-reversal behaviour in the topographs points to domain characteristics. If one studies the structure-factors of the reflections (see table 5.1) one finds that the anomalous scattering for the reflections 2 0 10 exceeds that of the reflections 008. In the former set, the domains appear in both dark and light contrast relative to the background - the anomalous scattering reflections pointing to the domain case.

Reflection : (*hkl*)	008	2 0 10	808
Structure factor:			
h k l	25762	1969	4188
h k $\bar{l}$	26351	1640	4377

Table 5.1 Structure factors for various reflections from TaGa:KTP, assuming 4% Ta incorporation, and nominal radiation at Mokα.

The features labelled E are absent in the 040 reflection, but are present in the 008. As grown-in dislocations, their Burgers vector would be [001], and they

would be pure edge-dislocation. However, they lie approximately parallel to the {011} growth-facet seen for KTP materials, and the presence of a grown-in dislocation in this orientation is not possible[3] - they are more likely to be post-growth glide dislocations, induced by the strain associated with crystal cooling at the end of the growth-process. The dislocation bundle B possesses many dislocations of different types, lying perpendicular to the {011} facet, and thus these are grown-in, though the high density makes individual type-identification difficult. The grainy features in the lower section of the topograph of Figure 5.6 are unexplained, though there is a possibility that they represent the strain associated with surface damage, magnified by the reflection's geometry.

5.3.4.2 [010] samples

The topographic study of the large b-samples revealed a wealth of contrast features, evidence of the multiple defects present across the width of the crystal, in the central region and wing segments.

Repeated reflections showed a variety of circular features present in the same region of the central sample of the bulk-crystal, with varying shapes in dark contrast. The features were approximately 1.5mm (scaled for sample size) in diameter and were present in both symmetric and asymmetric reflections in a variety of settings with irregular outline and inhomogeneous darkness. Figure 5.7, the 808 reflection from this sample, shows this feature labelled as A. This feature, due to its size is likely to be the strain field associated with a small inclusion, supported by its location near the seed at the centre of the crystal.

A small Y-shaped contrast feature (labelled GSB) was visible in this topograph, crossing the circular features described above, and has edges corresponding to the 2 0 10 growth sectors and a vertical segment in the [100] direction. This is the familiar growth-sector boundary seen in other KTP-family samples, and is revealed by its strain-contrast.

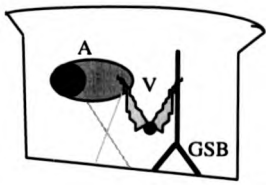

(a) (b)

Figure 5.7 (a) topograph of the 808 reflection from the central b-sample.
(b) Key to features, showing the inclusion labelled A.

A V-shaped feature, with a small dark spot at its base, is seen at the centre of this sample (and hence, the centre of the crystal). It is seen more clearly still in the topograph of the 400 reflection (figure 5.8). A faint dislocation is seen as an X-shaped feature to the left of the image, broadened by the geometry of the reflection.

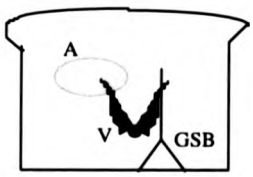

Figure 5.8 Topograph for the 400 reflection from the central b-sample.

In Figure 5.9, the 2 0 10 reflection, this V-feature is absent. This topograph does, however, show the same series of dark contrast bands parallel to the a-axis, and extending across the width of the crystal seen in the other topographs.

Figure 5.9 Topograph of the 2 0 10 reflection from the central b-sample.

The feature labelled V is the strain-contrast induced by a point defect, or congregation of point-defects visible as a dark spot at the base of the "V". The strain-field is not sampled in the 2 0 10 reflection in the same manner as the other reflections, though the dark, a-parallel bands are still seen in this topograph. They are not domain-like features, since they present the same contrast in all these topographs (and the 400 topograph not shown here). Similar features to these are seen in topographs from the wing-segment b-sample. Figure 5.10 shows the 008 topograph for this wing-segment, and two dark a-parallel bands can clearly be seen at the right-hand extremity of the sample.

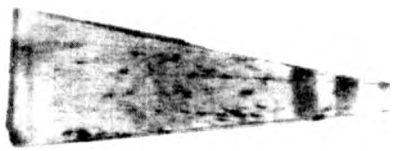

Figure 5.10 The 008 topograph for the wing-segment b-sample.

This topograph also has a series of dark spots, seen more clearly in the 400 topograph of Figure 5.11, and identified as the cross-section of dislocations running approximately perpendicular to the plane of these samples (and thus imaged in the topographs of Figure 5.4 to 5.6, from the a-samples). Figure 5.11 shows some of these spots in an approximate linear arrangement, at a small angle to the {201} edges of the sample. This suggests the dislocations are concentrated partially into a plane (parallel to the b-axis), and thus propagating at approximately the same time through the crystal bulk. The topograph does not show any a-parallel contrast bands, though the 004 reflection (not shown here) does possess contrast in these regions.

This topograph also possesses a curved fringe pattern in the centre, made slightly diffuse by the geometry of the reflection. These patterns are also seen in the 808 and 2 0 10 reflections, and are evidence of a local planar defect.

Figure 5.11 Topograph of the 400 reflection for the wing-segment b-sample

The features in topographs from the opposite b-fragment to that shown in Figures 5.10, and 5.11, show a distinct crack, a scattering feature associated with the fractured tip of the sample, and a few dark, a-parallel, bands. These are similar to the stripes seen in the opposite sample, and exhibit similar effects in other reflections. Analysis of this sample proved difficult due to the damage caused by preparation. During re-preparation, the crack seen in some early topographs ran through the rest of the sample, presumably due to the slight strain induced by heating.

5.3.5 Conclusion

The dislocation contrast lines seen in the various topographs of the a-sample possess irregularity of direction, and others have variation of contrast in different reflections. They are related to the strain-field as the crystal reconstructs around the dislocation, and hence the various alignments caused by the geometry of different reflections will simply perceive projections of the strain. The non-parallel nature suggests that the screw dislocations were not related to growth steps or growth facets, though it is possible that the dislocations originated in a defect at the seed/crystal interface since they are bundled together and propagate towards the {011} faces on the growing surfaces.

In particular, the point-like contrasts observed in the wing-sections of the b-sample are assumed to be the termination of these dislocations on the plane of this sample surface. They are themselves imaged due to the radial strain-field around the end of the dislocation line. They also imply that the diagonal dislocations of Figure 5.5 have a component into the a-dimension of the sample.

That they form patterns related to the (201) surfaces suggests that they originate due to some event during growth - perhaps a specific temperature effect, or a specific defect-event, such as the formation of an inclusion at the seed/bulk interface - and then ran with the growing surface layers.

The Y-shaped growth-sector boundary in the vicinity of the centre of the sample (and hence the bulk of the crystal) is expected, and simply relates to the conjunction point of the various characteristic growth facets of the KTP-family. Since the nearby circular feature is imaged in all reflections, and is thus likely to be the strain contrast around a small inclusion, the imperfect growth in the region of the seed, or related to the particular growth environment at this growth-sector boundary are likely to be its cause.

The broader contrast features are attributed to domains. The feature labelled L in Figure 5.6 is a notable example: appearing only partially in this 008 reflection, and the whole feature is seen in the 2 0 10 reflection - with high anomalous scattering contribution. The feature shows different background contrast in the differing reflections, and internal structure of faint parallel bands. Since the sample was grown above the Curie temperature of pure KTP (and for this material[4]), the formation of domains is possible. Domain production would occur at some change in the growth conditions, and the growing surfaces would extend the domains' dimension until such time as growth conditions again altered. This accounts for the partial length of some of these features.

The exact nature of the domains is not known from this experiment. The domains are visible from scattering contrast, and the crystal is grown above its Curie temperature - these suggest that they are ferroelectric in nature, rather than orientational. Thus they are unlikely to be bulk mis-orientated features, such as macroscopic mosaic blocks, or even localised twins. Experiments such as surface decoration or pole-sensitive etching are required to determine this precisely.

The block-like features seen in the wing-section samples remain visible in most reflections as dark contrast or reversed contrast (in orthogonal reflections). This

suggests their origin as being not domain-like, and their position near the extremity of the growing facets of the crystal could simply suggest regions of highly non-ideal growth, possibly incorporating a different proportion of dopant ions. The numerous faint a-parallel bands are attributed to striation-contrast, associated with the surface striations seen on the a-faces of this sample.

These domains, in combination with the high dislocation-density and the presence of strain associated with point defects and inclusions all point to highly-imperfect structure.

5.3.6 Topographic studies of Ta:KTP

The a-sample of Ta:KTP showed only a few contrast features. Even after re-preparation, the sample still showed evidence of multiple-direction thin dark-contrast lines in topographs of various reflections, the remains of surface damage not removed by etching.

The 040 topograph of Figure 5.12 shows the only other contrast features seen: a faint, diffuse, dark-contrast region marked A, and a series of dislocations marked B, broadened slightly.

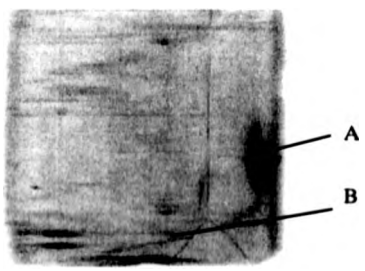

Figure 5.12 Topograph of the 040 reflection from the a-sample of Ta:KTP.

The sample dimensions were 4mm x 4mm x 0.3 mm.

The B-features, being random and present in multiple reflections are easily

identified as dislocations. The darker A feature appeared in all reflections, with slightly modified contrast (and the same dark contrast when the crystal was reversed). It is likely to be a small inclusion or congregation of point-defects, since it presents different geometries and is relatively large and diffuse.

The b-sample of Ta:KTP presented more contrast features in its topographs. The topograph of Figure 5.13 is for the 004 reflection, and quite clearly shows the presence of a growth-sector boundary in the left portion of the crystal. This is the boundary associated with the {201} facets of the crystal, and is visible due to strain contrast in its vicinity.

Figure 5.13 Enlargement from the 004 topograph for the b-sample of Ta:KTP

The rest of the image is filled with dislocation tracks, proceeding away from the GSB approximately parallel to the c-direction. The dislocations present extinct segments, and are broad. The strain-field associated with the larger dislocations is seen in Figure 5.14, the 400 reflection for this sample.

Figure 5.14 Topograph for the 400 reflection from the b-sample of Ta:KTP

The dislocations are partially absent in this reflection, and can be assumed to be of mixed character, since they appear segmented in the 004 reflection. The 808 reflection, in Figure 5.15 does not show the dislocations clearly, because the contrast is swamped by large block-like dark features. The largest, central block has one edge bounded at the GSB and at the dislocations at the top and bottom edges. The blocks are typically similar to those seen for the b-sample of TaGa:KTP described above.

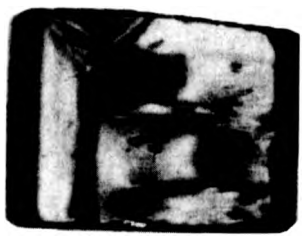

Figure 5.15 The 808 reflection from the b-sample of Ta:KTP

The dark blocks presented inverted contrast when the sample was reversed, and are seen in this reflection probably due to its anomalous-scattering nature. The segment of crystal seen in the top of the distinctive Y-shaped GSB has darker contrast than the rest of the sample. This differential scattering may be characteristic of different growth-regimes followed in the different portions of the sample.

5.3.7 Discussion and conclusion for Ta:KTP

Most topographs showed little evidence of defect features, apart from surface scratches and occasional dislocation tracks. This result suggests a relatively high degree of perfection in the samples of Ta:KTP, with a dislocation density in the region of one-two per cm^2. The topograph of Figure 5.15 contains the most contrast from the various defects, showing domains by anomalous scattering. The domains are apparently bounded by the GSB and dislocations, which modify the growth conditions seen as the domain propagates. The dislocations and inclusion seen in other reflections are likely to be formed in imperfect growth

conditions associated with the seed region or GSB, then running into the body of the crystal.

Certain topographs show the central growth-sector boundary. This feature, associated with the faint domain-like [010] bands are related to the high-resolution experiments seen in chapter 3. Here this sample, before being prepared for topographic study, demonstrated RLP peak-splitting related to misorientated diffracting regions. The angular misalignment of the diffracting regions is possibly related firstly to the growth-sector boundary, where different growth behaviours are related to the different sectors. Secondly, the domain-like regions imaged in these topographs possibly possess misalignment in the form of extended mosaic blocks. Absolute identification of domains is not possible, due to the faintness of the images, and the fact that they were only occasionally seen, and only in this [001]-faced sample. Their location in the centre of the bulk-crystal relates to imperfect growth conditions typically found here, and device-harvesting attempts to avoid this region, so device crystals ideally will not contain domains or defects.

5.4 Summary

The synchrotron topography experiments show a variety of defect features in the samples. Dislocations are present in both Ta:KTP and TaGa:KTP, though to a far greater extent in the latter. The TaGa:KTP presents particularly dense defect structure. Domains are apparently seen in both types, revealed by anomalous scattering effects, and are noted as being of a size of order fractions of a mm, and starting or finishing at growth-sector boundaries or dislocation-bundles. This is consistent with previous studies[1,2], which show growth-sectors and dislocations in pure, and Nb:KTP. The density of these defects is low enough so to be insignificant in terms of the optical properties of the materials. The presence of domains, however, is more important in that differential scattering from such features would affect SHG efficiency to varying extents. The distribution of

domains also appears random, meaning that if device crystals were cut from these bulk crystals, inconsistent quality would be found between samples. Examination of the domain regions in the TaGa:KTP sample under an optical microscope with crossed polarisers suggested that the domain walls were particularly broad, and hence possibly associated with orientational contrast as well.

The continuation of experiments to optimise the growth of these materials, and produce larger, defect/domain-free crystals is required before the full NLO potential of these particular KTP variants is realised. Synchrotron topography has been demonstrated as being a powerful way to determine these quality-aspects of KTP derivative materials.

5.5 References

[1] K.B. Hutton, R.C.C. Ward, K.W.Godfrey. *Mat. Res. Soc. Symp. Proc.* **329,** (1994) 23

[2] W.J. Liu, S.S. Jiang, X.R. Huang, X.B. Hu, W. Zeng, J.Q. Wei, J.Y. Wang, J.H. Jiang, Y. Han. *J. Cryst. Growth* **169,** (1996) 534

[3] "Characterisation of Crystal Growth Defects by X-Ray Methods" Ed. B.K.Tanner and D.K.Bowen, Plenum, London, (1980)

[4] K.Hutton, private communication.

Chapter 6

Conclusions

6.1 Summary

This thesis has been concerned with the structural quality of three specific KTP derivative materials. The defect structures have been examined using high-resolution x-ray diffraction, and synchrotron topography, and structural refinement has been performed for 4%Ta:KTP, along with simulation of its optical response.

6.1.1 High-resolution study

The high-resolution study in Chapter 3 revealed that all three sample types investigated had a significant defect structure, including mosaic blocks, and dislocations. Whilst the Ta:KTP sample was found to be close to ideal, except for the presence of a growth-sector boundary, the Nb:KTP and TaGa:KTP were found to possess large-scale mis-orientated blocks, which in the Nb:KTP case were found to correlate with the dense surface striations seen on the [100] face of the sample. These striations occur during growth, and generally are not important when they are present in low density. But in high densities, they are a symptom of the frustrated growth of the crystal. In the doped-KTP case, this is frustration in the [100] direction, to an extent that sometimes the dimension of the seed in this direction is the dimension of the final bulk crystal. As the {201} facets attempt to grow, then fail, a striation is begun with an [010] straight edge. The argument here is that these striations have a contribution to the bulk defect-structure, such that along [010] in the crystal, the structure appears as normal, but crossing [010] samples the various fine regions appear separated by tilt and *d*-spacing - this last caused by differential take-up of dopant between the regions.

Whilst this study is not representative of the behaviour of all such KTP derivatives, it does signal that the defect structure, and the growth striations, have implications for the optical properties. For SHG purposes, for example, the differential scattering induced by a fine structural variation in the crystal may lower the efficiency of frequency doubling.

The technique of high-resolution x-ray diffraction has been shown to be a relatively poweful tool for investigating the defects found in KTP derivatives.

6.1.2 Structural study for Ta:KTP

The structural refinement of Chapter 4 provides evidence that places Ta in the unit cell of KTP in much the same manner as Nb[1]. Preference for the Ti(1) site is shown, and the Ti site is forced into centricity compared to pure KTP. The small structural shifts that cause this are too low to account for any optical performance modifications, and suggest that the polarisability of the Ta itself is responsible. In addition, to resolve residual electron density in the difference maps, the refinement required that K vacancies be held at charge-balancing levels. This achieved a new residual peak of an intensity and location that could reflect the true position of Ta in the unit cell. These results are reinforced by the optical simulation carried out in Chapter 4.2, which produced a good simulation fit for refractive indices and birefringences when the polarisability volume of the OT(1) and OT(2) sites, the linking members of the Ti-O chains, was greatly increased relative to other O sites. The volume of the two O atoms nearest the suggested new site for Ta are also greater in the best-fit model, which could suggest the importance of this site in contribution to the NLO character of the material.

However, the existence of this site has not been proven in this thesis. What remains is to prove that the residual electron density is not due to a modelling error similar to that now thought to be responsible when residual density appears in KTP hole sites.

The study does serve to extend the understanding of Ti-site doping by providing another structure as an example. Structure/property analysis for the Ti-

substituted KTP variants should benefit from another comparison to the Nb:KTP case.

6.1.3 Synchrotron topography

Synchrotron topography was used to identify the defects found in the samples of Ta:KTP and TaGa:KTP. Simple dislocations were found in varying concentrations for both derivatives, and generally were sourced at the seed/crystal interface. The presence of domains in TaGa:KTP was suggested by the contrast revealed in anomalous-scattering reflections. These domains began at a defect, and then propagated with the growing facets until normal growth was established, perhaps by the action of another defect. The scale of the domains found varied from many mm to sub-mm size, and they were distributed at random. Their contribution to lowered SHG efficiency could be pronounced, if they were present in great enough numbers along the propagation path in a device crystal. Similar features were seen in Ta:KTP, to a smaller extent and not so readily identified.

By comparison of the Ta:KTP and TaGa:KTP topographs, it can be seen that the surface-striated TaGa:KTP presents the greater defect density in the bulk crystal. Whether this is a symptom of the frustrated growth, or a cause of it, remains to be determined.

Synchrotron topography has been shown to be an excellent method for determining the extent of defects in bulk crystals of KTP derivatives, complimenting the investigation by high-resolution diffraction.

6.2 General conclusion

By following 4%Ta-doped KTP through high-resolution x-ray analysis, to structural refinement and simulation of optical response, to an investigation of the defect structure by synchrotron topography, it has been shown that this particular material grows into a crystal with increased birefringence and low defect density. Comparison with different doping levels of Ta:KTP could further the understanding of the role of Ta in the material's optical response, and the

structural modifications induced by the dopant. The work performed here demonstrates difficulties for the well-studied Nb:KTP in terms of crystal quality. Whilst not exhaustive, it also provides an analysis of the defects seen in a new KTP variant, TaGa:KTP, which is an experiment in co-doping of KTP to produce a new class of material. This class may in the future provide the most promising of KTP variants, because of the numerous possible routes for producing a material with desired properties.

6.3 References

[1] P. A. Thomas, B. E. Watts. *Solid State Commun.* **73,** (1990) 97

Chapter 7

Suggestions for Future Work

7.1 Doping of KTP

To access the useful characteristics of the potential M:KTP materials, increased structural analysis of the existing materials is needed to establish the contribution of the dopant atoms to structural change. In particular, the significance of the potential new site for Ti-substitute ions suggested in the structural refinement of Chapter 4 should be investigated, since this may improve understanding of the mechanisms of dopant incorporation, and hence allow better design of future materials.

With good structure-property understanding, the growth-programme of new KTP-like materials could produce end-use-specific crystals, with 'engineered' properties.

7.2 Flux-growth of doped KTP

The investigation of Bordui and Motakef gives an insight into the precise conditions of the flux/crystal interface during flux-growth of KTP. Hydrodynamic simulation demonstrated the flow of flux-nutrient over the surfaces of a rotating crystal as it grows in a TSSG experiment: any situation whereby 'stale' nutrient is presented for incorporation into the crystal potentially results in the formation of defect features from point-defects to flux inclusions. These are postulated as occurring where the morphology of the spinning bulk-crystal causes small, transient drag-vortices close to the growing facets. The paper describes how by adjusting the angle of the crystal suspended in the melt, improved flow patterns led to growth of higher quality crystals of pure KTP.

Doped M:KTP crystals often present modified morphologies to pure KTP, which

can be either as broader, more spherical shapes or largely plate-like shapes (with narrowest dimensions in the a-direction, which is naturally reluctant to grow). In this case, the flow of nutrient over the growing crystal-facets is likely to be slightly or even radically different from undoped KTP conditions, dependent on the particular morphologies. Where flat, paddle-like morphologies are observed (for example, TaGa:KTP which shows a flat, distorted-rhomboid cross-section) the formation of vortices near the trailing-edges of spinning crystals is possibly increased. Whilst the TSSG method involves periods of direction-reversed spin, designed to destroy transient vortices, the timescale for these is decided by intuitive analysis of previous growth-runs, and thus may not be optimum for modified crystal morphologies. In this case, the formation of undesirable drag-effects may influence the presence of 'stale' flux near the growing facets, possibly to the detriment of the crystal quality. The creation of increased surface striation and crystal defects such as those seen in this thesis is possibly linked to this non-ideal growth behaviour.

The growth of M:KTP materials by the TSSG method could benefit from investigation of the contribution of altered morphology to defect formation, possibly by similar hydrodynamic analysis.

7.3 High-resolution x-ray diffraction analysis

The HRXRD analysis performed in this thesis, in parallel to synchrotron and high-resolution topography identified aspects of the lower crystal quality seen in the M:KTP crystals under investigation. The technique is powerful, particularly demonstrated by its use in analysing complex hetero-structured semiconductors. For KTP materials, the technique could be improved by applying 3D reciprocal-space analysis: this method, as outlined by Fewster[2], provides a more powerful way of quantifying the defect structure of the materials examined, in the laboratory environment.

7.4 References

[1] P.F. Bordui, S. Motakef. *J. Cryst. Growth* **96,** (1989) 405

[2] P.F. Fewster, N.L. Andrew. *J. Phys. D: Appl. Phys.* **28,** (1995) A97